Spring 5-2018

# Antineutrino-Induced Charge Current Quasi-Elastic Neutral Hyperon Cross-Section on Argon In Argoneut

Samuel M. Borer

# ANTINEUTRINO-INDUCED CHARGE CURRENT QUASI-ELASTIC NEUTRAL HYPERON CROSS-SECTION ON ARGON IN ARGONEUT

by

Samuel M. Borer

A Thesis Submitted in Partial Fulfillment
of the Requirements for a Degree with Honors
(Physics)

The Honors College

University of Maine

May 2018

Advisory Committee:

Dr. Saima Farooq, Lecturer in Physics, Advisor
Dr. Samuel T. Hess, Professor of Physics
Dr. Michael C. Wittmann, Professor of Physics
Dr. François G. Amar, Professor of Chemistry and Dean,Honors College
Dr. Melissa Ladenheim, Associate Dean, Honors College

ABSTRACT

This thesis outlines the first measurement of CCQE neutral hyperon production cross section in a liquid argon time projection chamber (LArTPC) through a topological study [1] and presents the ongoing progress of the addition of a calorimetric study. The analysis uses $1.20 \times 10^{20}$ protons-on-target, in the NuMI beam operating in the low energy antineutrino mode. The results of the topological study provide a total cross section measurement at the mean production energy of 3.42 GeV for CCQE neutral hyperons. The result of the topological study is consistent with the NUANCE cross section model and sets a 90% confidence level on the upper limit of the cross section. The calorimetric study is ongoing and shows promise to provide additional results to compare with results of the topological study [1]. The progress and further steps are presented in this thesis.

*Dedicated to my Mother: Self-proclaimed Queen of Everything.*

*Long Live The Queen*

ACKNOWLEDGEMENTS

This work was not conducted in a vacuum and I have been very fortunate to have so many amazing family, friends, and mentors there to help me along this path.

First, to my research advisor Dr. Saima Farooq. I cannot adequately express in words my appreciation for your time, dedication, and effort in guiding me and, at some times, dragging me through this process. You were under no obligation to assist any students with research and your schedule was already filled to the brim. For you to take me under your wing and work with me through this thesis, outside of your regular duties, says volumes about your character, resolve, and capacity for kindness. Without you, nothing on these pages would be possible.

To my family, who lived scattered across the globe through the entire process of this thesis. My mother, who was always willing to field a frantic phone call from across the world. Your counsel, love, and support has fueled me through my darkest hours. My father, who I could always count on for steadfast encouragement and the kind of love that exists as a soft, warm glow. To my twin sister, you have been my partner-in-crime my entire life and your influence is seen in every step I take. My brother, who's own personal development has provided inspiration to me throughout this journey.

To my friends, who I called on more like my immediate family in their absence. Jackie MacCallum, Chaya Karunasiri, and Anna Landry, who entered halfway through this chapter of my life, but I know will remain in it until it's final chapter. Your friendship has given me energy when I felt powerless, momentum when I couldn't take another step, and scintillation when everything around me seemed too dark to see a path forward. Paul Caruso, thank you for being the best friend I never saw coming. This thesis would never have happened without your influence in my life.

To my mentors, who have shepherded me through a very turbulent and ever-shifting phase in my life. Dr. Robert Dana, Dr. Melissa Ladenheim, Admiral Gregory 'Grog' Johnson, Major Carrie Mancini, Rosa Redonnett, Dr. Farahad Dastoor, Dr. Kristy Townsend, Colonel Eric Johns, Kimberley Minor, Dr. Sophie Todd, and far too many more people to list. I have never solved a problem alone and I am so grateful for your open doors and your willingness to walk through my challenges with me.

CONTENTS

# CHAPTER 1

# THE NEUTRINO

Neutrinos have a storied and elegant history that has interwoven itself throughout theory and experiment, spanning over 80 years and four Nobel prizes to date. This chapter will explore the proposed existence, discovery, and description of the neutrino. The contents of this Chapter have been adapted from [10].

## 1.1 Follow The Missing Energy

### 1.1.1 Neutrino Proposition

Physics is built on a foundation of conservation. Nature conserves energy, it conserves mass, it conserves linear momentum, and conserve color charge. The birth of neutrino arose from this conservation. Neutrinos were first postulated as a consequence of nuclear beta decay. In beta decay, a heavy radioactive nucleus is converted into a lighter one, losing an electron in the transformation.

$$N(A,Z) \rightarrow N'(A,Z+1) + e^{-} \tag{1.1}$$

Here $N$ and $N'$ are parent and daughter nuclei, respectively and $e^{-}$ is the emitted electron.

This process was thought to have been a two-body decay, because the daughter nuclei and electron were the only particles observed. When the parent nucleus is at rest, the electron's energy is a fixed value as a consequence of the conservation of energy

and momentum,

$$E_e = \frac{m_N^2 - m_{N'}^2 + m_{e^-}^2}{2m_{N'}} \tag{1.2}$$

The problem arose that equation 1.2 should give a unique value, but what was observed was a continuous spectrum of energy values. This continuous spectrum laid a direct threat to the foundation of conservation of energy. In 1930, in a letter to a conference at ETH Zurich, Wolfgang Pauli proposed the existence of a light neutral spin-1/2 particle that was being emitted with the electron in beta decay [19]. If true, this new particle would balance out the kinetic energy of the electron and explain the observed continuous spectrum without breaking conservation of energy. Originally he named this particle the "neutron", but the name was taken when James Chadwick discovered the proton-like neutral hadron we know as the neutron today.

While postulated by Pauli in 1930, the theory was not fully accepted until 1934 when Enrico Fermi described the beta decay model in full, shown below, setting many doubts to rest [20].

$$n \rightarrow p + e^- + \bar{\nu}_e \tag{1.3}$$

### 1.1.2 Experimental Detection

The actual experimental detection would wait over 20 years until 1956 when Cowan, Reines, and their colleagues observed antineutrinos [21]. The Savannah River nuclear reactor in South Carolina was used because it emits a flux of antineutrinos from beta decay. These antineutrinos can interact with protons in the tank of water and $CdCl_2$ to produce a neutron and positron.

$$\bar{\nu}_e + p \rightarrow n + e^+ \tag{1.4}$$

This observation was made possible because unlike neutrinos, neutrons and positrons can be detected with relative ease. The positron shown in the process above will annihilate with an electron and produce two photons that are detected by scintillator and photomultiplier tubes in the tank. The neutron produced will be captured by the Cd nucleus and undergo a specific process, $n + {}^{108}\mathrm{Cd} \rightarrow {}^{109}\mathrm{Cd}^{*} \rightarrow {}^{109}\mathrm{Cd} + \gamma$. The emitted photon will be detected approximately 5 $\mu$s after the initial $e^{+}e^{-}$ annihilation. This unique pattern of photon detection, which was not detected when the detector was off, allowed for the experimental confirmation of the neutrino.

### 1.1.3 Small Particle, Large Implications

Following their initial detection, neutrinos have played an integral role in our understanding and development of the Standard Model of Particle Physics. The original theory proposed by Pauli called for a single neutrino, however, following the detection of the electron neutrino ($\nu_e$), two other neutrino flavors have been identified, the muon neutrino ($\nu_\mu$) at Brookhaven in 1962 [22], and the tau ($\nu_\tau$) neutrino at Fermilab in 2000 [23]. The flavor types correspond to the charge lepton produced in interactions. Originally, the Standard Model predicted neutrinos to have a zero mass value, but the discovery of neutrino oscillations showed neutrinos to have a non-zero mass. The measurement of this non-zero mass is a current priority in many neutrino physics experiments.

Neutrino oscillations provided wide spread implications and promoted the start of many characteristic studies, including parity violation studies and investigating the possibility of sterile neutrino states. This will be discussed in more detail in a later section.

## 1.2 Neutrino Properties

The neutrino we understand today has a slew of key properties that make it a unique particle. We know that the neutrino is a spin 1/2 particle and has three flavors, $\nu_e$, $\nu_\mu$, and $\nu_\tau$, with anti-particles $\bar{\nu}_e$, $\bar{\nu}_\mu$, and $\bar{\nu}_\tau$. Neutrinos interact via weak interactions propagated by the $W^{\pm}$ and $Z^0$ bosons. This primary weak interactions is what gives neutrinos their famously small interaction cross sections.

Unique with their elusiveness is their abundance. Neutrinos are one of the most abundant particles in the universe. We exist in a constant shower of neutrinos from various sources. There is a constant background cosmological neutrino density, averaged around $n_\nu \simeq 336\text{cm}^{-3}$, created from the young, hot universe. This value can be higher within our galaxy due to the effects of gravitational clustering. Every time a large star succumbs to its own gravitational forces and produces supernova explosion, an incredible number of neutrinos ($\sim 10^{58}$) are emitted. In addition, the flux states that approximately 60 billion solar neutrinos, created by the nuclear reactions occurring in the sun's core, travel through each square centimeter of our bodies every second.

### 1.2.1 Parity Violation and Helicity

Mirror reflection symmetry, known as parity, was thought to be a constant characteristic of all particles. This idea was invalidated experimentally in 1957 [24] when it was determined experimentally that the $\beta$ decay of $^{60}Co$ violated parity in its' weak interactions.

$$^{60}Co \rightarrow ^{60}Ni + e^- + \bar{\nu}_e \tag{1.5}$$

When cobalt salt was polarized by a strong magnetic field, a measurement of the angular distribution of the emitted electrons showed a strong preference for the inverse direction of the magnetic field [4]. Since the spin direction of the cobalt nuclei aligns with the magnetic field, the expectation value of $\cos\theta_e$ was negative [25]. This dichotomy between the emitted electron direction and nuclear spin provided significant evidence for parity violation in weak interactions.

Helicity is the inner product of a particle's momentum and its' spin vector at any time reference. A neutrino is considered 'left-handed' because its momentum and spin vector are anti-parallel, whereas an antineutrino is 'right-handed' because its momentum and spin vector as parallel. However, after neutrino oscillations showed that neutrinos have a non-zero mass, depending on the reference frame, both neutrinos and antineutrinos were determined to be either left-handed or right-handed.

### 1.2.2 Neutrino Oscillations

Of the sources of neutrinos, there is sufficient evidence that solar, atmospheric, accelerator, and reactor neutrinos oscillate from one flavor to another. This flavor oscillation has serious implications, informing us that neutrinos have mass and that leptons can mix. It is interesting to note, historically, that the Standard Model predicted neutrinos to be massless. The discovery of neutrino oscillations, outlined briefly in the following section, proved this to be definitively false.

#### Solar Neutrino Problem

The sun is powered almost primarily by the proton-proton fusion chain reaction that turns hydrogen into helium. The chain of reactions in this p-p process produces a significant amount of electron neutrinos as a byproduct. The detailed spectrum of reactions, including nine distinct neutrino-producing reactions, is captured in the 'Standard Solar Model' and is used to predict the theoretical neutrino flux that should

be measured on Earth. In the 1960s, experimental physicists turned their gaze to the sun in an attempt to measure the flux of these electron neutrinos, comparing the results to the theoretical predictions [3].

Roughly $6.5 \times 10^{10}$ solar neutrinos travel through every square centimeter of the Earth per second. Within the complex proton-proton chain reaction most of the neutrinos are created in the first step, but they have an energy of $> 0.43$ MeV and thus are extremely difficult to detect. Low energies decrease the interaction cross section and create a weak interaction signature, both vital for consistent detection. Most of the neutrinos that reach the Earth are created from $^8$B neutrinos, which can exist in energies up to 15 MeV.

As the results of measuring the solar neutrino flux came in, a problem emerged. The experimental results showed a severe deviation from what theory predicted. The first detection came from Ray Davis's Homestake experiment in the 1960s. Using a 100,000 gallon tank of dry-cleaning fluid ($C_2Cl_4$), a flux was experimentally measured to be one-third lower than the theoretical value. This phenomena was known as the "Solar Neutrino Problem" and was independently verified by subsequent neutrino detectors, each with slightly different deficits. The difference in these deficits can be attributed to the characteristic of each experiment having different detection thresholds and the solar neutrino flux changing as a function of energy, seen in Figure 1.1.

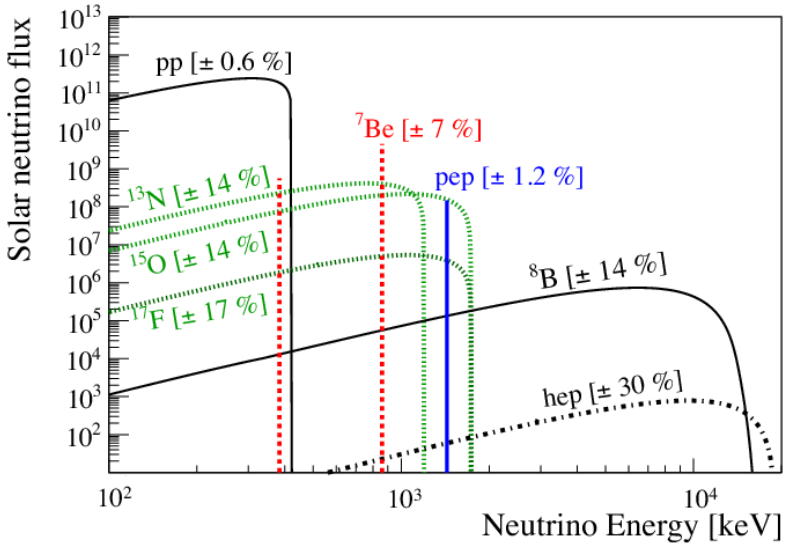


FIGURE 1.1: Solar neutrino flux as a function of energy. Figure from Ref [2].

For the next 40 years, numerous experiments tried to crack the solar neutrino problem, to no avail. Finally, in 2001, a Cerenkov-based detector known as the Sudbury Neutrino Observatory (SNO) solved the problem [26]. Using a spherical detector filled with 1,000 tons of heavy water that was surrounded by photomultiplier tube, SNO detected two key reactions independently:

$$\nu_e + d \rightarrow p + p + e^- \tag{1.6}$$
$$\nu_{e,\mu,\tau} + d \rightarrow p + n + \nu_{e,\mu,\tau}$$

where $p$ is a proton, $n$ is a neutron, and $d$ is a deuteron.

The first interaction is a charged-current interaction. Solar neutrinos, with energies $< 18$ MeV, are too low energy to produce a large muon or tau particle (rest masses of 106 MeV and 1780 MeV, respectively), so the reaction only proceeds through electron-neutrinos. Due to this characteristic, the first reaction only measures the electron-neutrino flux. But, the second interaction is flavor-blind and thus measures the total neutrino flux. By using the two different flux values, SNO discovered that the total

flux was three times greater than the electron-neutrino flux alone. This confirmed that the neutrinos did not disappear, but rather oscillated from one flavor to another. Figure 1.2 shows the experimental results of several neutrino detectors.

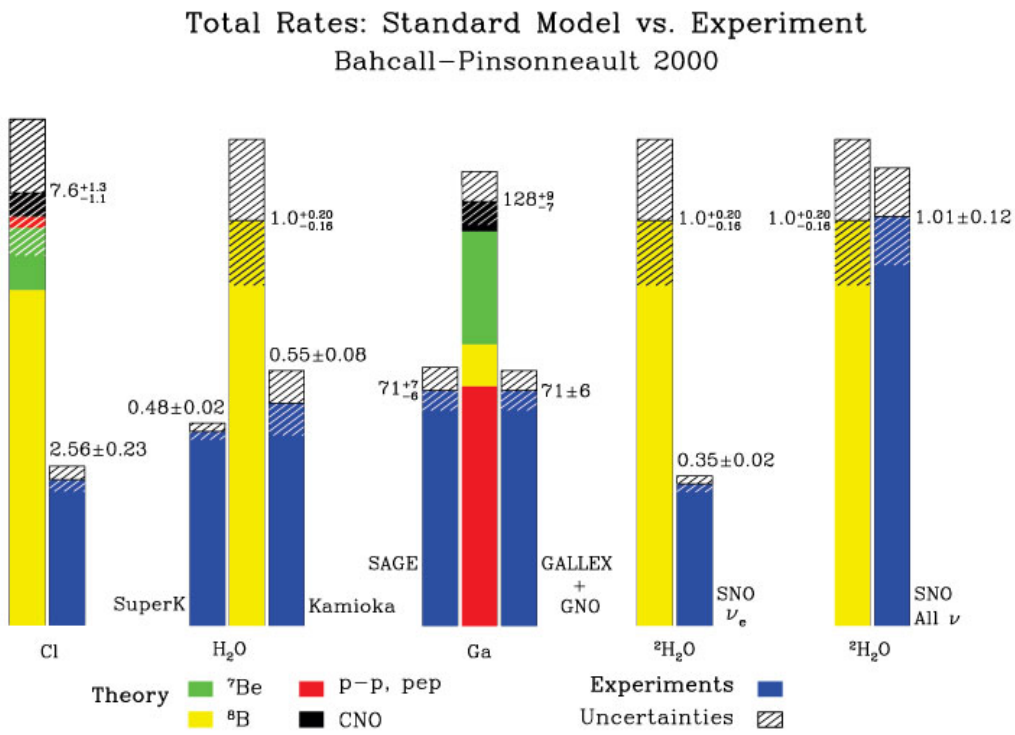


FIGURE 1.2: Solar Neutrino Flux observed (blue) by seven neutrino detectors. The first three groups show the large deficits found in the first-generation detectors. The total flux values are composites of the individual solar processes: green for electron capture by $^7$Be, yellow for $^8$B decay, red for pep fusion, and black for the stellar carbon-nitrogen-oxygen cycle. Figure from [3]

### 1.2.3 Neutrino Mass

The discovery of neutrino oscillations and the subsequent implication of neutrino mass marks one of the greatest discoveries in particle physics in the last decade. The Standard Model contains no right-handed neutrinos or left-handed antineutrinos. This results in the Standard Model neutrinos being massless, distinguishable only by

their lepton number. Being that experiment has shown that neutrinos oscillate, mass must be added to Standard Model neutrinos somehow.

## 1.3 Neutrino Scattering

Neutrino interactions were an incredibly useful tool while the Electroweak theory was being developed, a half a century ago. The beauty of neutrinos is that they are not shrouded by other forces. Since their chargeless and colorless demeanor interacts only with the Weak force, they offer a sterile meter from which to investigate weak interactions. The remainder of this Chapter is adapted from [1].

As future neutrino experiments probe higher neutrino energy ranges ($\sim$1 GeV), an interesting characteristic arises. At certain energy ranges, one or two interaction channels can dominate, but at higher energies the interaction channels show no favor to one or another. At a higher energy range, most of the interaction modes are possible, but the cross section for each is very large, roughly 20%. Additionally, because of neutrinos' low cross section most neutrino experiments utilize dense complex target material, commonly noble elements, which add significant nuclear effects that obscure the topology of neutrino interactions further. These nuclear effects are difficult to model and lead to increasing uncertainties in analyses.

This section will give a brief overview of neutrino interactions, delving only into neutrino-nucleus interactions from which this study relates. As this is an experimental thesis, the interactions will be discussed from the qualitative perspective experimentally.

When we consider neutrino interactions, we can consider them massless. In electroweak theory, we can also consider all neutrinos to be purely left-handed and their interactions mediated by weak charge currents (involving $W^{\pm}$ bosons) and weak neutral currents (involving $Z^0$ bosons).

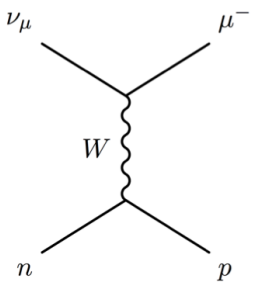


FIGURE 1.3: Charge current quasi-elastic scattering. Figure from [1].

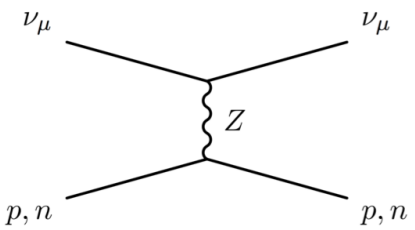


FIGURE 1.4: Neutral current elastic scattering. Figure from [1].

### 1.3.1 Neutrino-Nuclear Interactions

Neutrino-nucleus interactions are tough to model because they enter the realm of strong interactions as well, leading to a greater emphasis on the range of neutrino energies considered. Neutrino-nucleus interactions can be broken down into several subprocesses, each with a different probability dependent on the incident neutrino energy: coherent, elastic/quasi-elastic, resonant and deep inelastic.

An important characteristic in neutrino-nucleon scattering is momentum transfer, $Q^2$, from the neutrino to the nucleon and it defines the neutrino's resolving power. When $Q^2$ is low, the nucleon can be treated as a single entity comprised of quarks, but when $Q^2$ is high, you can get the resolution of single quarks. This variation makes higher $Q^2$ interactions more complex. The following sections will describe neutrino-nucleus interactions, in the order of increasing $Q^2$.

#### Elastic and Quasi-Elastic Scattering

In elastic neutral current interactions, the neutrino scatters elastically off a nucleon. In the quasi-elastic charge current interactions, energy is released that forms a lepton, which gives the quasi-elastic designation.

In neutrino interactions, it is important to identify what part of the interaction is observable through experiment. For neutral current interactions, the observable signal

is the knocked out nucleon. In the charge current interactions, the observable signal is the lepton produced.

With Charge Current Quasi-Elastic (CCQE) interactions, the neutrino energy is calculated by measuring the outgoing lepton's momentum and the angle in relation to the incident neutrino direction. The lepton carries most of the incident neutrino's energy, making it an easily reconstructable track. The problem with CCQE interactions is that other experimental backgrounds can give similar signals, which can interfere with the calculation of the neutrino energy or the event rate. This makes tagging CCQE events of significant importance and difficulty.

### Resonant Scattering

Continuing to increase the neutrino energy range higher into the GeV range and resonant scattering begins to dominate. As $Q^2$ rises with the energy, there is enough momentum transferred to the target nucleon that it can enter an excited state, known as a resonance, and decays to a nucleon and a pion. The most common resonance is the $\Delta$ particle, which will decay into a nucleon (proton or neutron) and a pion, via the strong force. For charge current interactions, the observable signal is a charge lepton accompanied with the nucleon and pion, while for neutral current interactions the charge lepton is swapped with a neutrino of the same flavor as the incident neutrino. These processes can be seen in Figure 1.5.

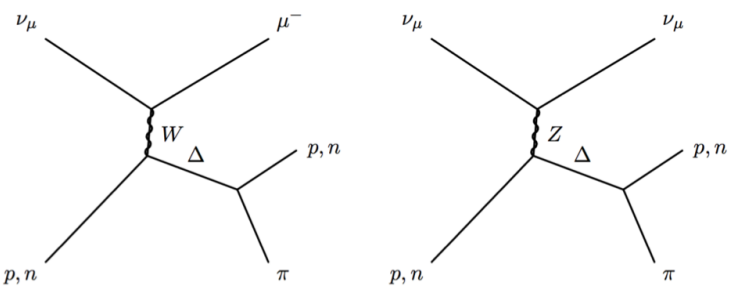


FIGURE 1.5: (Left) Charge current resonant scattering (Right) Neutral current resonant scattering. Figure from [1].

### Coherent Scattering

In coherent scattering, a neutrino interacts with the nucleus as a whole, giving a small $Q^2$. With a small momentum transfer, the nucleus remains in the ground state and a pion is produced with a charge lepton, if charge current, or a neutrino, if neutral current. This is shown in Figure 1.6.

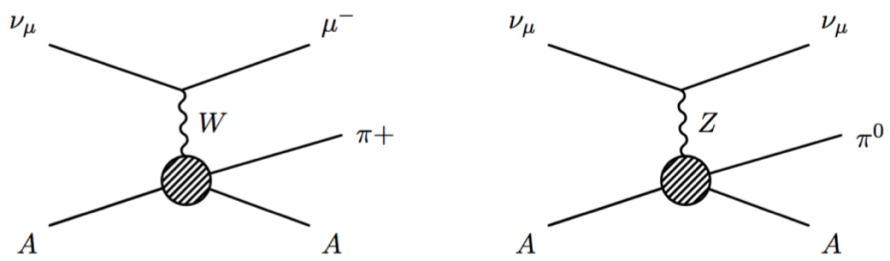


FIGURE 1.6: (Left) Charge current coherent scattering (Right) Neutral current coherent scattering. Figure from [1].

### Deep Inelastic Scattering

With deep inelastic scattering, the $Q^2$ becomes high enough that the neutrino can break down the nucleus. This allows interactions with the quasi-free quarks that exist in the nucleon. When the neutrino interacts with a quasi-free quark, the quark will recoil and produce a hadron shower, including nucleons, pions, strange particles and others. This process is shown in Figure 1.7.

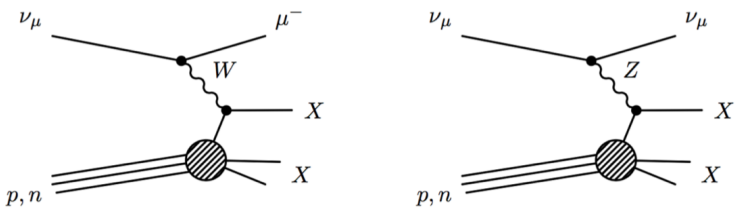


FIGURE 1.7: (Left) Charge current deep inelastic scattering (Right) Neutral current deep inelastic scattering. Figure from [1].

### 1.3.2 Charge Current Quasi-Elastic Scattering in NUANCE

This section presents the charge current quasi-elastic (CCQE) scattering theory and includes a description of how Cabibbo-suppressed CCQE scattering is modeled in the NUANCE neutrino event generator [5].

#### CCQE Scattering

Charge current quasi-elastic neutrino scattering off of a nucleon can be shown through two processes:

$$\begin{aligned} \nu_l + n &\rightarrow l^- + p, \\ \bar{\nu}_l + p &\rightarrow l^+ + n \end{aligned} \tag{1.7}$$

These processes were well studied in the 1970's utilizing bubble chambers [27].

Due to the characteristics of neutrinos, most neutrino experiments, including LArTPC experiments, a bound nucleon is the target. This can be written as,

$$\begin{aligned} \nu_l + A &\rightarrow l^- + A', \\ \bar{\nu}_l + A &\rightarrow l^+ + A' \end{aligned} \tag{1.8}$$

Here $A$ is the initial state nucleus and $A'$ is the final state nucleus with a hadron. The cross section model used in this analysis is the work of Smith and Moniz [28]. In the model, the cross section for free and bound nucleons are calculated and the Fermi gas model is used to calculate Pauli blocking and Fermi motion for a bound nucleon target [5].

Cabibbo-Suppressed CCQE Scattering

Cabibbo-suppressed CCQE scattering is considered the simplest process following CCQE scattering (shown in Equation 1.7). The processes are shown as,

$$\begin{aligned} \bar{\nu}_l + p &\rightarrow l^+ + \Lambda^0, \\ \bar{\nu}_l + p &\rightarrow l^+ + \Sigma^0, \\ \bar{\nu}_l + n &\rightarrow l^+ + \Sigma^-. \end{aligned} \tag{1.9}$$

These processes are well calculated, historically by [6, 27, 29, 30] and more recently by [7, 31–33]. The cross section models of these processes are vary widely from each other.

Equation 1.9 shows processes that only occur with antineutrinos (restricted by the $\Delta S = \Delta Q$ selection rule) and converts a u-quark to an s-quark, which transforms a proton into a $\Lambda^0$ or $\Sigma^0$, or a neutron into a $\Sigma^-$. These processes are suppressed by a factor of $\sin^2\theta_c \approx 0.05$, where $\theta_c$ is the Cabbibo angle, which makes them extremely rare. Since this process is only induced by antineutrinos, it can be used as an 'antineutrino tagger' with neutrino experiments. Another motivation for studying these processes is that, at low energy, hyperons do not experience Pauli blocking, unlike neutron production. When a proton is converted to a neutron, known as CCQE neutron production, the neutron cannot stay in the same shell in the nucleus because the Pauli-Exclusion principle does not allow two identical nuclear particles to exist in a single energy state. The energy must also be above an interaction threshold to take place, meaning at low-energies the process is Pauli-blocked. Hyperons, however, do not see this effect.

This study details the detection of neutral hyperons, given in the first two reactions of Equation 1.9. This process converts a proton to a neutral hyperon, via $u-s$ quark coupling mediated by the $W^-$ boson. $\Lambda^0$ and $\Sigma^0$ have minimum threshold neutrino energies of $\sim$ 325 MeV and 425 MeV respectively. In the final state of the interaction,

a $\mu^+$ and a neutral hyperon ($\Lambda^0$ or $\Sigma^0$) is created. Due to neutral particles inability to be detected, they will only be seen in the detector if they decay into charged particles. $\Lambda^0$ and $\Sigma^0$ have decay times of $(2.632 \pm 0.020) \times 10^{-10}$ s and $(7.4 \pm 0.7) \times 10^{-20}$ s, with masses of (1115.683±0.0006) MeV and (1192.642±0.024) MeV, respectively. The decay lengths, for $v < c$ and corresponding to the decay times, for each are 7.8 cm and 0.022 nm, respectively. It is important to note that the decay length of the $\Sigma^0$ is larger than the radius of an argon nucleus ($\sim 10^{-15}$ m). This means that it will leave the nucleus before decaying into a $\Lambda^0$. Its short decay is attributed to its electromagnetic decay, as compared to the weak decay of $\Lambda^0$. 64% of the time, $\Lambda^0$ will decay to $p\pi^-$ and 36% of the time to $n\pi^0$. $\Sigma^0$ will decay into $\Lambda^0$ 100% of the time, which will then decay through the two processes detailed above.

The Smith and Moniz model has been extended for Cabibbo-suppressed CCQE processes to integrate the inelasticity and the $|\Delta I| = \frac{1}{2}$ rule, using the calculations made by Pais [6]. The cross section for the Cabibbo-suppressed CCQE processes, determined by Pais, as a function of antineutrino energy is shown in Figure 1.8.

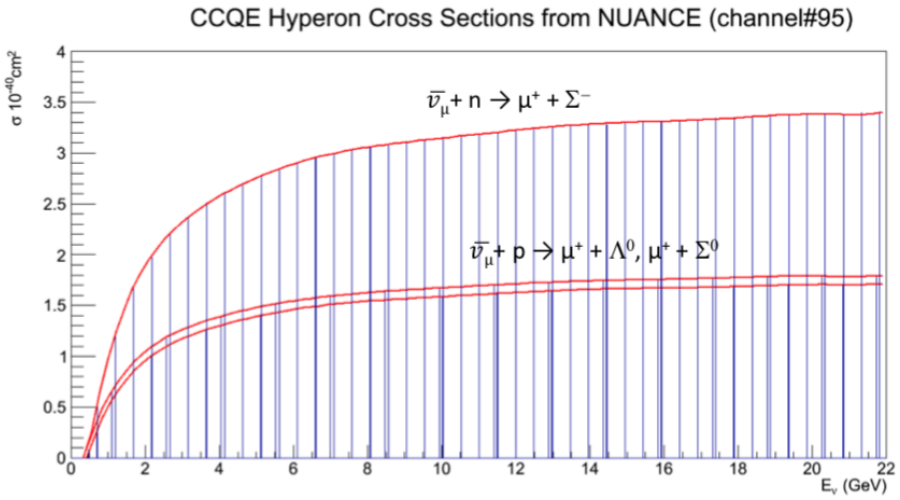


FIGURE 1.8: CCQE Neutral Hyperon Cross Section as calculated by Pais, used in the NUANCE Event Generator. [4][5][6]

The study of Cabibbo-suppressed CCQE processes has been pursued in bubble chamber experiments with propane with admixtures of freon, freon without propane, and hydrogen as neutrino targets. There are large statistical uncertainties, due to the small number of data events acquired. With advancements in more intense neutrino beams and larger neutrino detectors, the ability to study these processes becomes more realistic.

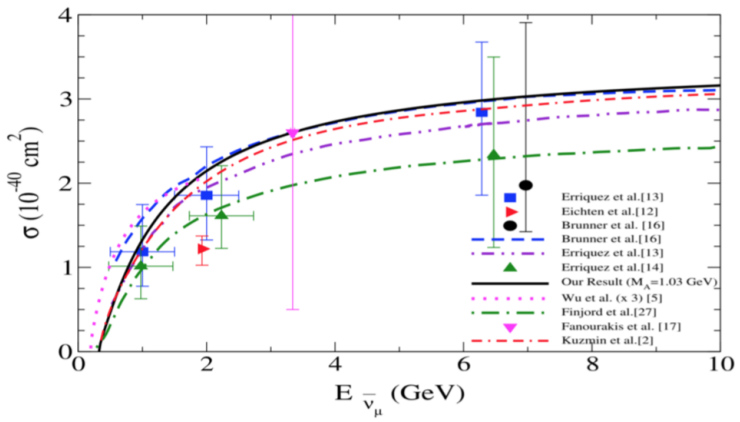


FIGURE 1.9: $\sigma$ vs. $E_{\bar{\nu}}$ for the $\bar{\nu}_l + p \longrightarrow l^+ + \Lambda^0$ process. Figure from [7].

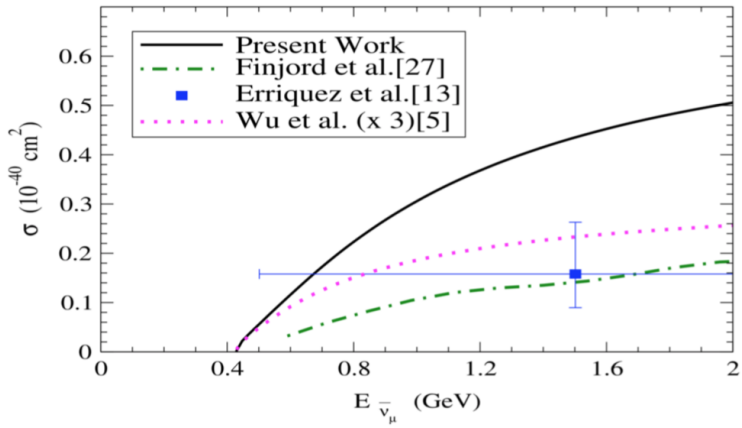


FIGURE 1.10: $\sigma$ vs. $E_{\bar{\nu}}$ for the $\bar{\nu}_l + p \longrightarrow l^+ + \Lambda^0$ process. Figure from [7].

Figure 1.9 and Figure 1.10 shows the theoretical calculation, from [7], for the $\bar{\nu}_l + p \longrightarrow l^+ + \Lambda^0/\Sigma^0$ process and the experimental measurements.

### 1.3.3 Nuclear Effects

For the NUANCE neutrino event generator [5] used in this analysis, a starting position is given to a neutrino interacting with a nucleon by utilizing the measured nuclear density distribution [34]. NUANCE considers each nucleus as an isoscalar sphere with Fermi momentum and radially-dependent density. As hadrons propogate, they are traced in 0.2 fm steps within the nucleus. At each step, the interaction probability is calculated using the local density and the single-nucleus cross section (nucleon-nucleon and pion-nucleon). All interactions are Pauli blocked if they exit the nucleon with a momentum below Fermi sea. Neutral kaons are 50% $K_s$ and 50% $K_L$, with the cross section of $K_L$ being calculated by an equal mixture of $K^0$ and $\bar{K}^0$ and the cross section of $K_s$ is 50% in every interaction.

The simulation makes certain approximations of hyperons, of note that they are non-interacting and non-decaying in the nucleus. In the data, when hyperons are produced in the nucleus, they can proceed through the elastic, quasi-elastic, and charge-exchange processes with nucleons [31],

$$\begin{aligned} \Lambda^0 + p &\rightarrow \Lambda^0 + p, \\ \Lambda^0 + n &\rightarrow \Lambda^0 + n, \\ \Sigma^0 + p &\rightarrow \Sigma^0 + p, \\ \Sigma^0 + n &\rightarrow \Sigma^0 + n. \end{aligned} \tag{1.10}$$

Equation 1.10 displays a hyperon elastically scattering with a nucleon. When looking at Equation 1.11, the first two processes, both quasi-elastic, will typically increase the cross section of $\Lambda^0$ while lowering the cross section for $\Sigma^0$ and $\Sigma^-$. This effect grows stronger as the charge and mass number of the nucleus increases. The last

two processes of Equation 1.11 are both charge-exchange and produce a $\Sigma^+$.

$$\begin{aligned} \Sigma^- + p &\rightarrow \Lambda^0 + n, \\ \Sigma^0 + n &\rightarrow \Lambda^0 + n, \\ \Lambda^0 + p &\rightarrow \Sigma^+ + n, \\ \Sigma^0 + p &\rightarrow \Sigma^+ + n. \end{aligned} \tag{1.11}$$

An additional process that increases the production of $\Lambda^0$ in data is the decay of $\Sigma^0$ in the nucleus;

$$\Sigma^0 \rightarrow \Lambda^0 + \gamma \tag{1.12}$$

However, the mean life is so long that the decay almost exclusively happens outside the nucleus and is thus ignored in the simulations. The result presented in this study is the production cross section of CCQE neutral hyperons on an argon target and is consistent with the NUANCE model.

# CHAPTER 2

## Accelerators and Neutrinos: A Love Story

There have been many experiments that utilize neutrinos produced without man-made interventions. This has provided significant leaps in our understanding of neutrinos and their role in our universe. However, as we begin to study neutrinos more closely and specify their characteristics, we need more control. This is where we are introduced to the class of accelerator-based neutrino experiments. A more detailed description of the contents in this Chapter can be found in [12].

### 2.1 Accelerator-Based Neutrinos

Using particle accelerators to create a neutrino beam is an increasingly favored mechanism of modern neutrino experiments. The greatest benefit to utilizing accelerator complexes comes from the design and control afforded to the researchers. Neutrino beams are carefully designed, often with a specific physics goal in mind, and the energy spectrum and range can be calibrated and tuned. For example, the NuMI Neutrino Beam, discussed in Section 2.2.2, was designed such that it can be run in three different configurations spanning a neutrino energy range of 1-20 GeV.

### 2.2 Fermi National Accelerator Laboratory

Fermi National Accelerator Laboratory, affectionately known as Fermilab, is a United States Department of Energy National Laboratory located just outside Batavia, Illinois. For 50 years, it has served as a world leader in accelerator physics, particle physics, and specifically neutrino physics.

### 2.2.1 Fermilab Accelerator Complex

Fermilab's Accelerator Complex fuels the NuMI neutrino beam with 120 GeV protons from the Main Injector. The following section outlines the operations of the Accelerator Complex and the creation of the NuMI beam. A more detailed description can be found in [12]. Until August 2012, the starting point of the accelerator complex was a Cockroft-Walton generator. This was replaced by a radio-frequency quadrupole (RFQ) and an ion source. Everything begins with pure Molybdenum, no larger than a small chocolate bar, that provides a supply of electrons. This Molybdenum is in a container filled with $H_2$ gas. As the Molybdenum produces electrons, it converts the hydrogen gas to $H^-$ ions. Using a positive potential and guiding magnetic fields, the $H^-$ ions are extracted from the container and focused within the RFQ. The RFQ allows bunches of $H^-$ ions to be made from the continuous stream and each bunch is accelerated from 35 KeV to 750 KeV and supplied to the LINAC (Linear Accelerator). The LINAC accelerates the particle bunches to 400 MeV and the beam enters the Booster. The bunches are 5 ns apart, with the typical pulse length (sum of all bunches) being roughly 20 ms. Just prior to entering the Booster, the pulse passes through a thin carbon foil which strips the atoms of their electrons, leaving only single proton-$H^+$ ions. Operating at a nominal frequency of 15 Hz, the proton bunches travel around the Booster ring about 16,000 times in order to reach a kinetic energy of 8 MeV. The Booster contains 17 radio frequency (RF) cavities operating at a frequency beginning at 37.8 MHz, upon initial extraction from the LINAC, up to 52.8 MHz when the batches are injected into the Main Injection. A Booster "Batch" yields roughly $5 \times 10^{12}$ protons. The beam is either sent to the Booster Neutrino Beam (for low energy neutrino beams) or to the Main Injector (for high energy neutrino beams) and subsequently the NuMI Beamline. Our path follows the Main Injector, where the Booster delivers a maximum of 11 proton batches in about 0.7 s. The Main Injector is a synchrotron that accelerates the protons up to 120 GeV, which takes about 1.5 s.

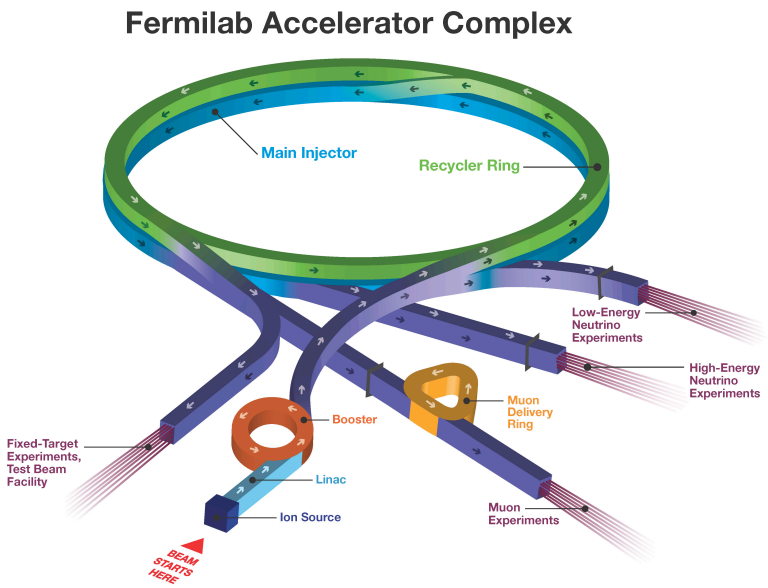


FIGURE 2.1: A schematic view of the Fermilab Accelerator Complex showing the three major acceleration steps: LINAC (light blue), Booster (orange), and Main Injector (green). Figure from [8]

### 2.2.2 The Neutrinos from the Main Injector (NuMI) Beam

The proton batches intended for the NuMI Beamline are extracted from the Main Injector with kicker magnets that changes from an initial zero value to their full field intensity in 700 ns, extracting a beam with an intensity of about $4.2 \times 10^{13}$ protons/spill. The extracted beam is bent downwards by 3.3° in order to aim towards the MINOS far detector in Soudan, Minnesota. Batches are normally extracted every 1.9 seconds with a beam window, or spill, of 8.6 $\mu$s. The proton beam then travels 350m and hits a water-cooled graphite target composed of 47 rectangular segments lined end-to-end, with a cross sectional area of $6.4 \times 18$ mm$^2$. Each rectangular segment is 20 mm in length, 6.4 mm in width, 15 mm in height, and spaced 0.3 mm from each other. The total length of the target is 95.4 cm, corresponding to 1.9 interaction lengths, allowing $\approx 85\%$ of protons to interact. The design and size of the target was

optimized for maximizing pion production and minimizing pion absorption, while maintaining tolerable thermal expansion properties.

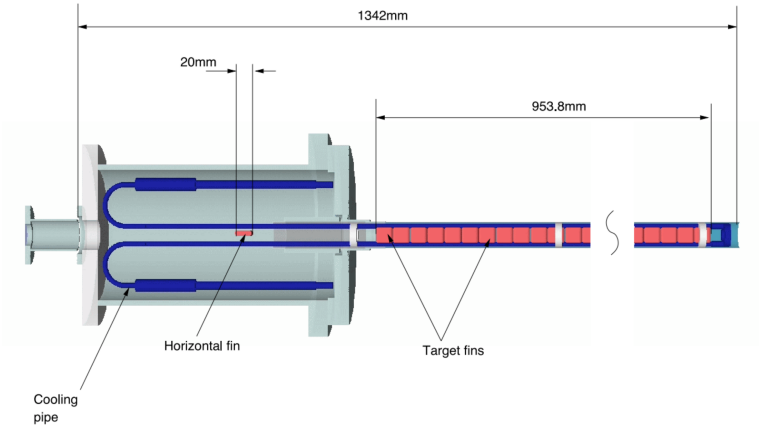


FIGURE 2.2: A longitudinal cross section of the NuMI graphite target. Figure from [9]

The proton-graphite interaction produces several types of particles,

$$p + C \rightarrow \pi^{\pm}, K^{\pm} + X \tag{2.1}$$

The particles created from the proton-graphite interaction are focused or defocused by two magnetic horns. The system is designed to focus the mesons into the decay region and down the beamline. The graphite target is inserted approximately 50cm into the first horn, which is 3.3m long. Located 10m downstream, the second horn is 3.58m long. This configuration and the possible trajectories are shown in Figure 2.3. The horn's toroidal magnetic field goes as $B \sim 1/r$.

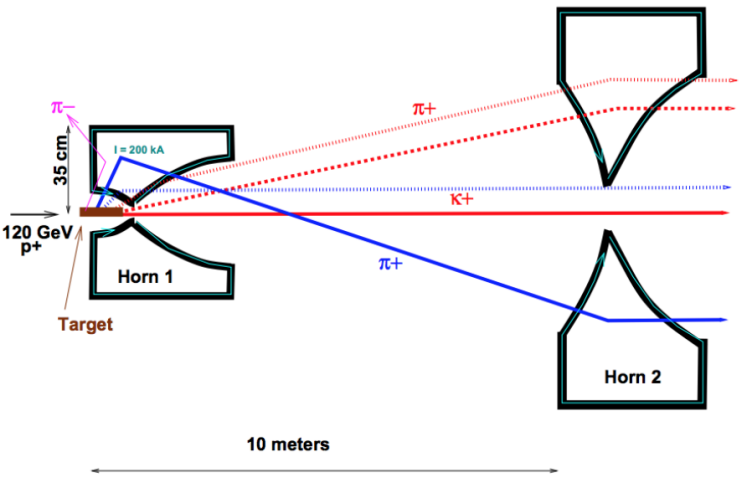


FIGURE 2.3: Possible trajectories through the two NuMI horns. The second horn serves to further focus hadrons that are underfocused or overfocused by the first horn. Figure from [10].

In the forward horn current mode (FHC), the horns focus $\pi^+$, which subsequently produces primarily a muon neutrino beam ($\pi^+ \rightarrow \mu^+ + \nu_\mu$). In the reverse current, the inverse will be created, ($\pi^- \rightarrow \mu^- + \bar{\nu}_\mu$). This can be summed as,

$$\pi^{+(-)} \rightarrow \mu^{+(-)} + \nu_\mu(\bar{\nu}_\mu) \tag{2.2}$$

Charge conservation of the proton-graphite interaction will cause the $\pi^-$ production to be significantly lower than $\pi^+$ production, meaning that the intensity of antineutrinos will be smaller than neutrinos.

The hadrons focused through the horn system then enter a 675 m long, 2 m diameter helium-filled decay pipe. The length corresponds to the decay distance of a 10 GeV pion. Nearly all the unstable hadrons will decay into neutrinos within this pipe.

## 2.3 Neutrino Detectors

A common thread through this thesis is the unique interaction characteristics of neutrinos. Neutrino detectors are the lens through which the neutrino dimension can be

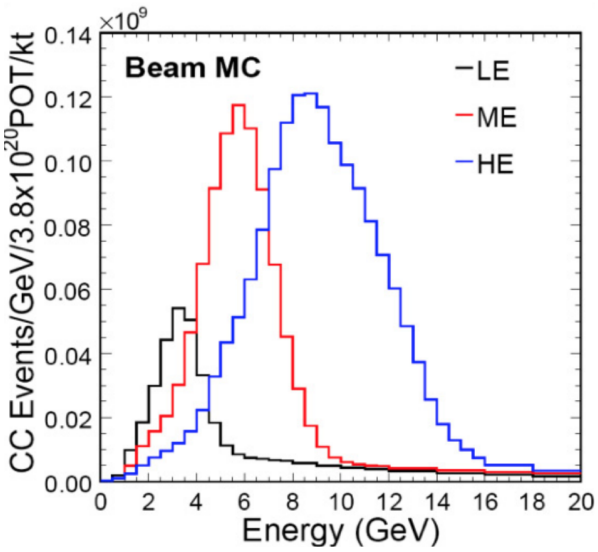


FIGURE 2.4: NuMI neutrino energies at different configurations. The analysis performed for this work is based on the Low-Energy mode, in antineutrino mode. Figure from [9].

viewed. For some neutrino experiments, a neutrino detector is the only equipment needed because natural neutrino sources are available. For accelerator-based neutrino experiments, the neutrino detector is one of the two major components. Neutrino detectors are used to characterize the daughter particles created by neutrino interactions. These particles can be reconstructed and used to identify the flavor, energy, or characteristics of the incident neutrino. A major benefit of accelerator-based neutrino experiments is that many of the important parameters are intentionally designed and known, such as the distance the neutrino traveled or the neutrino's initial direction. A great neutrino detector will have ample statistics and efficiency in detecting neutrino interactions, precise energy reconstruction, and extremely high purity of particle tracks.

### 2.3.1 LArTPC Theory

Liquid Argon Time Projection Chambers (LArTPCs) represents the most advanced neutrino detection technology, leading to it being the detector type of choice for the

US Neutrino Program. LArTPC's are able to accurately reconstruct neutrino energies and flavors with low background noise and systematics. The theoretical concept behind a LArTPC is rather simple, given its immense ability to characterize neutrino interactions.

A LArTPC is a detector filled with liquid argon, usually ultra-pure and cryogenically cooled. When a neutrino interacts with an argon atom inside the detector, it will produce particles. As these product particles travel through the detector medium they will ionize the argon, leaving a track of ion-electron pairs as they pass. Argon, as a noble element, provides the characteristic of being chemically inert. This allows particles to travel through without significant unwanted interactions. The Time Projection Chamber (TPC) is within an electric field, allowing the ions and electrons to be separated. The electrons will drift towards a set of wire planes situated on one side of the TPC. The wire planes are oriented at specific angles in respect to each other. The electron will induce a wire signal pulse on the wire plane, which can be read out and analyzed. There are two important wire planes; an 'induction' plane and a 'collection' plane. The electron will induce a signal on the induction plane and then be collected by the collection plane. The induction plane will give a bipolar signal, due to the electrons approaching the plane and then traveling away from the plane. The collection plane will be unipolar because the electron approached the wire plane and is then collected.

The induction and collection planes are oriented at $\pm 60^{\circ}$ with respect to the beam direction. This orientation is crucial because it allows the combination of the information from both the wire planes to provide a two dimensional projection of the interaction event. An additional dimension can be found by measuring the time it takes the electrons to drift across the detector medium and be collected onto the collection plane. By combining these three measurements, a three dimensional projection of each neutrino interaction can be made. Additionally, as each electron charge is induced and collected by the wire planes, the calorimetric data is stored. This calorimetric data is proportional to the energy deposited by the particle in the detector.

Through the interaction processes, there is also some scintillation light produced in the detector. Some LArTPC experiments utilize Photomultiplier Tubes (PMTs) to gather this light information, which can be used in a variety of analyses and as a trigger to designate $t_0$. For ArgoNeuT, utilizing accelerator neutrinos, the timing of the beam is used to determine $t_0$.

A illustration of the LArTPC concept for detecting neutrino interactions can be seen in Figure 3.2.

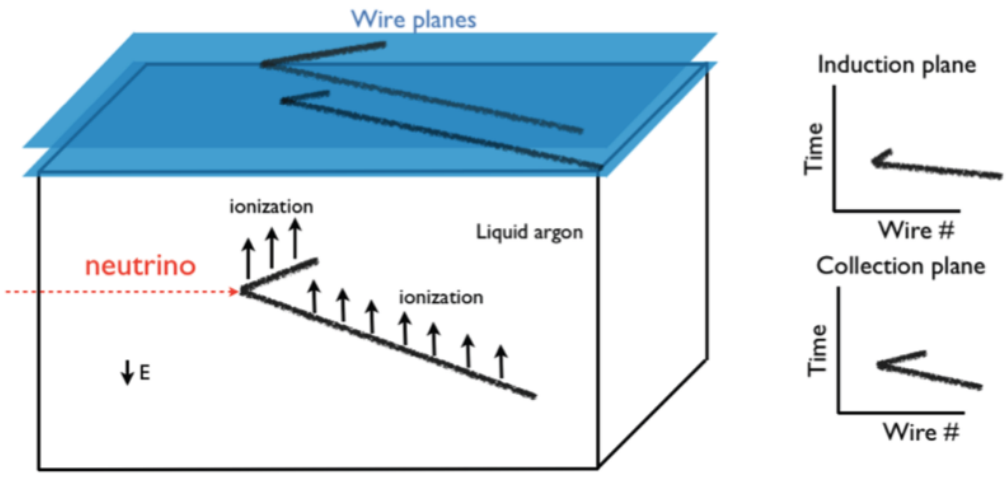


FIGURE 2.5: The LArTPC concept for detecting neutrino interactions. (Left) An incident neutrino enters the detector and strikes an argon atom, producing charged particles that ionize the detector medium as they travel through the detector. This ionization is drifted to the wire planes by the uniform electric field. (Right) The wire planes measures the time in which the charge interacted with the wire, as well as the wire number of the interacting wire. Utilizing the wire orientation, the wire numbers affected, and the timing from both wire planes allows for the reconstruction of a three dimensional image of the interaction, including the calorimetric information. Figure from [11].

Argon provides an optimal medium for neutrino experiments because it has a high density, minimal radiation length, is chemically inert, and produces significant scintillation. The more dense noble gases provide even more benefit, but their small abundance in our atmosphere makes them monetarily unfeasible to use. Argon still

provides the density, while being more abundant and less expensive for neutrino experiments, particular larger LArTPC's such as DUNE that will hold up to 70,000 tons of pure argon. Having argon in liquid form provides more density which increases the likelihood of neutrino interaction, density of ionization, and less diffusion of electrons as they drift, allowing for more resolved track reconstruction. Liquid argon also contains dielectric properties that perform better in the TPC's high voltage environment. The benefits of argon over the other noble gases can be seen in Figure 2.6. In Figure 2.7, a collection plane in ArgoNeuT for a neutrino event is shown. The

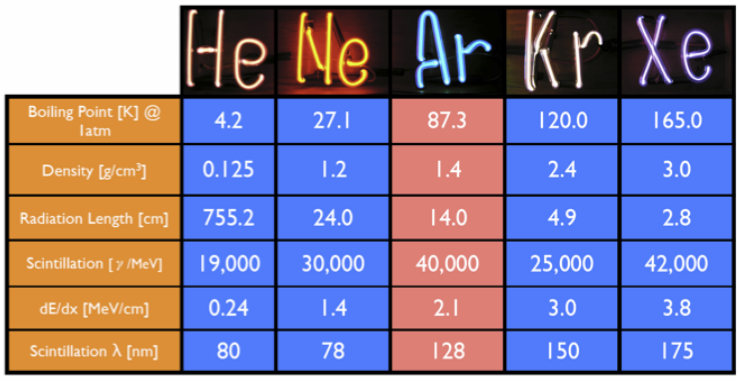


FIGURE 2.6: A table displaying the most relevant characteristics, in relation to particle detectors, of the stable noble elements. Argon represents the best possible detector medium when reconciling price per mass. Figure credit: Mitchell Paul Soderberg.

signal shown is in what is known as a wire-time view, the two dimensional view of time vs. wire number, and the colors designate the amount of charge deposited on a certain charge at that time. Below the collection plane is a view of the signal on the collection plane (in ADC counts) as a function of time.

There is a region of specific balance in the electric fields between the drift region and the induction wire plane (space 1), as well as between the induction and collection planes (space 2). The implication of this is that in order to gain the greatest grid electron transparency, an electron will drift from space 1 to space 2 only with a delicate

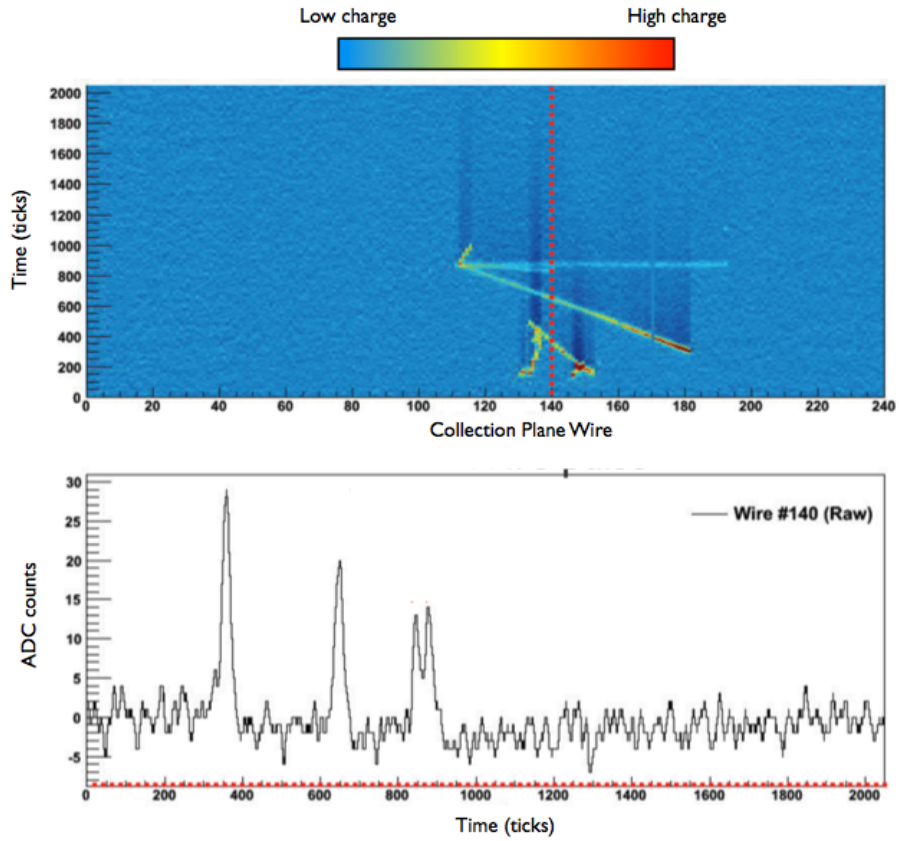


FIGURE 2.7: (Top) The Collection Plane showcasing a neutrino interaction. Wire 140 is shown in red. (Bottom) ADC counts vs. Time ticks for Wire 140. Figure from [1].

ratio of the electric fields $E_1$ and $E_2$ [35]. The transparency condition gives:

$$\frac{E_2}{E_1} > \frac{1+\rho}{1-\rho} \tag{2.3}$$

where $\rho = \frac{2\pi r}{a}$ and $r$ is the wire radius and $a$ is the space between the wires. Many LArTPCs, including ArgoNeuT, use an additional wire plane known as a "shield" plane that separates the drift volume from the induction and collection plane. This shield plane serves to protect the induction and collection planes from receiving any charge other than the ionization that enters the wire plane region. In order to maximize this effect of shielding the two wire planes, the shield plane must satisfy:

$$\frac{a}{2\pi s}\ln\left(\frac{a}{2\pi r}\right) \sim 1 \tag{2.4}$$

where $s$ is the distance between the shield plane and the induction plane.

The shield plane also can serve as a way to shape the field near the wire planes. Additionally, if used to read data, it can provide another source of information and assist in the three-dimensional reconstruction of an interaction. For ArgoNeuT, the induction and collection planes are used to take data. In Figure 2.8, you can see all three planes (shield, induction, and collection), as well as the three drift regions created with the electric field ($E_1$, $E_2$, and $E_3$). Each of the three regions are selected to have a certain wire thickness and spacing in order to satisfy Equation 2.3, while the spacing between the planes is selected to satisfy Equation 2.4.

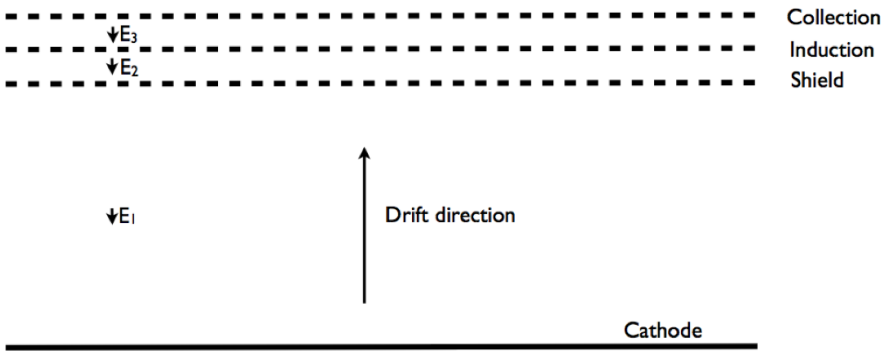


FIGURE 2.8: A LArTPC's drift regions and wire planes. Figure from [12]

### 2.3.2 Calorimetry

As discussed in the previous section, the amount of charge detected at the wire planes is directly proportional to the amount of energy deposited by the traveling particle in the liquid argon. By measuring the amount of energy deposited by a stopping particle, we know the kinetic energy of that particle, which can be an incredibly powerful tool to identify particles. During cases where the particle stops within the detector, it is possible to use the measure of the energy deposited along a track per unit length, $\frac{dE}{dx}$ as a way of differentiating particles from each other. This is best shown in Figure 2.9.

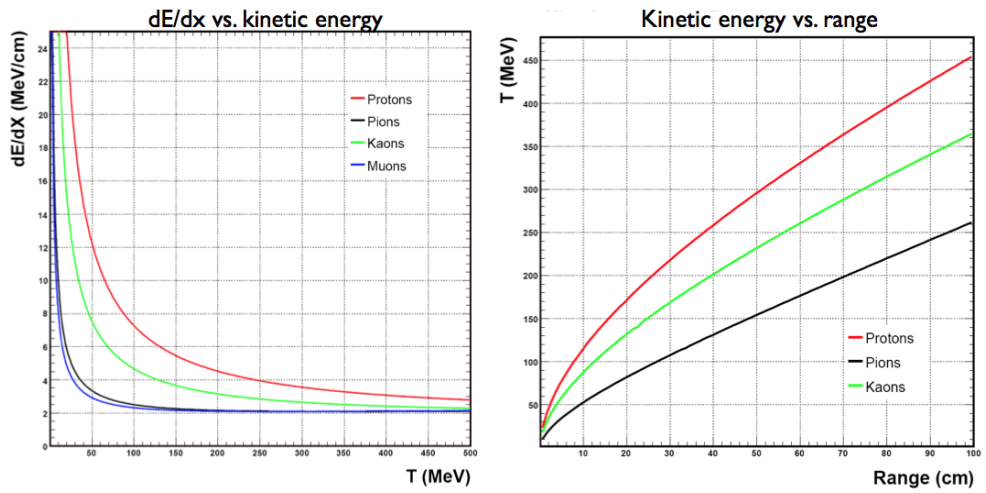


FIGURE 2.9: (Left) $\frac{dE}{dx}$ versus kinetic energy. (Right) Kinetic energy versus track range for a variety of relevant particles. Figure from [13]

A prime example of the power of differentiating particles with LArTPCs is the separation of electrons and photons (gammas). Traditionally this is a very difficult process, due to their decay processes. An example of why this is a problem is reconstructing a photon as an electron is one of the dominating backgrounds for signaling electron-neutrino events in oscillation experiments.

In order to differentiate gamma-induced electromagnetic showers from electron-induced ones requires using $\frac{dE}{dx}$ to discriminate. The $\frac{dE}{dx}$ of a gamma-induced electron-positron pair track is approximately twice as energetic as the electron-induced track. This fact can be used and one can measure the $\frac{dE}{dx}$ and determine the particle's identity before the electromagnetic shower of the track begins and the track becomes too difficult to characterize.

In order to convert the collected charge to $\frac{dE}{dx}$, you must know the preamplifier/-electronics calibration factor, the level of ionization-attenuating impurities in the medium, the effect of ionization-attenuating recombination of electrons with argon ions, the efficiency of the charge collection, and the orientation of the track. Knowledge of the preamplifier/electronics calibration factor is necessary to convert ADC

counts into charge. The ionization-attentuating impurities in the medium is referring to impurities that affect the ionization, such as having electronegative $H_2O$. This is discussed in greater detail in Section 3.1.2. The ionization-attenuating recombination of electrons with ions refers to the possibility that a liberated ionization electron could be recaptured immediately following creation by an argon ion via electrostatic pull. This effect is characterized by the charge density and the applied electric field, with the ability to remove an election-ion pair at higher values.

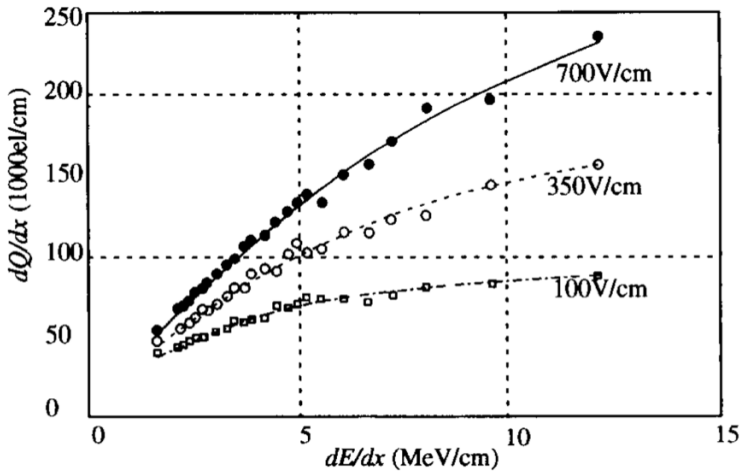


FIGURE 2.10: The effect of recombination in converting charge deposited into energy deposited, shown for a few electric field values. Figure from [14]

If we consider the recombination effect in isolation, we can say,

$$\frac{dQ_{\text{cor}}}{dx} = A\,\frac{(dE/dx)}{1+K_B(dE/dx)} \tag{2.5}$$

where $Q_{\text{cor}}$ is the corrected charge and $A$ and $K_B$ are constants (in a given electric field). Equation 2.5 is commonly referred to as Birk's law. The constants $A$ and $K_B$ have been measured by [14] at a spectrum of voltages standard of LArTPC-based experiments.

## 2.4 Experimental Challenges

ArgoNeuT is a research and development (RD) project at Fermi National Accelerator Laboratory. It served as the first phase of the US neutrino program, moving towards the future kilo-ton scale LArTPCs. ArgoNeuT helped characterize the performance of LArTPCs, providing a testing ground to flesh out the advantages, disadvantages, and areas of concern for larger LArTPC experiments.

Challenges not addressed in this section, such as those with signal processing, automatic reconstruction, and data analysis. These challenges will be discussed in detail in Chapter 4.

### 2.4.1 Liquid Argon Purity

The liquid argon required for the effective use of LArTPCs must be thousands of times more pure than commercially available argon. This is a requirement to have minimal charge attenuation and to allow electrons to drift the full distance to the anode. The experimental process of purifying the liquid argon for ArgoNeuT is discussed in Chapter 3 in detail. The larger the LArTPC, the greater challenge it will be to maintain purity. For example, a 20Kt LArTPC will have a drift distance of roughly 10m. Therefore, the liquid argon must be pure enough for a liberated ionization electron to drift 10m without interacting with an impurity. This problem is possible subverted by the concept of a segmented TPC that has multiple drift regions of roughly 2-3m. The cost of a segmented TPC is that you decrease the number of readout channels possible for the TPC.

### 2.4.2 Liquid Argon Safety

Liquid argon is a noteworthy safety hazard in general, but particularly in confined spaces. While argon is a noble gas and would not pose a serious health hazard to humans, if a significant amount of liquid argon were to be spilled in an enclosed space, it can quickly expand into a gas and replace the oxygen in the space. Safety designs that manage the potential for an underground spill of liquid argon are a challenge, as is devising a method to fill underground tanks with liquid argon. These challenges increase as the size of the LArTPC increases. ArgoNeuT deploys gas relief lines that would direct the spilled argon from the underground enclosure to the ground level. In addition, there are also oxygen deficiency alarms, spill containment vessels, slow control monitors that measure temperature and pressure, and more.

### 2.4.3 Light Collection

Interactions with liquid argon produce scintillation light that can be readily read out with detectors. This scintillation light can be used as a trigger to designate the start time of a neutrino interaction and is particularly useful in analyses that do not involve a timed neutrino beam. For future LArTPC experiments, having light detection capabilities with resolutions up to nanoseconds is an important characteristic.

There are two main processes that produce scintillation light:

$$\begin{aligned} Ar^* + Ar &\rightarrow Ar_2^* \rightarrow 2Ar + \gamma, \\ Ar^* + Ar &\rightarrow Ar_2^+ + e^- \rightarrow Ar_2^* \rightarrow 2Ar + \gamma. \end{aligned} \tag{2.6}$$

The first process is known as self-trapped exciton luminescence, created when an excited argon atom, generated by the production of a charged particle in the neutrino interaction, forms a molecular pair with a neighboring argon atom. This molecular pair de-excited by producing a photon. The second process is known as recombination luminescence, created when an argon ion, generated by the production of

a charged particle in the neutrino interaction, recombines with a neighboring argon atom to form a molecular ion. This molecular ion then breaks apart and is de-excited by producing a photon. In both processes a photon with a wavelength of 128nm is produced. This photon is very difficult to detect with a conventional photomultiplier tube because they have low transmittance at that wavelength. This can be solved by using high transmittance glass or using a wavelength shifter to shift the light into the visible spectrum.

## 2.5 Current and Future LArTPCs

The United States accelerator-based neutrino physics programs has chosen LArTPC detectors as the main detectors for their future neutrino field studies. LArTPCs provide complete 3D imaging, precise calorimetric energy reconstruction, efficient particle identification and allow the recognition of exclusive topology and the investigation of nuclear effects in detailed studies into the hadronic phase of the final states. These characteristics make LArTPCs the ideal detector for few-GeV neutrino scattering measurements. ArgoNeuT, the LArTPC this study was conducted on, was the first LArTPC in a neutrino beam in the United States and started the US LArTPC neutrino program. ArgoNeuT collected data on the NuMI beam from 2009-2010. During this period, the LArTPC known as MicroBooNE was proposed and commissioned. MicroBooNE is currently taking data on the Booster Neutrino Beam (BNB) on the Fermilab site. Over the next few years two detectors will be joining MicroBooNE in formal data taking, the Short-Baseline Near Detector (SBND) and the ICARUS-T600 detector. These three detectors will form a detector chain known as the Short-Baseline Neutrino Program (SBN). This program is providing crucial research and feedback that will feed into the US Neutrino Programs flagship detector, known as the Deep Underground Neutrino Experiment (DUNE). DUNE will be the largest neutrino detector ever built, designed as a four cryostat detector that will hold a combined 68,000

tons of liquid argon. DUNE is still in the design phase but will eventually serve as part of the Long-Baseline Neutrino Program as the far detector.

# CHAPTER 3

# The ArgoNeuT Experiment

This chapter will detail the specific hardware aspects of the ArgoNeuT Experiment. A more detailed description of the contents in this Chapter can be found in [15].

## 3.1 ArgoNeuT Hardware

The major piece of hardware in the ArgoNeuT Experiment is the Time Projection Chamber (TPC). On one side of the TPC is the cathode plane, while the other side contains the three parallel wire planes that consist of the anode. Equally as important as the TPC is the cryostat, electronics readout, and MINOS Near Detector. The purity, containment, and cooling of the liquid argon is vital to the efficiency of the experimental data. The proper extraction of the raw data and the electronics readout to filter and amplify signals provide the ability to analyze the data properly. Finally, for through-going particle tracks, utilizing the MINOS Near Detector provides significant resources to deepen the possible analyses. Together with the TPC, these hardware components provide crucial abilities to the experiment to allow for our studies. Each of these hardware elements will be discussed in detail in the sections following.

### 3.1.1 Cryostat and Cryocooler

The needs of the LArTPC to be continuously filled with ultra-pure liquid argon requires a storage and maintenance system for the liquid argon. The liquid argon is maintained in a cryostat, which consists of an inner and outer vessel. The cryostat is cylindrical in shape and has convex end-caps at each end. The end caps are the access points to the internal volume for the installation of the detector. The length of

the inner cryostat is 130 cm, with a diameter of 76.2 cm, giving a liquid argon volume of 550 L (0.76 tons). The length of the outer cryostat is 163 cm with a diameter of 106.7 cm. In between the inner and outer cryostat's is a thick layer of vacuum insulation that was maintained at a pressure of $10^{-3}$ - $10^{-4}$ torr throughout the physics run. The major axis of the cryostat is parallel to the NuMI beam axis.

The neck of the cryostat is wide and consists of a partially vacuum jacketed chimney that is formed through two stainless-steel, coaxial straight-joints assembly. This chimney is oriented on the top of the cryostat. The chimney provides access to the TPC's signal wires and internal instrumentation, while also containing the pipes for the high voltage feedthrough and re-circulation.

To maintain the argon in its liquid state within the cryostat at a constant temperature of 88 K, a commercial single-stage cryocooler with high cooling capacity is used. Flexible lines are used to connect the separate compressor package and the cold head expander. The compressor package is water cooled and supplies compressed helium for the cold head. Once inside the cold head, the helium expands and creates cryogenic temperatures.

The copper heat exchanger is contained in a small vacuum insulated vessel, connected via a four-pipe vertical pathway to the cryostat. Any argon that is boiled off will move vertically through a pipe and is recondensed within the heat exchanger vessel. Once recondensed, the liquid argon travels back through another one of the three pipes to return to the active volume. There is a bypass pipe and two argon filters making up the three passes. The bypass pipe is closed during operation of the detector and only one argon filter is used.

The inner and outer vessels have a number of temperature and pressure sensors that create a feedback loop with the heaters within the volume. A constant 2.0 psig pressure in the area above the liquid is maintained by a system of slow-control software. The feedback loop is such that when the pressure lowers below a threshold,

the heaters on the cryocooler start and the net cooling power lowers. If the pressure increases, the heaters decrease and the net cooling power increases.

A screenshot of the slow-control software is shown in Figure 3.1.

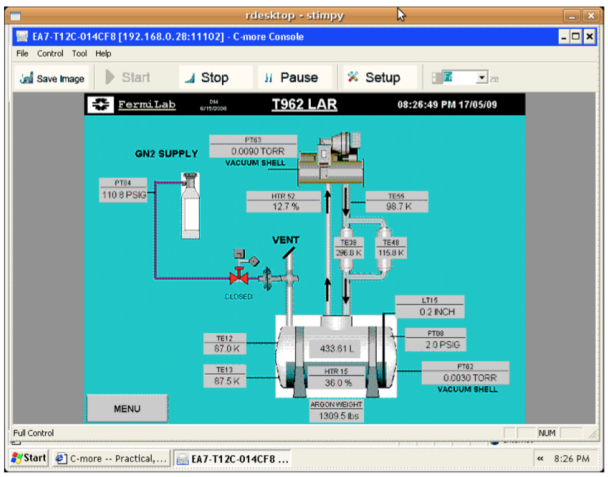


FIGURE 3.1: A screenshot of the remotely controllable cryostat monitoring software. Figure from [15].

### 3.1.2 Time Projection Chamber

ArgoNeuT is a rectangular Time Projection Chamber (TPC) measuring $40 \times 47 \times 90$ cm$^3$, which corresponds to an liquid argon active volume of 170 L, and lies within the inner cryostat. The TPC is built of G10, consisting of woven fiberglass and an epoxy resin binder.

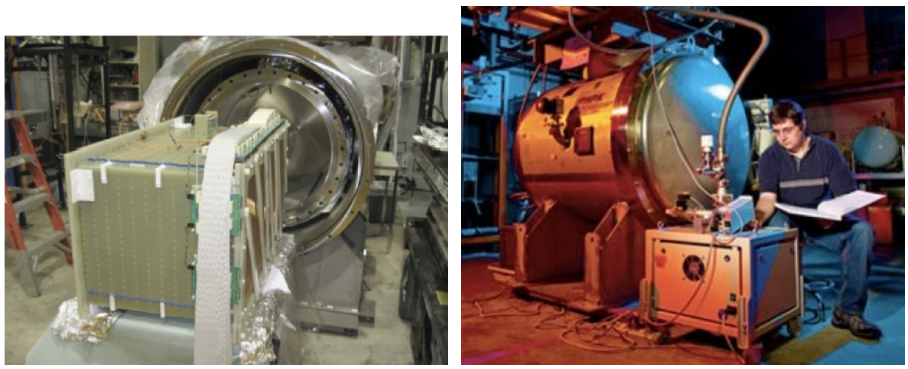

FIGURE 3.2: (Left) ArgoNeuT TPC removed from the inner cryostat with the wire planes and read-out electronics exposed on the right side. (Right) the ArgoNeuT cryostat. Figures from [15].

The TPC is oriented within the cryostat in such a way that the longest dimension is parallel with the beamline. This gives the dimensions of the wire planes to be $40 \times 90$ cm$^2$, with a drift distance horizontal to the ground of 47 cm from the cathode plane to the innermost wire of the first anode plane. The cathode plane is a sheet of G10 with metallized copper on the inner surface. The wires are constructed from a beryllium-copper alloy, with a diameter of 152 $\mu$m. They were strung at a tension of 9.8 N, with a 4 mm spacing (known as pitch). This pitch is constant in all wire planes. As discussed previously, the anode consists of three parallel wire planes separated from one another by 4 mm away.

The first plane in the anode is the ”shield plane", consisting of 225 wires oriented perpendicularly to the beam axis (+90 degrees). Due to the orientation of the wires, each wire is 40 cm. The shield plane is not instrumented to readout any data, but rather provides the shape to the electric field in the anode region and shield the electronics and other instrumented planes from induction signals produced by ionization. The second plane in the anode is the “induction plane", consisting of 240 wires oriented at +60 degrees relative to the beam axis. A bipolar signal is produced as ionization electrons travel towards, cross, and then travel away from the induction plane. The third plane in the anode is the “collection plane", consisting of 240 wires oriented

at −60 degrees relative to the beam axis. After the ionization electrons pass the induction plane, they are collected onto the collection plane and produce a unipolar signal. Due to the orientation to the beam axis, the wire lengths of the induction and collection planes vary, starting as long a 46.2 cm in the middle of each plane and decreasing in length to fill the corners of each wire plane.

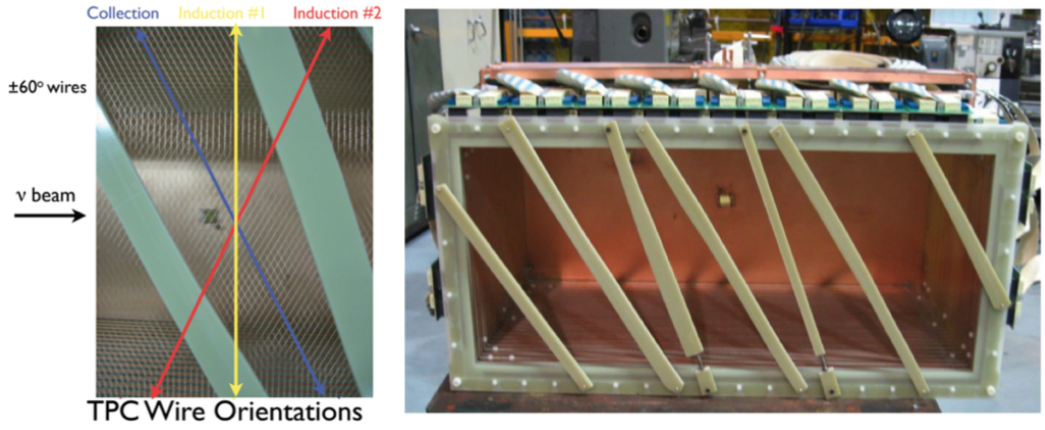


FIGURE 3.3: (Left) ArgoNeuT's anode wire plane orientation. (Right) Fully assembled TPC. Figure from [12].

The drift region of the TPC is maintained in an electric field of 500 V/cm. This is done through key electrodes placed on the boundary surface surrounding the drift volume, shaping the field. Around the TPC are four panels that have 1 cm copper strips that run up the entire length of the TPC. These strips are equally spaced 1 cm apart to form 23 rectangular bands around the TPC. The copper strips are placed at potentials that linearly decrease from the cathode to the shield plane, shaping the field to be uniform in the drift volume and near the edges of the TPC volume. This allows ionization electrons to drift through the volume at a constant velocity.

FIGURE 3.4: Inside the ArgoNeuT TPC. The copper strips lining the TPC is shown, attached to the G10 TPC frame. The solid copper sheet shown is the cathode plane. Figure from [15]

### 3.1.3 Electronics Readout

The charge information is read out from each individual wire continuously by a multi-channel waveform reader, consisting of three electronics cards and boards. These are a bias voltage distribution card (BVDC), preamplifier and filter card (PFC-16), and the ADC, circular memory buffer, and VME readout digitizer module (ADF-2). Each element is connected via internal readout cables, signal feedthrough card, external readout cables, and pleated foil cables. The bias voltage is created from a noise-filtered external DC power supply. This is daisy-chained to the BVDC, which then is passed through another noise filter and distributed amongst the sense-wires of the TPC, using a 100 MΩ isolation and current limiting resistor. To limit ground-loop currents, the daisy-chains' ground bus is isolated from the signal through 100 MΩ resistors. The BVDC, including the mounted resistors and capacitors, are submerged in the liquid argon inside the cryostat. Each BVDC can service 24 wires, connecting to them through 12-pin connectors. It has been observed that the BVDC does not effect the electron lifetime. When the BVDC receives a signal from a wire, the signal

is transported through 20 internal readout flat cables up to the cryostat chimney to the inner side of the signal feedthrough.

The bridge between the vacuum-tight cryostat and the exterior is the readout signal feedthrough, which is custom-built to provide board-mount connectors on the inside and outside of the cryostat. After the signal travels through the signal feedthrough outside the cryostat, it is transferred to the 16 channel preamplifier and filter card (PFC-16). Consisting of two stages, a preamplifier stage and shaping/filter stage, the PFC-16 cards are contained in a double RF shielded cage. After the signal has been amplified and filtered, it is transported along pleated foil cables to a set of 32-channel ADF-2 modules where it is digitized. Each ADF-2 module contains a 10 bit analog-digital converter and is capable of handling sampling frequencies of more than 100 MHz. For ArgoNeuT, the ADF-2 sampled the preamplifier every 198 ns and recorded the digital information for 2048 samples, or time ticks. With a maximum drift time of 333 $\mu s$, having a recording time window of 405 $\mu s$ allows events to be pre- and post-sampled.

### 3.1.4 Liquid Argon Purification and Purity Measurements

Due to the importance of the purity of the liquid argon, the purification and measurement processes are carefully monitored. One of the greatest threats to argon purity is the presence of electronegative molecules. As the impurity concentration increases, the electron lifetime decreases, as shown,

$$\frac{1}{\tau_e} = k_e[O_2] \tag{3.1}$$

The oxygen equivalent $[O_2]$ concentration is often used for the total concentration of electronegative impurities, expressed in units of parts-per-billion (ppb). The attachment processes rate constant $k_e$ is dependent on the TPC's electric field. For example, if $k_e \simeq 3.1$ ppb$^{-1}$ms$^{-1}$, then the corresponding electric field is 0.5 kV/cm and the

drift velocity of the electrons is 1.6 mm/$\mu$s [36]. When the impurity concentration reaches 0.7 ppb (and $\tau_e = 450\mu$s), it only takes 310 $\mu$s, or a 50 cm drift, to remove half of the free ionization electrons.

Commercially available liquid argon typically comes with an oxygen-equivalent concentration in the parts-per-million range, so in order to conduct the ArgoNeuT experiment, a purification system had to be built to remove impurities that would stop ionization electrons from drifting the length to the wire planes. A purification system required a high removal efficiency, while still be fast enough to purify large amounts of argon to continuously feed the TPC. One of the most efficient ways of removing oxygen from an inert gas stream is by utilizing the oxidation reaction with a metal to form a metal oxide. Doing this removes the oxygen from the gas stream and is temperature and pressure dependent. Once a filter becomes saturated with oxygen, regenerating the metal form from the metal oxide allows the process to be restored. This can be done by heating the filter with a flow of hot inert gas that contains 2-4% $H_2$ by volume. ArgoNeuT utilizes a custom-made filter of this type.

ArgoNeuT's filters are built from activated-copper-coated alumina granules, contained inside of flanged cylindrical stainless-steel cartridges. At each end of the cartridge are liquid argon inlet/outlet flange-fitted lines, using vacuum tight cryogenic valves. Steel disks are placed at both ends of the internal volume of the cartridge to keep the granules inside while allowing liquid argon to flow through. The dimensions of each cartridge is 61 cm in length with a diameter of 6.4 cm, giving a roughly 2 L volume. The cartridges alumina are porous enough to provide a large active copper surface with which $O_2$ can react. The cartridges also allow for molecular trapping of $H_2O$, another impurity linked to a low electron lifetime. Each cartridge is insulated by being wrapped in fiberglass, as well as being maintained at a weak vacuum of 100-200 torr in the recirculation system.

Figure 3.5 shows the contained cryosystem. Once a filter is saturated, the other filter is used while the saturated filter is regenerated. Argon that is boiled off the liquid

surface travels up to the cryocooler, where it is condensed. Once in liquid form, gravity and pressure pushes the liquid through a filter and re-enters the cryostat volume. The recirculation flow rate is roughly 1.6 L/hr/L (LAr volume per unit time per unit volume of the filter), which corresponds to the full volume (approximately 550 L) recirculation every 7-8 days.

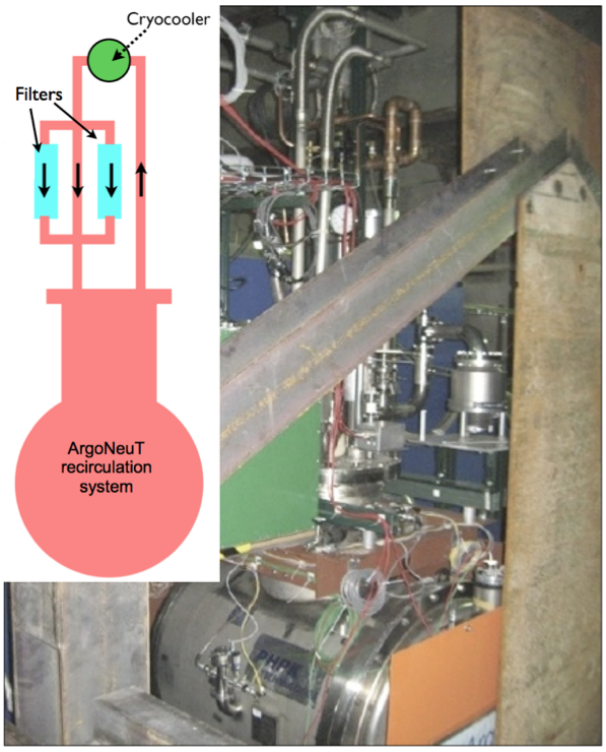


FIGURE 3.5: The ArgoNeuT experiment during a physics run. (Inset) A drawing of the ArgoNeuT recirculation system, including the cryocooler and two liquid argon filters. Figure from [12].

On top of the TPC, inside the cryostat, is the liquid argon purity monitor. The monitor provides instantaneous measurements of the argon purity, although with high systematics. Using measurements spanning the course of several days can provide a general purity trend. Figure 3.6 shows the general concept of monitoring the argon purity. The process begins by shining a Xenon flash lamp, outside the cryostat, to the inside via optical fibers and is directed towards a gold photocathode on the purity monitor. The photoelectrons produced in the photon-gold interaction drift through the field cage of the purity monitor and are detected at an anode roughly 10 cm away.

Using an oscilloscope to compare the signals at the cathode and anode allow for the determination of the level of ionization attenuation across the drift distance. If the signals from the cathode and anode are equal and opposite (after accounting from the differing readout responses), then the purity is infinite.

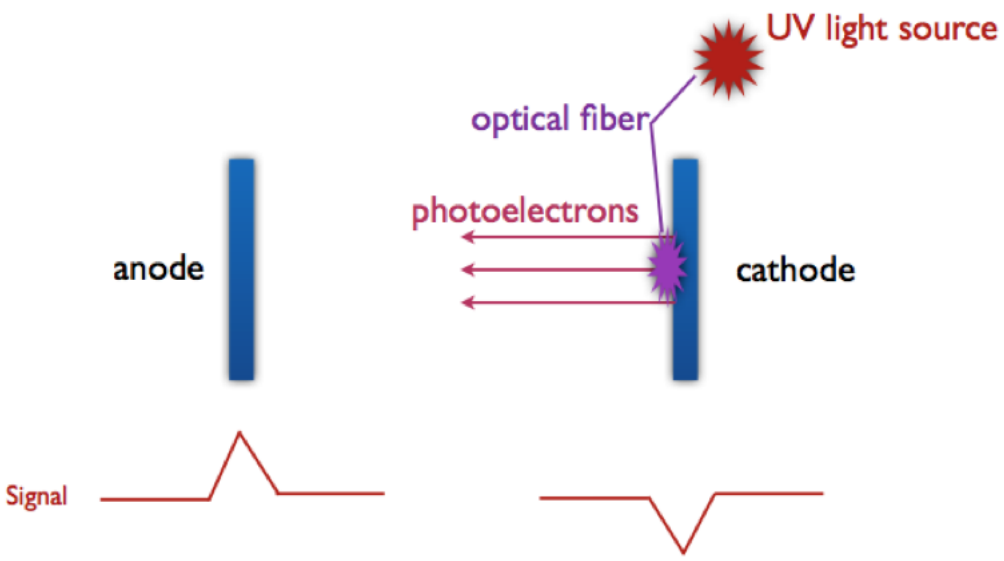


FIGURE 3.6: The purity monitor concept. Since the anode and cathodes are separated by time, comparing the signals can determine the electron lifetime, which is a measure of the argon purity. Figure from [12]

The electron drift time and the electron lifetime can be related by,

$$\frac{Q_{\text{anode}}}{Q_{\text{cathode}}} = e^{\frac{-t}{\tau}} \tag{3.2}$$

where $Q_{\text{anode}}$ and $Q_{\text{cathode}}$ are proportional to the anode and cathode pulse heights respectively. Using a program that utilizes peak-finding techniques, a purity monitor oscilloscope determined the electron lifetime automatically. To account for the electronics signal response, an exponential decay is fit to the signal.

The electronegative impurity concentration in liquid argon can be expressed as [36],

$$\frac{d[e]}{dt} = -k_s[S][e] \tag{3.3}$$

where $[S]$ is the electronegativity impurity concentration, $[e]$ is the electron concentration, $t$ is time, and $k_s$ is the attachment rate constant for electrons.

Solving equation 3.3 gives,

$$[e(t)] = [e_0]e^{-k_s[S]t}, \tag{3.4}$$

or

$$\frac{Q_{\text{anode}}}{Q_{\text{cathode}}} = e^{-k_s[S]t}. \tag{3.5}$$

If one solves the two equations for $[S]$, a relation between the electron lifetime and electronegative impurities arises,

$$[S] = \frac{1}{35k_s\tau} \tag{3.6}$$

where $[S]$ is given in a unit of a molar fraction. In ArgoNeuT, running in neutrino-mode, an electron lifetime is typically 750 $\mu$s, which corresponds to an oxygen-equivalent electronegativity impurity concentration of 400 ppt.

### 3.1.5 MINOS Near Detector

MINOS is a long-baseline neutrino experiment with near and far detectors exposed to the NuMI neutrino beam. The Near Detector sits at Fermilab, just upstream of ArgoNeuT, and the Far Detector is 735 km downstream in the Soudan Mine in northern Minnesota. ArgoNeuT utilizes the MINOS Near Detector to measure the momentum and charge values of muons that exit the ArgoNeuT TPC and enter the Near Detector.

The MINOS Near Detector is a 980 ton magnetized steel and scintillator tracking calorimeter. The detector consists of alternating layers of steel and scintillator, sandwiched together to make the detector 3.8 m high, 4.8 m wide (in an octagon shape), and 16.6 m long. There are a total of 282 steel planes in the detector, each 2.54 cm

thick with a 1 cm thick plastic scintillator attached. There is a 2.54 cm distance between each steel-scintillator pair and the next one. Each scintillation layer is oriented 90 degrees with respect of the previous layer, in order to ease three-dimensional reconstruction. The NuMI beam is off center horizontally, shown in Figure 3.7. Every 5th layer, in the first 150 layers, is fully covered in scintillator, while the preceding four only have scintillator on the beam-centered side of the detector. This is down in the first 150 layers because this region is used to measure the energy of hadronic showers and requires more fine instrumentation. This section is known as the 'calorimeter'. Downstream from the calorimeter is the 'spectrometer', which provides muon tracking. The underlying concept is that a neutrino will interact in the calorimeter region and produce a muon (in the case of charge current muon neutrino interactions) that travels to the spectrometer region and is fully reconstructed.

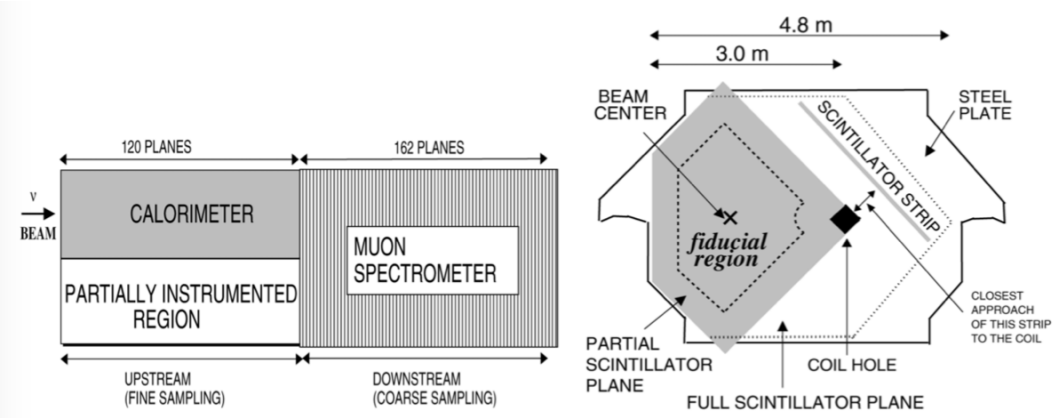


FIGURE 3.7: (Left) The MINOS Near Detector regions, as used by the MINOS experiment. (Right) The plane configuration of the MINOS detector. Figure from [16]

The detector sits in a toroidal magnetic field averaged at 1.3 T, which is produced by a coil of current-carrying cables that travel the length of the detector. By magnetizing the detector, a particle's charge and momentum can be determined by using the direction and amount of curvatur of the particles path through the magnetic field.

The scintillation strips consist of polystyrene, with a reflective coating of 85% polystrene and 15% $TiO_2$ by weight. As a particle travels through a scintillator strip, UV light

peaked at 420 nm is produced and absorbed by wavelength shifting (WLS) fibers. The WLS fibers re-emit the light at a wavelength of 470 nm and transport it to the end of the strip where it is fed to a photomultiplier tube via clear wires. This is shown in Figure 3.8.

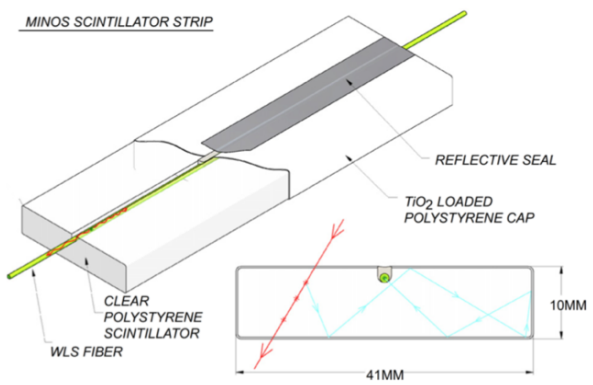


FIGURE 3.8: MINOS scintillation strip concept. Figure from [17].

If muons exit the ArgoNeuT detector, and enter the MINOS Near Detector, there is a chance they can still be fully reconstructed by using both ArgoNeuT's and MINOS's data. For muons higher than 1 GeV, the energy reconstruction resolution $\Delta E_\mu / E_\mu$ can vary from 6% to roughly 13%. Most of the muons produced from the NuMI beam will range out in the MINOS Near Detector, allowing for their full reconstruction by measuring the amount of its curvature in the magnetic field.

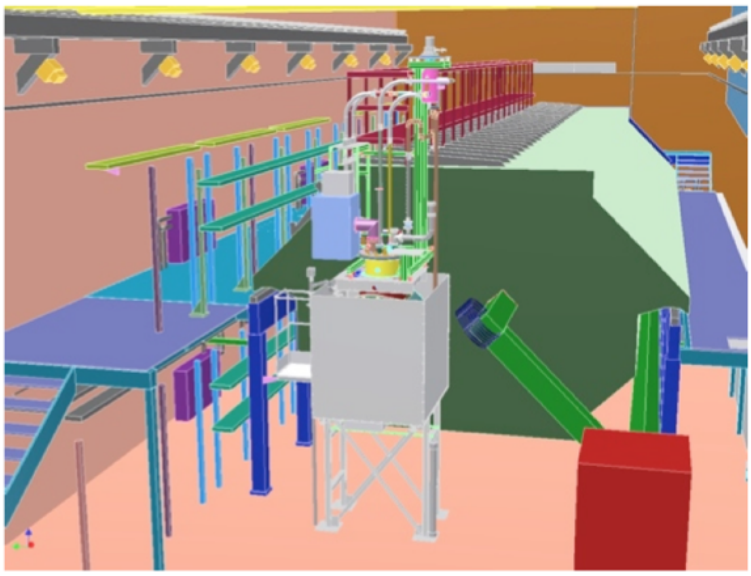

FIGURE 3.9: The position of ArgoNeuT in relation to the MINOS Near Detector in the MINOS Near Detector hall. The ArgoNeuT detector is shown in gray and the MINOS Near Detector is shown in green. Figure from [12].

## 3.2 The Physics Run

The ArgoNeuT detector was commissioned for the physics run in the MINOS Near Detector hall at Fermilab in the Spring of 2009. The TPC was placed inside the cryostat and then vacuum sealed inside. Leak tests were performed on the argon purification system and the TPC was connected to the cryostat.

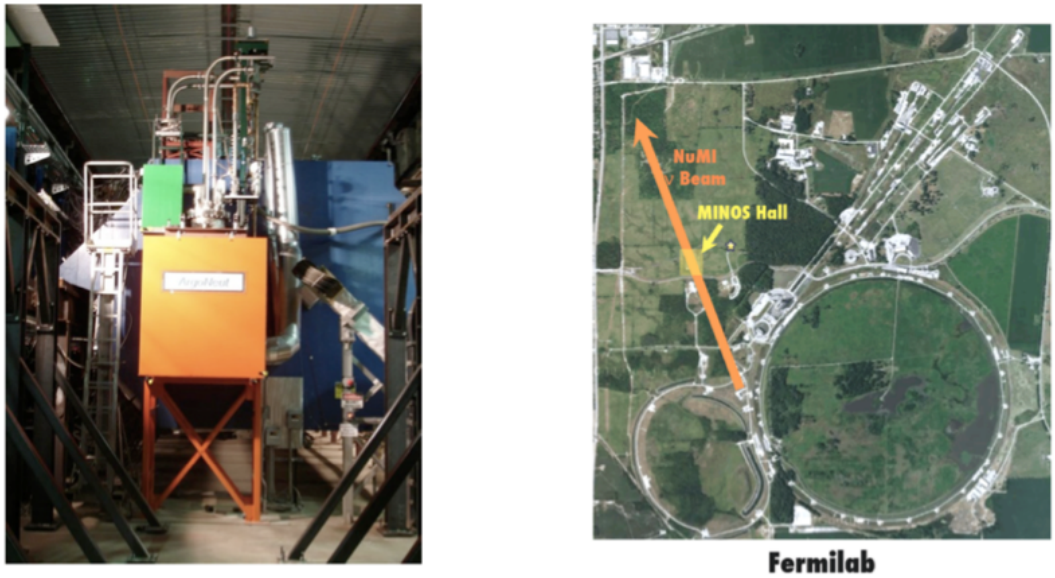


FIGURE 3.10: (Left) The fully instrumented ArgoNeuT detector positioned in the beamline. (Right) An aerial view of Fermilab highlighting the NuMI beam and MINOS hall. Figure from [1].

The conditions for ArgoNeuT's trigger for data acquisition were matched to the NuMI beam spill signal rate of 0.5 Hz. The NuMI accelerator complex provides a time stamp that is recorded into every event record at each trigger. This is used later to match ArgoNeuT tracks with MINOS Near Detector tracks, on a spill-by-spill basis.

The ArgoNeuT physics run began in September 2009 and it gathered data for about six months. The entire run was in the "low-energy" NuMI configuration and the accelerator delivered $1.335 \times 10^{20}$ protons on target (POT). The first phase of the run was in neutrino mode with $8.5 \times 10^{18}$ POT, and the second phase was in anti-neutrino mode with $1.25 \times 10^{20}$ POT. The MINOS Near Detector was operation during the ArgoNeuT run for 90% of the time.

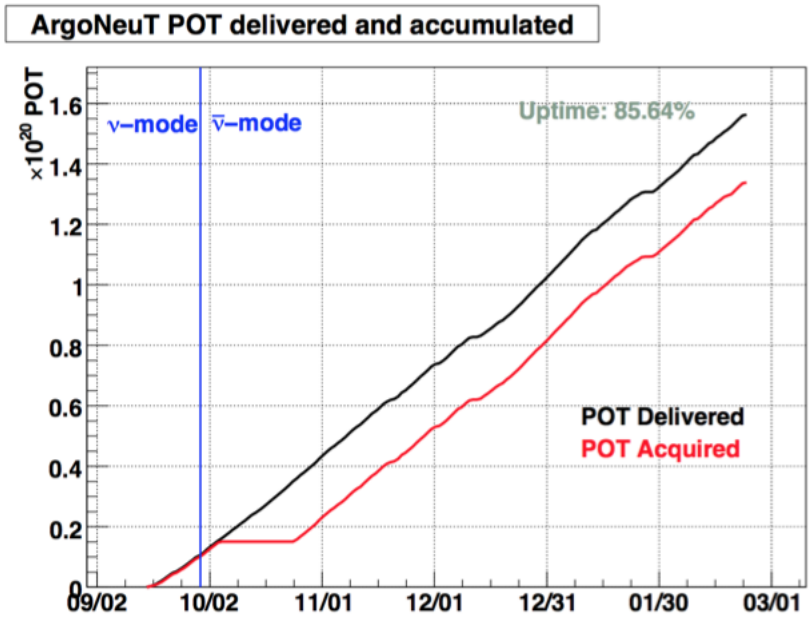


FIGURE 3.11: The ArgoNeuT physics run, in terms of delivered and acquired protons-on-target (POT) as a function of time. The two week suspension in operations was due to a failure of a commercial component of the cooling system. Figure from [15].

# CHAPTER 4

## ArgoNeuT Generation, Simulation, and Reconstruction of Events

Liquid Argon Software (LArSoft) is the software utilized by ArgoNeuT and most LArTPC experiments for neutrino event generation, simulation, and reconstruction. The neutrino event generator allows the creation of final state particles outside the nucleus, which are then transferred to the detector simulation, which propagates them through simulated detector medium and produces simulated ionization electrons. The simulation also models the drift and diffusion of the ionization electrons, the creation of the wire signals, and the electronics response. The simulation also includes the propagation of particles that leave ArgoNeuT into the MINOS Near Detector. A more detailed description of the contents in this Chapter can be found in [1].

### 4.1 Event Generation

ArgoNeuT uses the NUANCE [5], GENIE [37], and NuWro [38] neutrino event generators to generate neutrino interactions with an argon target. The work presented in this thesis utilizes only the NUANCE neutrino event generator software, which has an interaction channel for charge current quasi-elastic neutral hyperon production. There are 99 neutrino/antineutrino interaction channels that correspond to different interaction types that range from 100 MeV to $10^3$ GeV. The channels in the NUANCE Event Generator are shown in Figure 4.1

| # | CC / NC | Reaction |
|---|---|---|
| Cabibbo–allowed quasi–elastic scattering from nucleons | | |
| 1 | CC | $\nu_\mu n \to \mu^- p$ ($\overline{\nu}_\mu p \to \mu^+ n$) |
| (Quasi–)elastic scattering from nucleons | | |
| 2 | NC | $\nu_\mu n \to \nu_\mu n$ ($\overline{\nu}_\mu n \to \overline{\nu}_\mu n$) $\nu_\mu p \to \nu_\mu p$ ($\overline{\nu}_\mu p \to \overline{\nu}_\mu p$) |
| Resonant single pion production | | |
| 3 | CC | $\nu_\mu p \to \mu^- p\pi^+$ |
| 4 | CC | $\nu_\mu n \to \mu^- p\pi^0$ |
| 5 | CC | $\nu_\mu n \to \mu^- n\pi^+$ |
| 6 | NC | $\nu_\mu p \to \nu_\mu p\pi^0$ |
| 7 | NC | $\nu_\mu p \to \nu_\mu n\pi^+$ |
| 8 | NC | $\nu_\mu n \to \nu_\mu n\pi^0$ |
| 9 | NC | $\nu_\mu n \to \nu_\mu p\pi^-$ |
| 10–16 | | Corresponding $\overline{\nu}_\mu$ processes |
| Multi–pion resonant processes | | |
| 17 | CC | $\nu_\mu p \to \mu^- \Delta^+ \pi^+$ |
| 18 | CC | $\nu_\mu p \to \mu^- \Delta^{++} \pi^0$ |
| 19 | CC | $\nu_\mu n \to \mu^- \Delta^+ \pi^0$ |
| 20 | CC | $\nu_\mu n \to \mu^- \Delta^0 \pi^+$ |
| 21 | CC | $\nu_\mu n \to \mu^- \Delta^{++} \pi^-$ |
| 22 | NC | $\nu_\mu p \to \nu_\mu \Delta^+ \pi^0$ |
| 23 | NC | $\nu_\mu p \to \nu_\mu \Delta^0 \pi^+$ |
| 24 | NC | $\nu_\mu p \to \nu_\mu \Delta^{++} \pi^-$ |
| 25 | NC | $\nu_\mu n \to \nu_\mu \Delta^+ \pi^-$ |
| 26 | NC | $\nu_\mu n \to \nu_\mu \Delta^0 \pi^0$ |
| 27 | NC | $\nu_\mu n \to \nu_\mu \Delta^- \pi^+$ |
| 28–38 | | Corresponding $\overline{\nu}_\mu$ processes |
| 39 | CC | $\nu_\mu p \to \mu^- p\rho^+(770)$ |
| 40 | CC | $\nu_\mu n \to \mu^- p\rho^0(770)$ |
| 41 | CC | $\nu_\mu n \to \mu^- n\rho^+(770)$ |
| 42 | NC | $\nu_\mu p \to \nu_\mu p\rho^0(770)$ |
| 43 | NC | $\nu_\mu p \to \nu_\mu n\rho^+(770)$ |
| 44 | NC | $\nu_\mu n \to \nu_\mu n\rho^0(770)$ |
| 45 | NC | $\nu_\mu n \to \nu_\mu p\rho^-(770)$ |
| 46–52 | | Corresponding $\overline{\nu}_\mu$ processes |
| 53 | CC | $\nu_\mu p \to \mu^- \Sigma^+ K^+$ |
| 54 | CC | $\nu_\mu n \to \mu^- \Sigma^0 K^+$ |
| 55 | CC | $\nu_\mu n \to \mu^- \Sigma^+ K^0$ |
| 56 | NC | $\nu_\mu p \to \nu_\mu \Sigma^0 K^+$ |
| 57 | NC | $\nu_\mu p \to \nu_\mu \Sigma^+ K^0$ |
| 58 | NC | $\nu_\mu n \to \nu_\mu \Sigma^0 K^0$ |
| 59 | NC | $\nu_\mu n \to \nu_\mu \Sigma^- K^+$ |
| 60–66 | | Corresponding $\overline{\nu}_\mu$ processes |
| 67 | CC | $\nu_\mu n \to \mu^- p\eta$ |
| 68 | NC | $\nu_\mu p \to \nu_\mu p\eta$ |
| 69 | NC | $\nu_\mu n \to \nu_\mu n\eta$ |
| 70–72 | | Corresponding $\overline{\nu}_\mu$ processes |
| 73 | CC | $\nu_\mu n \to \mu^- K^+ \Lambda$ |
| 74 | NC | $\nu_\mu p \to \nu_\mu K^+ \Lambda$ |
| 75 | NC | $\nu_\mu n \to \nu_\mu K^0 \Lambda$ |

FIGURE 4.1: Channels in NUANCE Event Generator. Figure from [5].

| # | CC / NC | Reaction |
|---|---|---|
| 76–78 | | Corresponding $\overline{\nu}_\mu$ processes |
| 79 | CC | $\nu_\mu n \rightarrow \mu^- p \pi^+ \pi^-$ |
| 80 | CC | $\nu_\mu n \rightarrow \mu^- p \pi^0 \pi^0$ |
| 81 | NC | $\nu_\mu p \rightarrow \nu_\mu p \pi^+ \pi^-$ |
| 82 | NC | $\nu_\mu p \rightarrow \nu_\mu p \pi^0 \pi^0$ |
| 83 | NC | $\nu_\mu n \rightarrow \nu_\mu n \pi^+ \pi^-$ |
| 84 | NC | $\nu_\mu n \rightarrow \nu_\mu n \pi^0 \pi^0$ |
| 85–90 | | Corresponding $\overline{\nu}_\mu$ processes |
| Deep Inelastic Scattering | | |
| 91 | CC | $\nu_\mu N \rightarrow \mu X$ |
| 92 | NC | $\nu_\mu N \rightarrow \nu_\mu X$ |
| 93–94 | | Unused |
| 95 | CC | Cabibbo–supp. QE hyperon production: $\overline{\nu}_\mu p \rightarrow \mu^+ \Lambda$ $\overline{\nu}_\mu n \rightarrow \mu^+ \Sigma^-$ $\overline{\nu}_\mu p \rightarrow \mu^+ \Sigma^0$ |

| # | CC / NC | Reaction |
|---|---|---|
| Coherent / diffractive $\pi$ production | | |
| 96 | NC | $\nu_\mu A \rightarrow \nu_\mu A \pi^0$ $(\overline{\nu}_\mu A \rightarrow \overline{\nu}_\mu A \pi^0)$ |
| 97 | CC | $\nu_\mu A \rightarrow \mu^- A \pi^+$ $(\overline{\nu}_\mu A \rightarrow \mu^+ A \pi^-)$ |
| $\nu$–e elastic scattering | | |
| 98 | – | $\nu_\mu e \rightarrow \nu_\mu e$ $(\overline{\nu}_\mu e \rightarrow \overline{\nu}_\mu e)$ |
| $\nu$–e inverse $\mu$ decay | | |
| 99 | CC | $\nu_\mu e \rightarrow \mu^- \nu_e$ |

FIGURE 4.1: Channels in NUANCE Event Generator. Figure from [5].

### 4.1.1 Quasi-Elastic Cross Section Model

The cross section models used in NUANCE are specific to the interaction types. The Fermi gas model is used since nucleons are considered in the bound state in a neutrino experiment, where a uniform initial momentum density and a negative binding energy is attributed to the bound state. If a bound nucleon reaches a threshold momentum, it can exit the nucleus. This means that if there are no final state interactions in the nucleus, the minimum possible momentum value of the nucleon exiting the nucleus must be equal to the threshold value. Lepton masses are always accounted for in NUANCE models [5].

For quasi-elastic interactions (charge and neutral current two-body interactions with nucleons), the relativistic Fermi gas model of Smith and Moniz is used by NUANCE [28]. The cross section for both free and bound state nucleons is provided by the model, using identical form factors for both cases. Also, for free nucleon targets, the binding energy is set to zero and the initial momentum distribution is defined as a delta function at zero [5].

For the cross section calculation of charge current quasi-elastic hyperon production, the Smith and Moniz model is extended by Pais [6] to account for the inelasticity of the interaction and the $|\Delta I| = 1/2$ rule.

### 4.1.2 NUANCE for ArgoNeuT

Originally NUANCE was used for carbon and oxygen targets, so modifications had to be made to fit NUANCE to manage argon targets. Additionally, the parameters of the ArgoNeuT detector had to be built into the NUANCE software. These changes gave a target of A = 40 for argon, with 18 protons and 22 neutrons, a nucleon binding energy of 29.5 MeV, Fermi momentum for protons of 242 MeV, and a Fermi momentum for neutrons of 250 MeV. The detector dimensions were set to be a cube of 47.5 cm × 40 cm × 90 cm, corresponding to the x, y, and z dimensions, respectively. The density of the argon was set to 1.396 g/cm$^3$.

### 4.1.3 Event Kinematics

NUANCE produces an output that contains a list of particles, with their particle codes (in accordance with Particle Data Group convention), and tagged as either an initial state particle (denoted -1), final state particle prior to interactions (denoted -2), or the final state particle after interactions (denoted 0). In the detector simulation, only status code 0 particles are used. NUANCE also provides the event kinematics, including the primary vertex (position of the neutrino interaction), the total energy,

and the direction cosines of the particles. Each output also numbers each event with a NUANCE channel number.

## 4.2 Event Simulation with Geant4

### 4.2.1 Particle Propagation

When NUANCE produces the 'final state particles after interactions', these particles are used by the Geant4 software package to simulate the detector and propagate the particles through the detector medium. Geant4 includes simulations of the Time Projection Chamber, inner and outer cryostat, chimney, containment vessel, and the first plane of the MINOS Near Detector. Figure 4.2 shows the Geant4 simulation of major components.

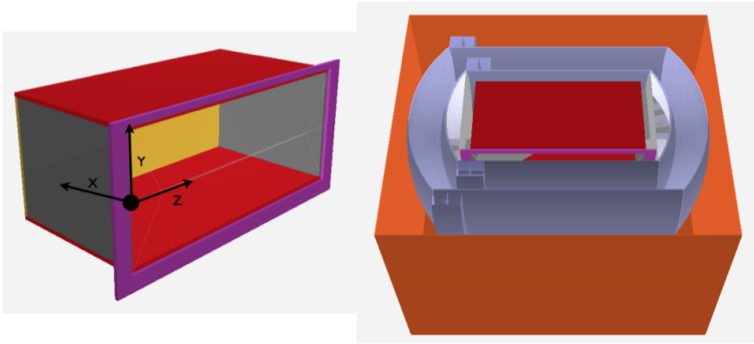


FIGURE 4.2: (Left) Geant4's simulation of the ArgoNeuT Time Projection Chamber, with the cathode shown in yellow and the wire planes in purple. The TPC origin is also shown. (Right) The ArgoNeuT TPC with the inner and outer cryostats as simulated in Geant4. In this orientation, the neutrino beam will enter from the left side. Figures from [12]

As particles propagate, they are subject to the relevant physical processes, up until they reach a kinetic energy of 100 KeV. For ionization electron clouds, three dimensional voxels (pixels in 3D of volume $0.03 \times 0.03 \times 0.03$ cm$^3$ are recorded.

### 4.2.2 Electron Drift and Wire Signal Simulation

After the ionization is recorded in voxels, the ionization is allowed to drift to the wire plane and initiate signals. While the ionization drifts, longitudinal and transverse diffusion constants are used to account for diffusion. The time it takes for the ionization to reach the wire planes determines the amount of diffusion possible. Recombination effects are also simulated, see Equation 2.5 [14, 39]. Additionally, the total number of electrons that reach the wire plane is calculated and assigned to the respective wire. The raw digit ADC counts can be determined by taking the convolution of the induction and collection planes' response shapes. Careful consideration is taken to include simulated electronic noise to complete the electron drift simulations and subsequent wire plane responses.

### 4.2.3 Through-Going Muon Simulation

Due to the size of the ArgoNeuT detector and the characteristics of muons, many muons created upstream of the ArgoNeuT TPC will pass through the detector. Fortunately, the MINOS Near Detector is positioned behind the ArgoNeuT TPC, which keeps a log of muons entering the MINOS Near Detector based on the NuMI trigger. From this log, a normalized set of muons is developed and the reconstructed kinematics of these muons from the MINOS Near Detector are used to simulate them within the ArgoNeuT detector. Using the kinematics from the MINOS Near Detector, simulated muons are created upstream of the forward face of the ArgoNeuT detector and then propagated through the medium with the Geant4 software package.

## 4.3 Event Reconstruction

With each neutrino event inside the detector, a colossal quantity of data is taken. One of the greatest benefits of Liquid Argon Time Projection Chambers is its ability

to provide incredible spatial resolution and detailed calorimetric data. In order to provide precise simulation power, LArSoft must match this data resolutions. LArSoft was created from scratch, maintaining its unbiased "agnostic" approach to simulation, and is constantly being updated. Within LArSoft, reconstructed elements are known as objects, with users having the ability to pick from a list of algorithms in order to reconstruct an object. For the remainder of this chapter, only reconstructed objects and algorithms used in this thesis will be discussed.

### 4.3.1 Raw Data Treatment

As discussed in the previous Chapter, the DAQ electronics digitally records the charge deposited on each wire as a function of time. The next step in treating this raw data is to utilize deconvolution and noise filtering. The remainder of this chapter is adapted from [12].

Recall that the signal on the Induction Plane is bipolar, collecting charge as the ionization electrons approach and as they pass the wire. This creates two separate charge depositions, inverse of each other, on a wire within a short time interval, allowing us to bunch them as a single deposition of charge. The Collection Plane collects the ionization electrons, thus providing a unipolar signal. However, as the wires collect the charge, there is a negative overshoot in the signal which then returns to baseline exponentially. If there is a nearby signal on the same wire that is close in time to this, it can effect the height of that signal. To correct for this a fast Fourier transform (FFT) [40] is used for the raw data deconvolution. This corrects the baseline in the collection plane, identifies the time overlap of the charge depositions in both the planes, and outputs a unipolar induction plane signal.

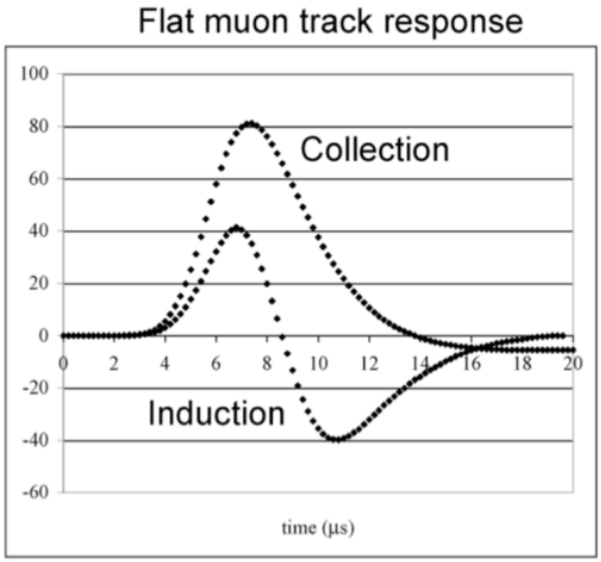


FIGURE 4.3: The base signal for the Induction and Collection planes of the ArgoNeuT detector. This was determined by analyzing a large sample of muons travelling parallel to the wire planes. Figure from [12].

At each wire in ArgoNeut, an empirically-produced signal shape is used, created through thousands of muon tracks considered nearly parallel to the wire planes. To avoid shifting the basic pulse to a wider shape and adding distortion, the delta rays were withheld. By doing this, the effects of electron drift and additional electronic noise can be accounted for. A passable first order approximation of the signal from both planes is given by a FFT that has the most narrow signal still considered as a delta function input to it. The results of this raw data treatment is shown in Figure 4.4, where three consecutive wires are shown prior to and following deconvolution.

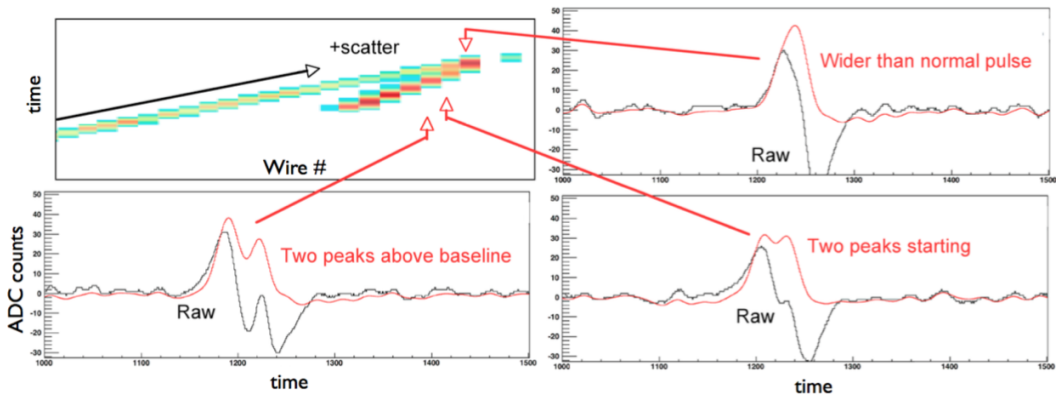


FIGURE 4.4: (upper left) Induction plane of ArgoNeuT showing two deconvoluted tracks. (Upper right, lower left, and lower right) The deconvoluted (red) and raw (black) wire signals with overlapping hits as a function of time from three consecutive wires. Figure from [15].

To account for high frequency noise that is amplified by the FFT, a high frequency filter is used. For the induction plane, an analytic function is used that maintains the low frequency signals, but removed high frequency noise. For the collection plane, a Weiner filter is used [41], which makes an assumed known signal and noise spectra, therefore correcting for the low frequency baseline shift. These filters produce waveforms that are unipolar and smooth.

### 4.3.2 Hit Identification

Following deconvolution, the waveforms produced are then fed to hit finding. In order to properly characterize hits from the waveform special attention must be paid to what region of the waveform constitutes a hit (ADC, time). The hit finding algorithm uses a Guassian-shape approximation to identify the hits of individual wires. The procedure begins by first finding the local minimum within the space of the wire and then searching for a local maximum when increasing in time. If a local maximum is found and is greater than a predetermined threshold, then that area is taken to be a single hit. It then continues in time until it finds the next local minimum and

uses the distance between the two minima as the time width of the hit. This process continues throughout the entire time window for an event.

Using the time widths of the hits, Gaussian fits are utilized to characterize each individual hit. The fit depends on the careful selection of the seed parameters in order to properly converge. These can vary between the induction and collection plane, for example the seed value of time width and parameter uses data to determine a typical hit width. If there are overlapping hits, of n hits, then n Gaussian fits are made to the n consecutive hits in the waveform. Using a linear approximation, the amplitude can be determined with the height of the signal plus any small contribution from neighboring hits. This height can be expressed as,

$$O_i = A_j f(t_j - t_i; w) \tag{4.1}$$

Here $O_i$ is the observed height of the hit and $A_j$ is the true height of the adjacent hits. The function shown, $f(t_j - t_i; w)$, is the model signal that has been normalized with width $w$. Looking at the peak times of the adjacent hits of each model signal, this function determines the influence of nearby hits on the amplitude of the considered hit. Note that we can consider Equation 4.1 to take the form $\vec{O} = M\vec{A}$, where $M$ is a matrix of the function values at each point. This creates hits with unique start times, end times, widths, and signal amplitudes.

### 4.3.3 Density-Based Clustering

After the hits are reconstructions, the next step in processing their information is to clump them together based on their position and density. This creates an object known as a cluster. The formation of clusters is accomplished by using a procedure known as 'density-based spatial clustering of applications with noise' (DBSCAN) [18]. For each wire plane, DBSCAN creates clusters separately. A hit $q$ is considered 'directly density-reachable' from another hit $p$ if it is within a given region $\epsilon$ and if $p$

has a sufficiently higher density of hits near it. This and the following definitions are shown in Figure 4.5. The region $\epsilon$ is modified to account for the slight variation in resolution in wire and time directions. Next, a hit $q$ is 'density-reachable' from another hit $p$ if there exists a series of consecutive hits $p_i(p_1,...,p_n$, such that $p_1 = p$ and $p_n = q$, and each $p_i + 1$ is directly density-reachable from $p_i$. Note that there exists the possibility that one hit can be directly density-reachable from another hit, but not vice versa. If one hit is not surrounded by a sufficient number of hits, but the other hit is. This asymmetry brings forth another special definition; if there exists a separate hit $k$ such that the two hits $q$ and $p$ are both directly density-reachable from k, then $q$ and $p$ are density-connected.

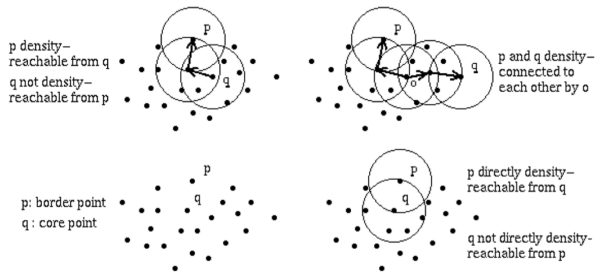


FIGURE 4.5: The definitions given in DBSCAN. Figure adapted from [18].

The DBSCAN algorithm takes an arbitrary point $p$ and finds all the hits that are density-reachable from it. Every hit that exists in this cluster are known as core hits, while the hits on the periphery are known as border hits. Once the cluster has been determined, the algorithm will then move onto hits that have not yet been assigned an association with any cluster. This process propagates until all hits have been considered. Figure 4.6 shows this process and output.

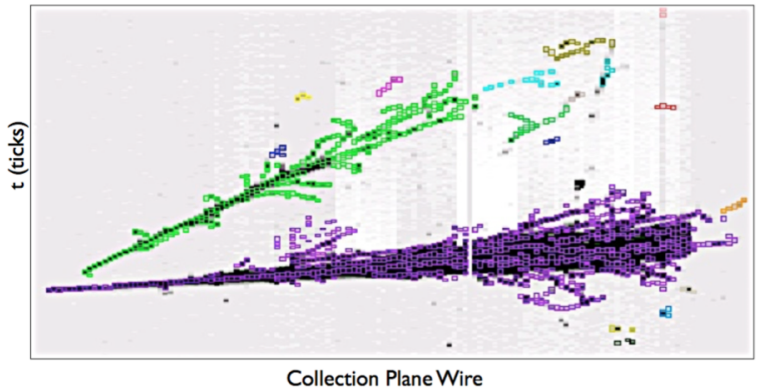


FIGURE 4.6: A visual product of the DBSCAN algorithm ran on a neutrino event. The raw data is shown in grey, with unique clusters given distinct colors. Figure from [15].

### 4.3.4 Two Dimensional Line Reconstruction

It is expected that the trajectory of most particles in ArgoNeut will follow line-like paths, since ArgoNeuT is not magnetized. One might entertain the idea that lines can be found with relative ease by a simple linear regression of the density-based clusters. But alas, the world does not give us the easiest path, and this approach would not account for events that consist of more than one track or clusters that have excessive noise. Even density-based clusters that one consist of a single track are a significant amount of trouble because of many things such as delta ray production, Coulomb scattering, noisy or dead wires, or non-uniformities in the electric field, etc. In order to circumvent these challenges, line-like cluster finding is accomplished through the use of the Hough transform [42].

The Hough Transform takes the locations and weights of all the points in an image and creates a parameter space, known as 'Hough accumulator'. The algorithm defines a line as $r = x\cos\theta + y\sin\theta$ for each $(x, y)$ in an image. The line will define a distinct sinusoidal wave for each $(x, y)$ in the $(r, \theta)$ plane. If the curves for two $(x, y)$ points overlay each other, then the point of intersection in the $(r, \theta)$ plane will define

the line that passes through both of the two points in $(x, y)$. Figure 4.7 shows this graphically.

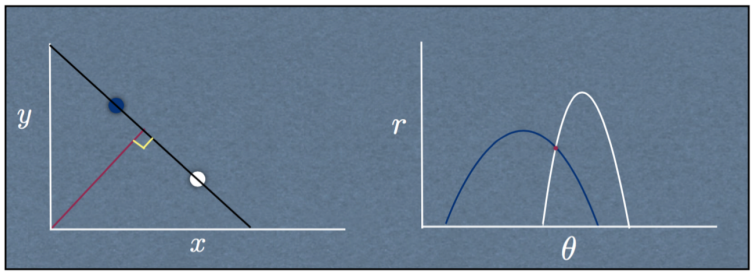


FIGURE 4.7: (Left) Two points in the $(x, y)$ plane. (Right) Both points parametrized in the $(r, \theta)$ plane. The intersection point is shown in red and defines a line that passes through both of the two points in $(x, y)$. Figure from [12]

Each $(x, y)$ point is translated into the accumulator $(r, \theta)$ space and the cells that have a weight above a threshold will be considered as line candidates. The cell with the highest weight, which would correspond with the highest number of crossing curves, is used as the center of a candidate line formed by using the center-of-mass of a $3 \times 3$ cell window. This procedure is repeated, each time considering hits that have not yet been associated with a candidate line. This is done until a threshold value is reached or the maximum number of lines is reached. It is possible with Hough transforms to partition a single line-like cluster into many, since each segment with have slight variations in slope and intercepts which gives more cells to choose from the Hough accumulator.

### 4.3.5 Line Merging

The Hough Transform, as discussed in the previous section, is able to partition a single line-like cluster into more than one cluster. In order to make three-dimensional tracks out of these two-dimensional line-like clusters, it is crucial to combine clusters together if they have similar slopes and endpoints. In LArSoft, an algorithm is used to combine the like clusters and form a 'merged-line'. This is shown in Figure 4.8.

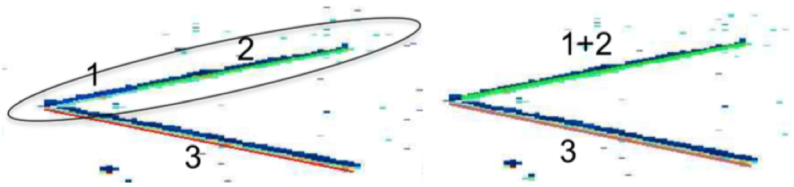


FIGURE 4.8: (Left) Three Hough line clusters, showing #1 in blue, #2 in green, and #3 in red. (Right) The merged-lines following the merging algorithm. Figure from [12]

### 4.3.6 Three Dimensional Tracking

Once all clusters have been merged, the reconstruction of the three dimensional tracks can occur. First, the drift distance between the two planes must be accounted for, which then allows the clusters to be matched by their start and end point time coordinates in each plane. Once two clusters have been matched together, the three dimensional track is reconstructed along with the direction cosines. The direction of the 3D track is reconstructed first, after which hit-by-hit matching is done to produce 3D space points $(x, y, z)$ which allows the creation of a high resolution 3D image for each event. The calculation of a space point is given as,

$$\begin{aligned} x &= t v_d \\ y &= \frac{v-u}{2cos\alpha} \\ z &= \frac{v+u}{2sin\alpha} - \frac{Y}{2tan\alpha} \end{aligned} \tag{4.2}$$

where $u$ and $v$ are the wire coordinates (cm) for the induction and collection planes respectively. $v_d$ is the drift velocity of the ionization charge in the TPC, $Y$ is the height of the TPC, and $\alpha$ is the absolute value of the angle of the wires, with respect to the vertical axis.

### 4.3.7 Matching with MINOS Near Detector

One of the unique challenges of the ArgoNeuT collaboration is the small detector size. Since most of the muons created will exit the detector, utilizing the MINOS Near Detector that sits directly behind the ArgoNeuT TPC allows for the reconstruction of these tracks. Using the MINOS offline analysis code [12], the tracks can be reconstructed across both detectors. If the muon track stops within the MINOS fiducial volume, the total energy deposited in the detector can be used to reconstruct the momentum of the muon. For muons that do not stop in the detector, the magnetization of the MINOS Near Detector allows for the momentum to be determined by its curvature when traveling through the detector, along with the charge. This track can then be matched if the $Z$ vertex of the track is within 20 cm of the center of the first plane of the MINOS Near Detector. Using the common time stamp from the accelerator division, the tracks in ArgoNeuT and MINOS can be selected on a spill-by-spill basis. If a track stops within the instrumented region of the MINOS detector, that is considered a stopped track. This, as well as some other reconstruction variables, differ from the MINOS reconstruction protocol. Figures 4.9 and 4.10 show this difference.

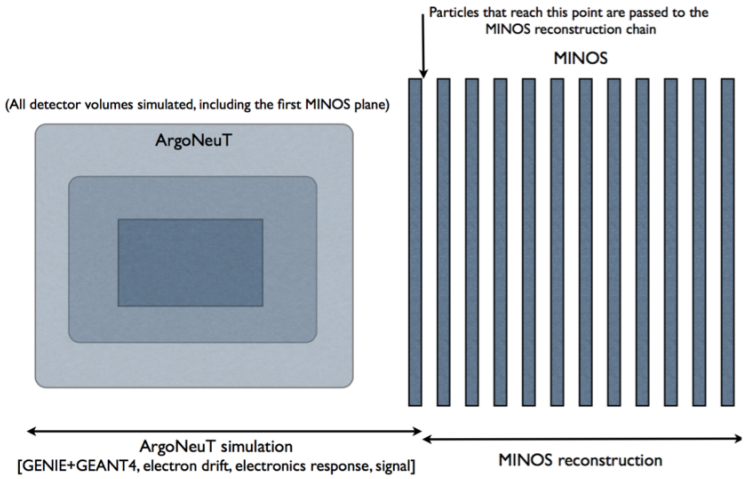


FIGURE 4.9: The ArgoNeuT simulation corresponding to the TPC, inner cryostat and outer cryostat. (This figure is not to scale). Figure from [12].

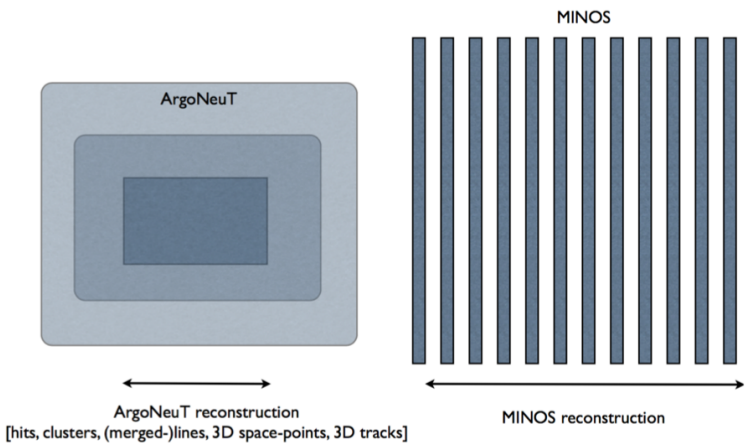


FIGURE 4.10: The ArgoNeuT reconstruction shown when applied to simulation and data. (This figure is not to scale). Figure from [12].

### 4.3.8 Vertex Finding

Once the lines have been merged (which will be denoted as clusters moving forward), the two-dimensional vertices can be calculated. The algorithm used determines multiple vertices in each plane and then matches them across the planes to determine the three-dimensional vertices.

First, the algorithm sorts all the clusters by descending length, in each plane. It will then verify if there is a matched track in MINOS and if not, it will use the start point of the longest cluster in each plane as a vertex candidate. From this, a straight line fit is performed on the beginning section of each cluster, since most tracks produced in ArgoNeuT are straight in the beginning. This line fitting is iterated three times and each iteration, hits that have high incremental $\chi^2$ values with respect to the straight line fit, are removed. This allows us to negate delta ray hits and other hits from noise. The wire coordinate numbers for each hit are converted to time ticks. While the error in hit times are incorporated, the error in wire number is assumed to be zero. If the cluster has more hits than a minimum threshold number, then the cluster is 'accepted' for vertexing.

For the first accepted cluster, the two-dimensional start point is considered to be a 'guessed vertex' and calculations are made of the distance of closest approach as defined between a cluster and the guessed vertex. If a cluster has a distance of closest approach greater than a given threshold, it is removed from vertex finding. A vertex $\chi^2$ is defined as the squared sum of the distance of closest approach of clusters weighted by their error. By minimizing the $\chi^2$, the best fit coordinates of a two-dimensional vertex is found. This is shown in Figure 4.11.

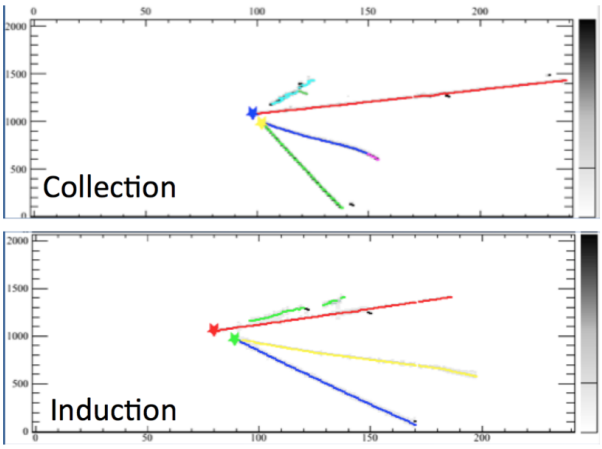


FIGURE 4.11: A simulated event that displays the reconstructed vertices of an event. The colored lines and stars each show different clusters and vertices, respectively. There are two reconstructed vertices in each plane. Figure from [1].

For the technical description, Figure 4.12 gives a visual representation.

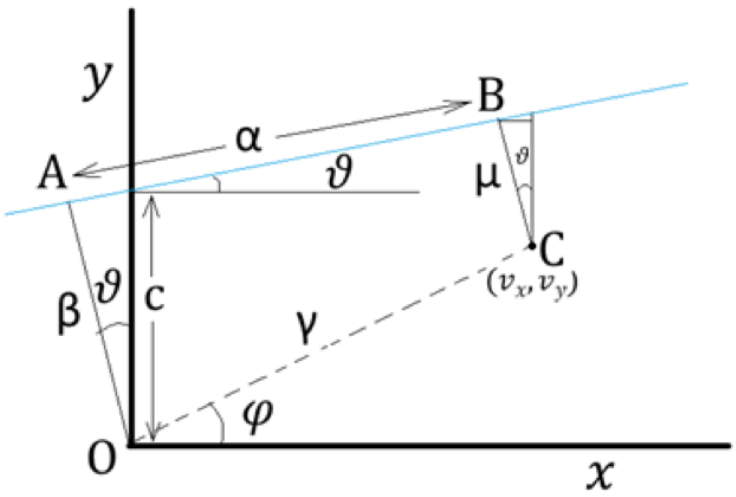


FIGURE 4.12: Straight line cluster (blue line) in a wire plane. The X-axis gives the wire numbers converted to ticks and the Y-axis is the time tick. Point C is the guessed vertex and $\mu$ is the distance of closest approach from the guessed vertex to the straight line cluster. Figure from [1].

Let's first assume a straight line cluster (given as a blue line in Figure 4.12) in one of the wire planes and designate the x-axis to be ticks and the y-axis to be the time tick. The cluster makes an angle $\theta$ with the horizontal with an intercept 'c'. If we have a guessed vertex at point 'C' with coordinates $(v_x, v_y)$, then the distance of closest approach ($\mu$) is given by:

$$\mu = c\cos\theta - v_y\cos\theta - v_x\sin\theta \tag{4.3}$$

We can write $\theta = \tan^{-1} m$, where $m$ is the slope of the straight line cluster. This allows us to rewrite Equation 4.3 as,

$$\mu = c\cos(\tan^{-1} m) - v_y\cos(\tan^{-1} m) - v_x\sin(\tan^{-1} m) \tag{4.4}$$

The uncertainty in the distance of closest approach $\sigma_\mu$ is expressed as,

$$\sigma_\mu = \sqrt{(\cos\theta)^2\sigma_c^2 + \left(\frac{1}{1+m^2}\left[-c\sin\theta + v_y\sin\theta + v_x\cos\theta\right]\right)^2\sigma_m^2} \tag{4.5}$$

where $\theta_c$ and $\theta_m$ are the errors on the intercept $c$ and slope $m$, respectively, of the straight line fit of a cluster. These are calculated simultaneously while the lines are fitted.

We can use these expressions to express the vertex $\chi^2$ of a cluster $i$,

$$\chi^2_i = \frac{\mu_i^2}{\sigma^2_{\mu_i}} = \frac{(c_i \cos\theta_i - v_y \cos\theta_i - v_x \sin\theta_i)^2}{(\cos\theta_i)^2 \sigma^2_{c_i} + \left(\frac{1}{1+m_i^2}\left[-c\sin\theta_i + v_y \sin\theta_i + v_x \cos\theta_i\right]\right)^2 \sigma^2_{m_i}} \tag{4.6}$$

The total vertex $\chi^2$ if n clusters are added to the vertex can be given by,

$$\chi^2 = \sum_{i=1}^{n} \left( \frac{(c_i \cos\theta_i - v_y \cos\theta_i - v_x \sin\theta_i)^2}{(\cos\theta_i)^2 \sigma^2_{c_i} + \left(\frac{1}{1+m_i^2}\left[-c\sin\theta_i + v_y \sin\theta_i + v_x \cos\theta_i\right]\right)^2 \sigma^2_{m_i}} \right. \tag{4.7}$$

The best fit values $(v_x, v_y)$ for the vertex are given by minimizing Equation 4.7. Once the vertices are identified, they are matched between the wire planes to create three-dimensional vertices.

### 4.3.9 Calorimetric Reconstruction

Once the vertices and tracks have been reconstructed in three dimensions, the calorimetric information can be used to identify the corresponding particles. This method of particle identification has been discussed in detail in Section 2.3.2.

The calorimetry algorithm utilizes the three-dimensional tracks to calculate the track pitch, which is a measure of the track length as seen by a single wire. Then all the corresponding hits to that track are used to calculate the amount of deposited charge per unit track pitch. There are two effects that can reduce the amount of charge on a wire: recombination, the recombining of ionization electrons with argon ions before they can be separated by the applied electric field, and absorption, the charge lost due to electronegative impurities in the fiducial volume of the detector. Charge quenching is often used interchangeably with the recombination effect. When these effects are

corrected for, the true total charge deposited by a track per unit track pitch can be determined. The amount of energy deposited by a track per unit length (dE/dx) is calculated with Birk's Law [14, 39], which can then be summed over the full track to get the total amount of kinetic energy.

Knowing the charge deposition and the charge loss per unit track length allows us to identify the particles. For a track that stops inside the detector, the total energy deposited by the track and the range of the track can produce compelling information about what particle the track is associated with. Additionally, the energy loss profile provides more information for particle identification. The curves of different particles from Geant4 simulations are shown in Figure 4.13.

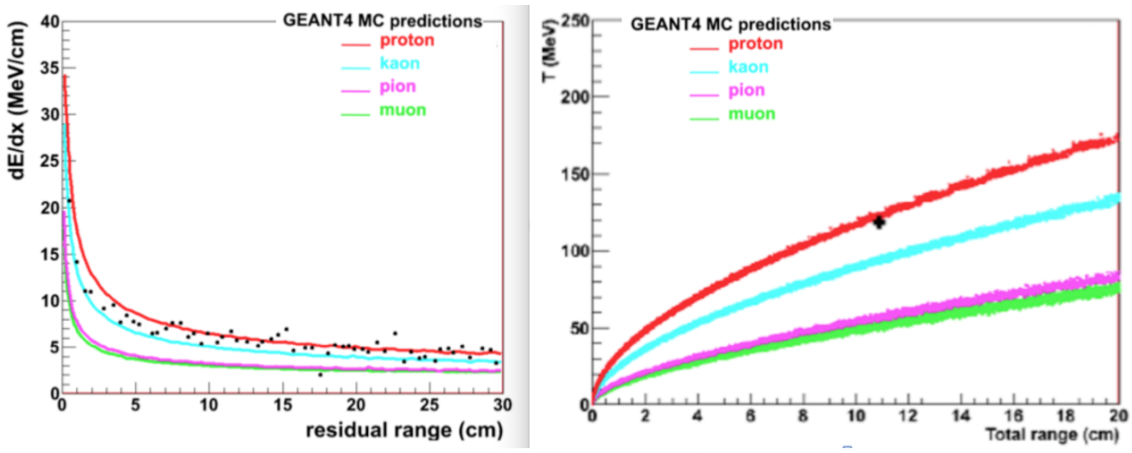


FIGURE 4.13: (Left) Simulated energy loss per unit track length as a function of residual range for different stopping particles. The plot is overlaid with points of a track reconstructed by the calorimetry module for reference. (Right) Simulated kinetic energy as a function of range of different particles. Figure from [15].

# CHAPTER 5

# Analysis

## 5.1 Introduction

This chapter documents the process to measure the charge current quasi-elastic (CCQE) neutral hyperon production cross section in a Liquid Argon Time Projection Chamber. The topological study described in the beginning of this chapter can be found in full detail in [1]. CCQE Neutral Hyperons are created through interactions with antineutrinos. When an muon antineutrino interacts with a proton, the proton is converted to a hyperon. This is shown as,

$$\begin{aligned} \bar{\nu}_\mu + p &\longrightarrow \mu^+ + \Lambda^0 \\ \bar{\nu}_\mu + p &\longrightarrow \mu^+ + \Sigma^0 \end{aligned} \tag{5.1}$$

This rarely studied process is a Cabibbo-suppressed process. The $\Lambda^0$ is a weakly decaying strange particle with a relatively long decay time. When it does decay, it produces either two charged particles $p\pi^-$ or two neutral particles $n\pi^0$. The $\Sigma^0$ electromagnetically decays to a photon and $\Lambda^0$, which will then decay as detailed above. This analysis is based on the combination of the topological and calorimetric properties of the $\Lambda^0$ decay. Using the high resolution images that a LArTPC can produce from neutrino interactions, the characteristic topology of $\Lambda^0$ can be identified as a primary vertex with one track and then a detached secondary vertex with two tracks branching from it. The charged daughter particles produced in the CCQE hyperon decay processes are what make up the 'signal' for this analysis.

The NUANCE neutrino event generator **??** was modified to use argon targets with the ArgoNeuT detector and was interfaced with the LArTPC software, LArSoft. By doing

this, it allows for the full detector to be simulated, as well as the ability to match exiting muons from ArgoNeuT into the MINOS Near Detector. This chapter will outline the analysis steps taken ([1]), the progression of the analysis, and the further actions required to complete the full study.

The cross section section measurement for the processes given in Equation 5.1 can be expressed as,

$$\sigma_{(CCQE_{\Lambda^0+\Sigma^0})} = \frac{f \times \left(N_{\text{data}} - N_{\text{bkg}}\right)}{\phi \times N_{\text{targ}} \times \epsilon} \tag{5.2}$$

Here $N_{\text{data}}$ is the number of data events that pass all analysis cuts, $N_{\text{bkg}}$ is the predicted number of background events, $\phi$ is the total antineutrino flux, $N_{\text{targ}}$ is the number of targets (protons) in the fiducial volume of the detector, $\epsilon$ is the efficiency of all analysis cuts, and $f$ is the correction for the branching fraction of hyperon decay to neutral particles.

## 5.2 Flux

Figure 5.1 shows the flux in the low energy configuration of the antineutrino NuMI beam.

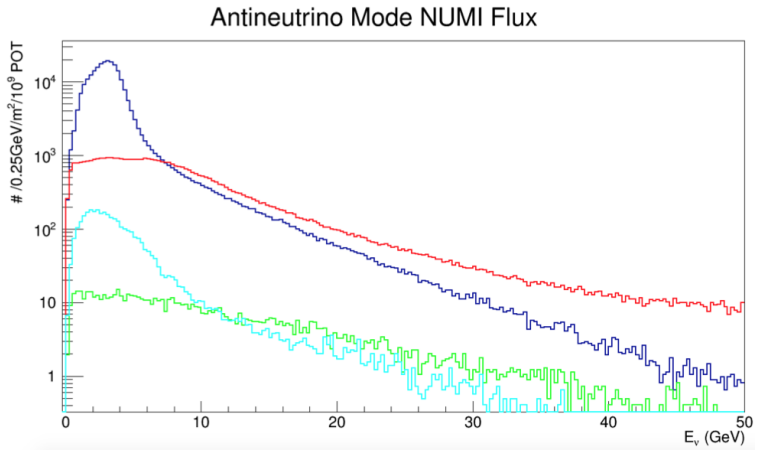


FIGURE 5.1: Antineutrino flux of $\nu_\mu$ (red), $\bar{\nu}_\mu$ (blue), $\nu_e$ (green), and $\bar{\nu}_\mu$ (cyan) in the Low Energy (LE) antineutrino mode NuMI beam. Figure from [1].

This analysis uses a total integrated flux of $2.4 \times 10^5 \bar{\nu}_\mu / m^2 / 10^9$POT for the antineutrino beam. In ArgoNeuT's antineutrino-mode run, it received $1.25 \times 10^{20}$ POT. However, since this analysis requires the MINOS Near Detector track information for muons, a correction must be made to give the amount of POT while both detectors were active, giving $1.20 \times 10^{20}$ POT used in this analysis.

## 5.3 Analysis Steps

The analysis consists of two major studies, a topological study and a calorimetric study. The topological study was conducted by Dr. Farooq and can be found in detail in [1]. The study utilizes only the topology of the neutrino interaction to determine the signal events. The calorimetric study builds upon the topological study and uses the charge deposited per unit track length to determine the identity of the particles, which can be used to further determine signal events. The next two sections will discuss the process used in the topological study, present the results of that study, and discuss the progress made on the calorimetric study. This study uses roughly five months of ArgoNeuT data when the NuMI beam was in antineutrino-mode. The antineutrinos created in antineutrino-mode are of a lower energy than the neutrinos. This is shown visually in Figure 5.2.

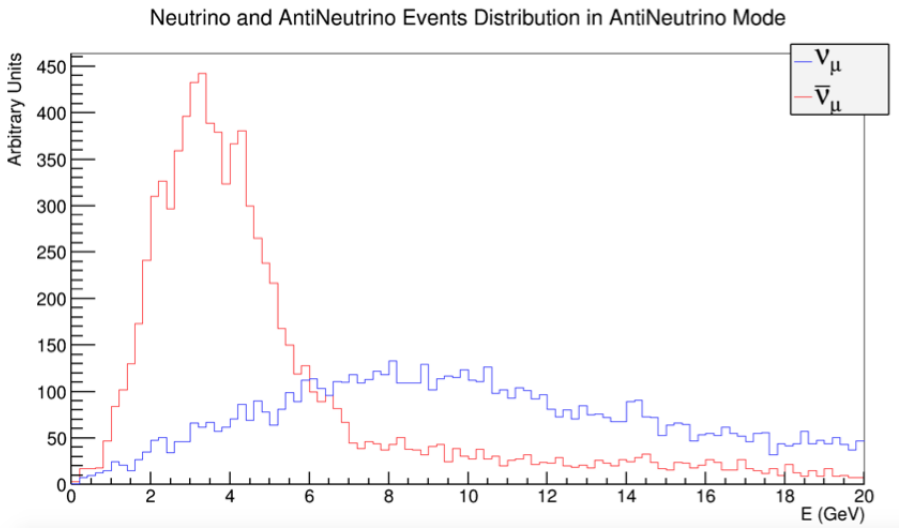


FIGURE 5.2: The energy spectrum of neutrino and antineutrino events in an MC sample of a antineutrino-mode run of ArgoNeuT. Figure from [1].

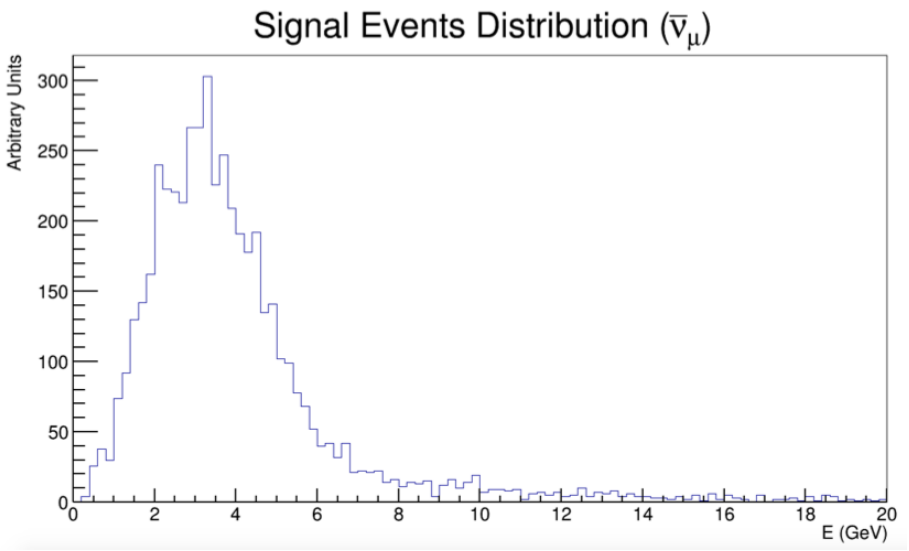


FIGURE 5.3: The energy spectrum of the signal events in an MC sample of a antineutrino-mode run in ArgoNeuT. Figure from [1].

## 5.4 Topological Study

The topological study consists of two major analysis steps, the automatic reconstruction and visual scanning.

### 5.4.1 Automatic Reconstruction

The first analysis step taken is to reconstruct the events and filter based on automatic reconstruction cuts. Using the NUANCE event generator, events are simulated in the detector and passed through the full reconstruction chain of ArgoNeuT. If a muon track exits the ArgoNeuT detector into the MINOS Near Detector, the tracks are matched and calculations are made to determine the momentum and charge sign. The purpose of the automatic reconstruction step is to retain as many signal events as possible, while also rejecting as many background events as possible. The difficulty lies in the fact that $\Lambda^0$ produces a significantly weak signal. The reconstruction cuts set 4 conditions that must be met:

1. The primary vertex is reconstructed inside the fiducial volume of TPC, defined as $[3 < x < 44, -16 < y < 16, 6 < z < 86]$, with all dimensions in cm.
2. More than 1 Linemerger clusters are reconstructed in each wire view.
3. Track matching with MINOS Near Detector (with +ve charge and non-zero momentum reconstructed by the MINOS Near Detector) ($\bar{\nu}_\mu$).
4. The MINOS Near Detector matched track starts inside the fiducial volume of the TPC.

At the edges of the TPC the electric field becomes non-uniform and the possibility arises for through-going muons not created by a neutrino interaction inside the detector, which is rejected by requiring the primary vertex to be within the fiducial volume. By requiring that there must be more than one Linemerger cluster in each wire view, some $\bar{\nu}_\mu$ CCQE events that have $\Lambda^0$ decaying into neutral particles will be rejected since they will often only have a $\mu^+$ track. Neutral current (NC) and $\nu_\mu$ are rejected by requiring MINOS Near Detector matching with positive charge. Figure 5.4 shows the difference between the true and reconstructed vertices for all MC events that passed the automatic cuts. Each graph is fit with a Gaussian to show the vertex

resolution. Note the tails in the Y and Z graphs, corresponding to mis-reconstructed space points during the plane view matching process. There is a minor shift in the X graph also, because there is 10 $\mu$s start time window of the NuMI beam. It is important to note that the resolution of each of the graphs is in the sub-cm level.

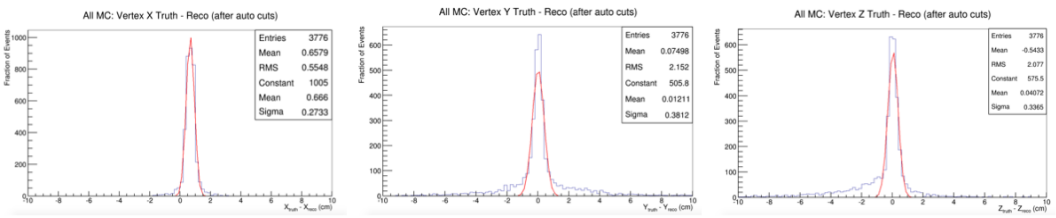


FIGURE 5.4: These graphs show the difference between the true and reconstructed vertex (X on the left, Y in the center, and Z on the right) of all the events that pass automatic cuts. Figure from [1].

Figures 5.5 and Figure 5.6 shows the X vs Z vertex distribution (top view of the detector) and the X vs Y vertex distribution (downstream face view of the detector), respectively. Figure 5.7, Figure 5.8, and Figure 5.9 gives the X, Y, and Z vertex distributions of the data for all the MC events passing the automatic cuts. The cut of the fiducial volume from 6 cm (upstream) in the Z direction will assist in rejecting through-going muons. This is not complete, however, and through-going muons will still exist in the data, as shown in Figure 5.9. In MC, through-going muons are not simulated, and in the data they are removed in visual scanning.

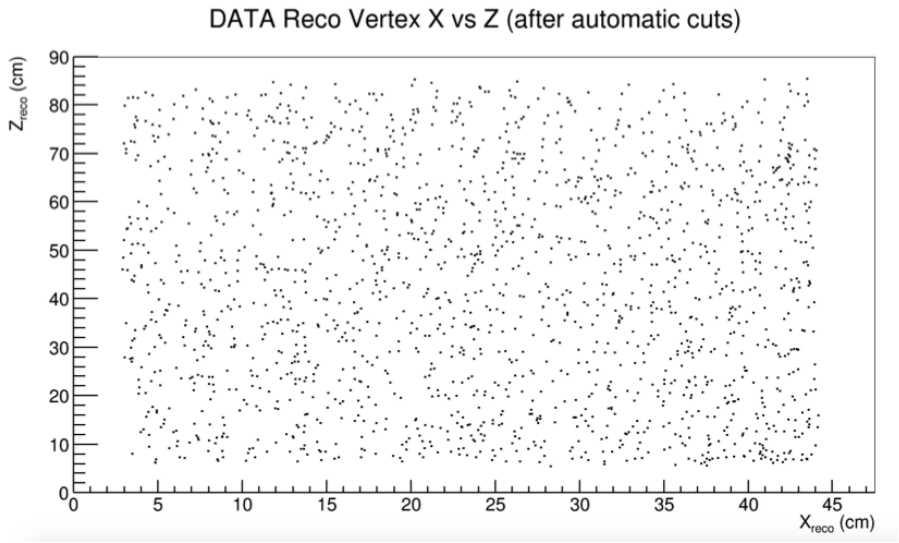


FIGURE 5.5: X vs Z vertex distribution of all data events that pass the automatic cuts. Figure from [1].

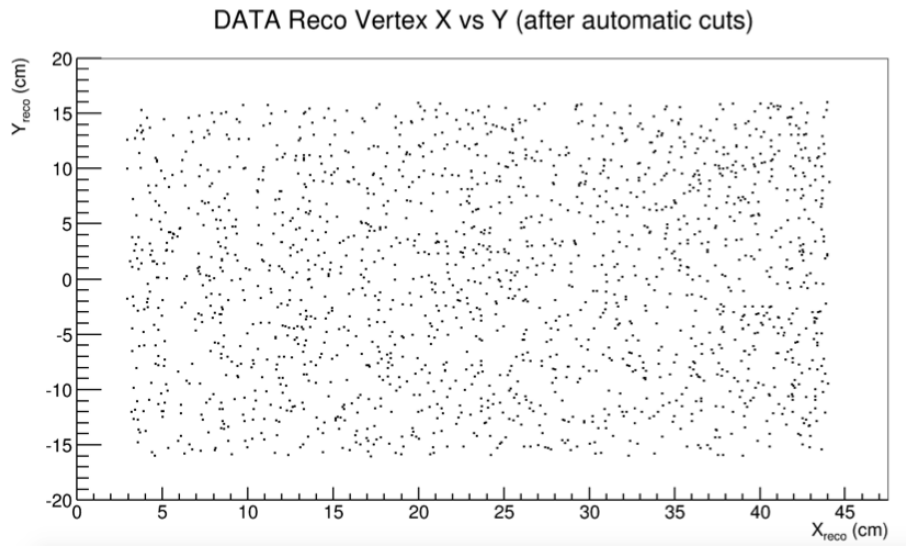


FIGURE 5.6: X vs Z vertex distribution of all data events that pass the automatic cuts. Figure from [1].

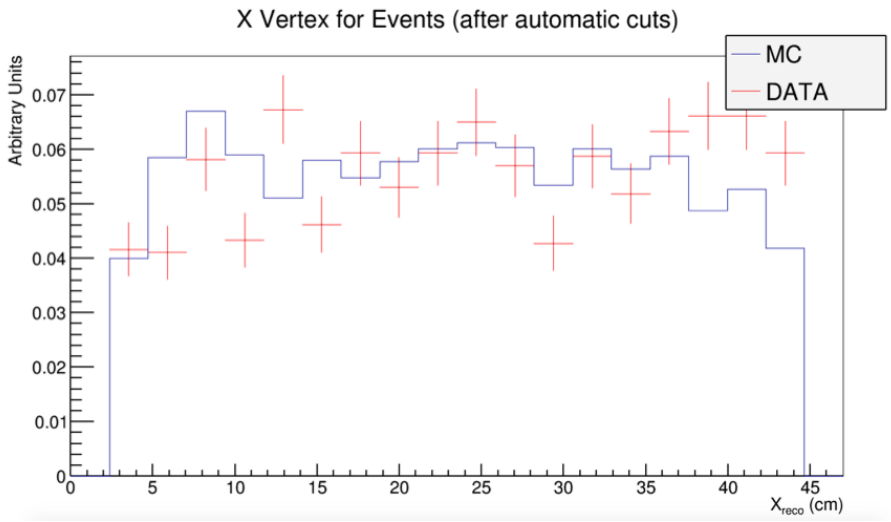


FIGURE 5.7: X vertex distribution for reconstructed data and MC that pass automatic cuts. Both are normalized to one. Figure from [1].

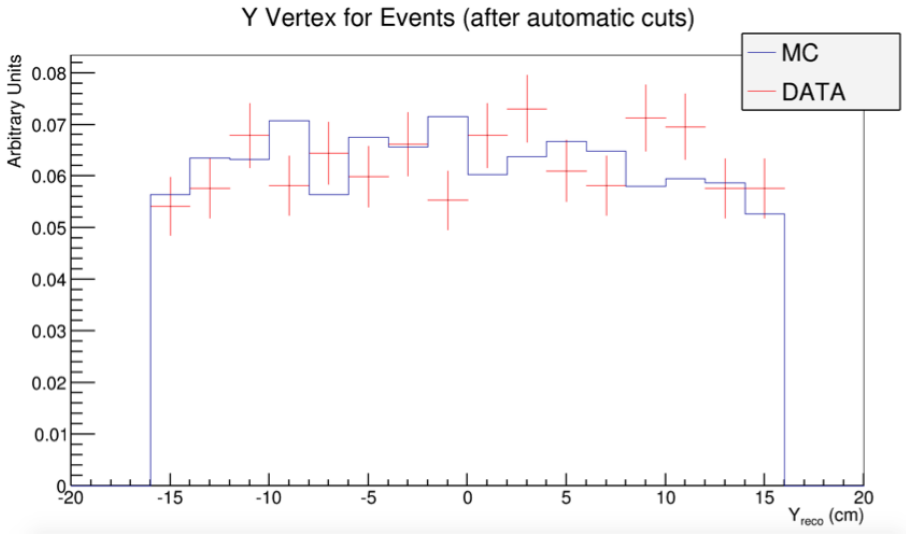


FIGURE 5.8: Y vertex distribution for reconstructed data and MC that pass automatic cuts. Both are normalized to one. Figure from [1].

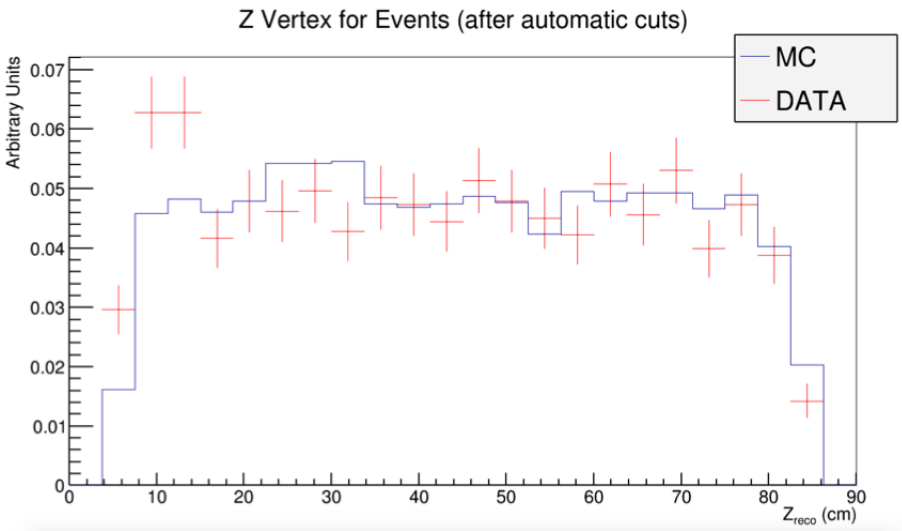


FIGURE 5.9: Z vertex distribution for reconstructed data and MC that pass automatic cuts. Both are normalized to one. Figure from [1].

Matching a track with the MINOS Near Detector allows the rejection of Neutral Current (NC) background events and the charge reconstruction assists in determining antineutrino events. MC is used to select the cuts made for ArgoNeuT tracks that exit the TPC and project into the MINOS Near Detector. A requirement is set that the difference in the angle between the projected ArgoNeuT track and the MINOS Near Detector should not be greater than 0.4 rad, as well as the radial distance between them being no more than 27 cm. The relative sizes and position of the ArgoNeuT and MINOS Near Detector are shown in Figure 5.10. The ArgoNeuT display showing the tracks of one spill, including a negatively charged track from ArgoNeuT to MINOS, is shown in Figure 5.11.

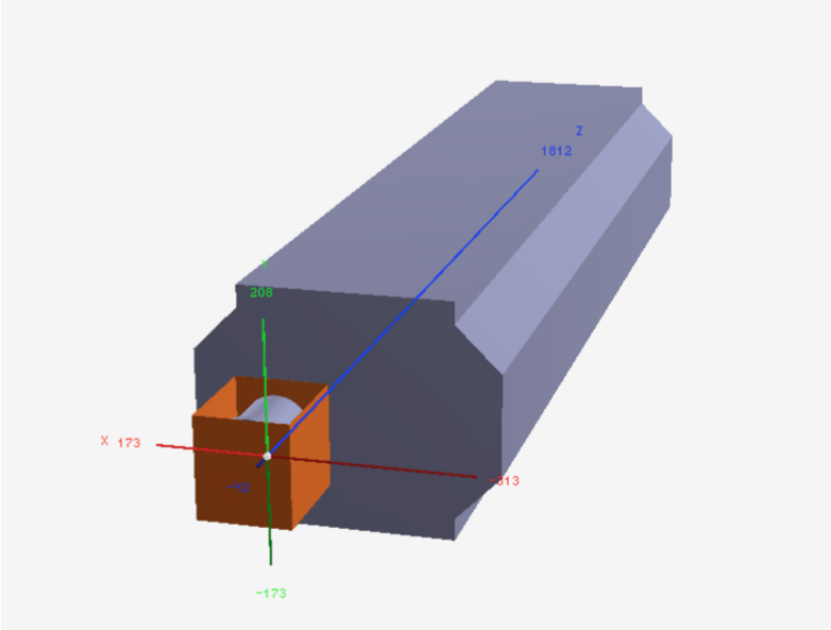


FIGURE 5.10: The relative size and position of ArgoNeuT (orange) and MINOS Near Detector (purple) in the MINOS Near Detector hall at Fermilab. Figure from [10].

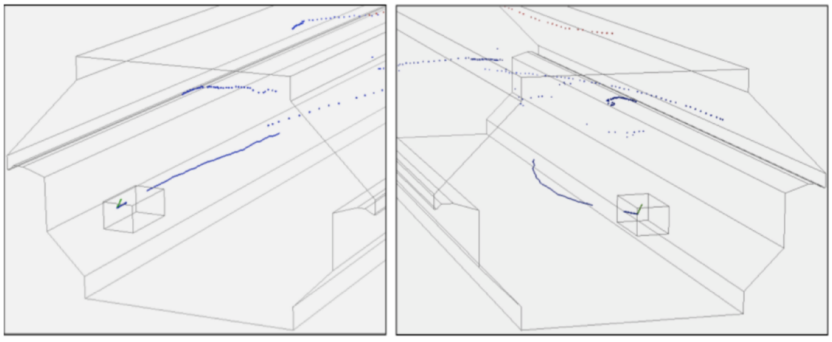

FIGURE 5.11: Tracks in both ArgoNeuT and MINOS Near Detector, with a negatively charged track matched between ArgoNeuT and MINOS. All tracks in the spill are visible. Figure from [15].

If there is more than one ArgoNeuT track matched, the least value of $\Delta r/\cos\theta$ will be considered the best match; where $\Delta r$ is the radial distance of the projected track in ArgoNeuT to the MINOS track, and $\theta$ is the angle between those two tracks. Following the matching of the tracks, the momentum and charge can be determined. The reconstructed muon momentum for data and MC events in ArgoNeuT is shown in Figure 5.12. The total momentum of the muon is determined by summing the

energy deposited in the ArgoNeuT TPC, the energy lost between the ArgoNeuT TPC and MINOS Near Detector, and the energy deposited in the MINOS Near Detector. The momentum of the muon is corrected for in ArgoNeuT by looking at the energy deposited as it travels through the TPC, the energy lost between the detectors by using a Geant4-based study, and the MINOS Near Detector measures the momentum as it travels through the detector. Figure 5.13 gives the muon's energy lost as a function of distance traveled between ArgoNeuT and the MINOS Near Detector. This gives a non-linear function, but this can be accounted for when considering the non-homogeneous composition of the two detectors. The energy lost calculations are still calculated by using a linear fit. Figure 5.14 gives the muon angles for all data and MC events that pass the automatic cuts. There is a difference in the neutrino beam angle in data and MC of $-3.3°$ which gives the difference in the distribution between them. The NuMI beam is pointed at $-3.3°$ so that the neutrino beam is in line with the MINOS Far Detector in Soudan, Minnesota, while the MC beam is pointed at $0°$. The effect of this difference from MC to data was determined by assigning weights to the MC events in muon angle bins and a systematic error is used in the calculation of the final measurement.

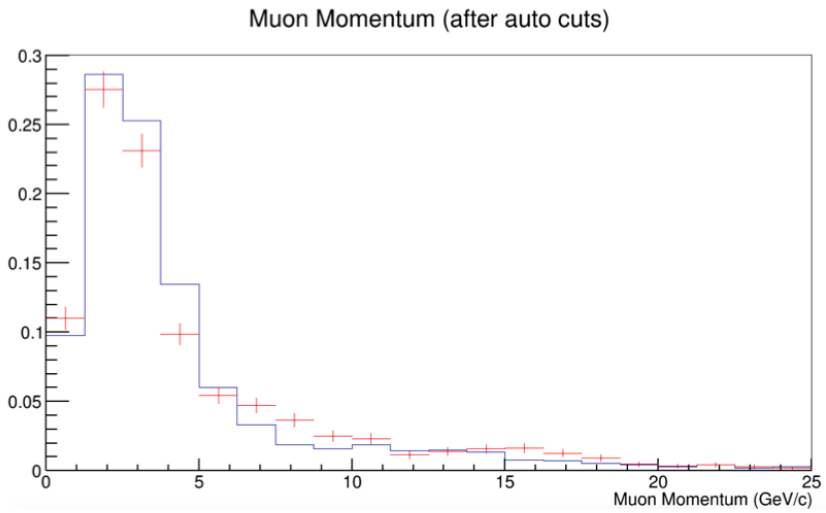


FIGURE 5.12: The distribution of muon momentums for all data (red) and MC (blue) events that pass the automatic cuts, normalized to one. Figure from [1].

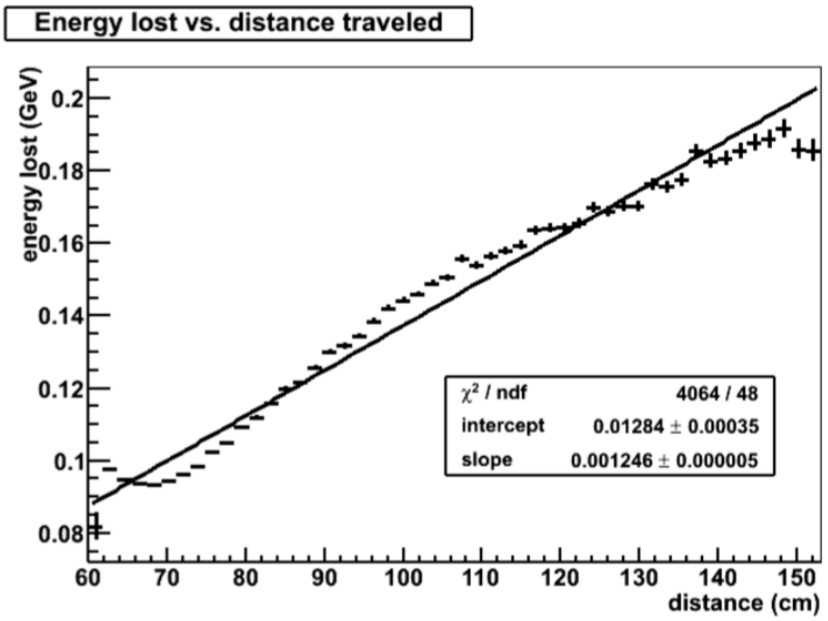


FIGURE 5.13: The energy lost of a muon as a function of distance traveled between the ArgoNeuT TPC and the MINOS Near Detector, predicted from Geant4. The non-homogeneous composition of the two detectors gives the non-linear functionality. Figure from [10].

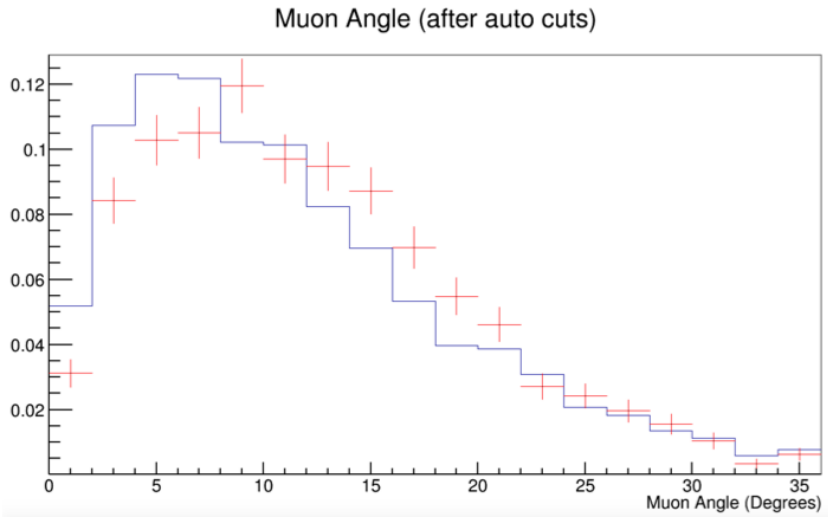


FIGURE 5.14: The distribution of muon angles for all data (red) and MC (blue) events that pass the automatic cuts, normalized to one. Figure from [1].

The automatic cuts gave a 78.7% signal acceptances ($\epsilon_{\text{cuts}}$ and an 81.3% background rejection. Recall that a 'signal' is an event the produces a neutral hyperon decaying into a proton and a pion. There is a branching fraction of 63% of a $\Lambda^0$ or $\Sigma^0$ decaying

to charged particles. A total data sample of 1753 events pass through the automatic cuts. These results are given in Table 5.1.

| **Cuts** | **Description** | **Signal Acceptance** | **Background Rejection** | **Data** |
|---|---|---|---|---|
| Automatic Reconstruction Cuts | FV, MM $\mu^+$, MM track begins in FV, Clusters in each view > 1 | 78.7% | 81.3% | 1753 |
| Scanning Cuts | Primary tracks = 1,2<br>Secondary tracks = 2<br>Detached vertex = 1,2<br>Reject events with 2 showers | 75.7% | 98.6% | 36 |

TABLE 5.1: Signal acceptance and background rejection rates along with the number of data events after each cut. Table from [1].

The number distribution of reconstructed tracks in data and MC following the automatic cuts is shown in Figure 5.15. The distribution of the number of Linemerger clusters in the Induction and Collection wire planes for data and MC after the automatic cuts are given in Figure 5.16 and Figure 5.17, respectively. The distribution of exiting tracks in data and MC after automatic cuts is given in Figure 5.18. In all plots, the data and MC are in agreement and normalized to one.

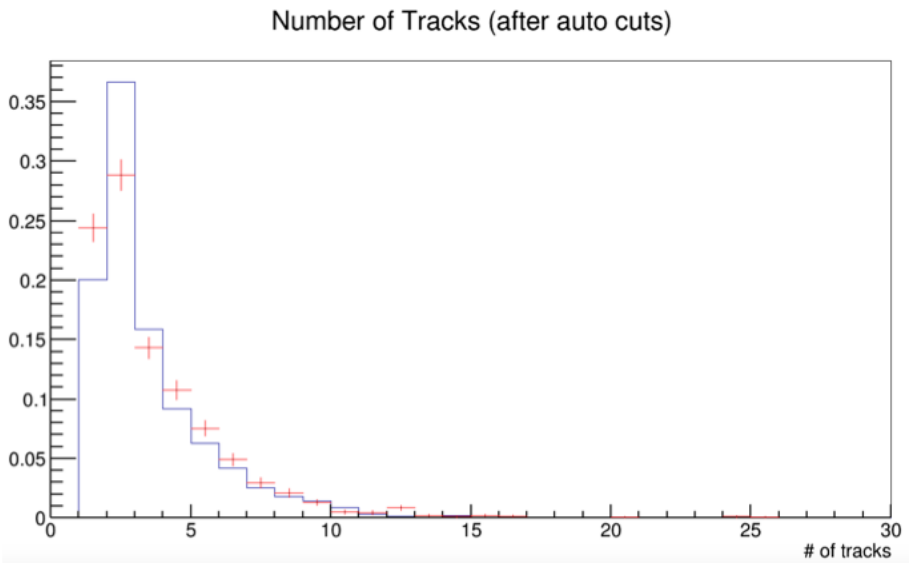


FIGURE 5.15: The number of tracks reconstructed in the data (red) and MC (blue) after the automatic cuts. Both have been normalized to one. Figure from [1].

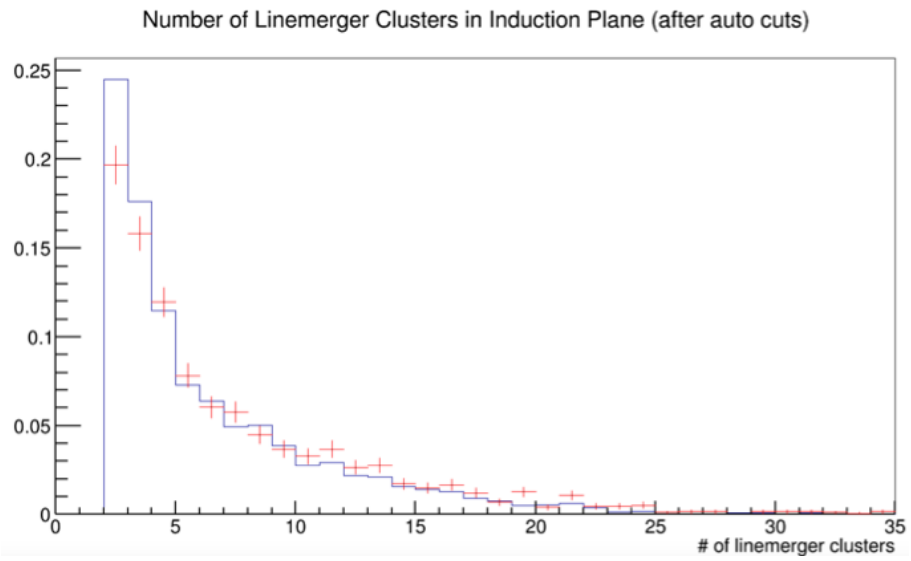


FIGURE 5.16: The number of Linemerger clusters in the Induction wire plane for data (red) and MC (blue) after the automatic cuts. Both have been normalized to one. Figure from [1].

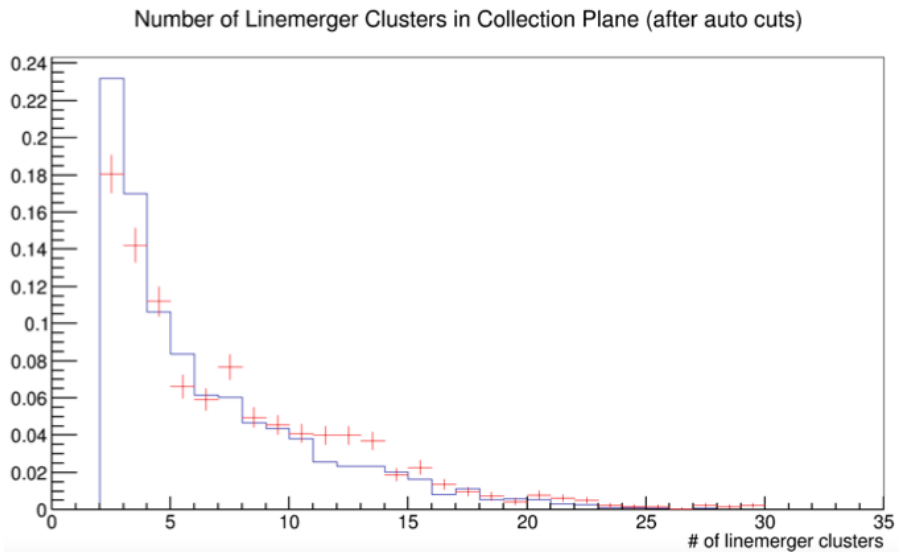


FIGURE 5.17: The number of Linemerger clusters in the Collection wire plane for data (red) and MC (blue) after the automatic cuts. Both have been normalized to one. Figure from [1].

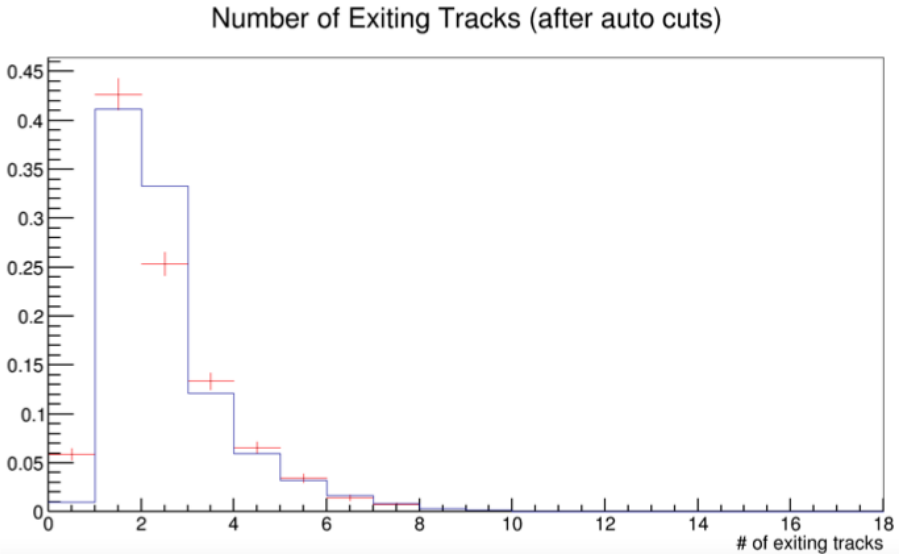


FIGURE 5.18: The number of exiting tracks for data (red) and MC (blue) after the automatic cuts. Both have been normalized to one. Figure from [1].

### 5.4.2 Visual Scanning

The second step of the analysis is visually scanning each event that passed the automatic cuts. With each event, the scanner studies the topology and pulls out relevant

information. Figure 5.19 and Figure 5.20 show the ArgoNeuT event display with a CCQE $\Lambda^0$ event and a scan window that a scanner populated for each event, respectively.

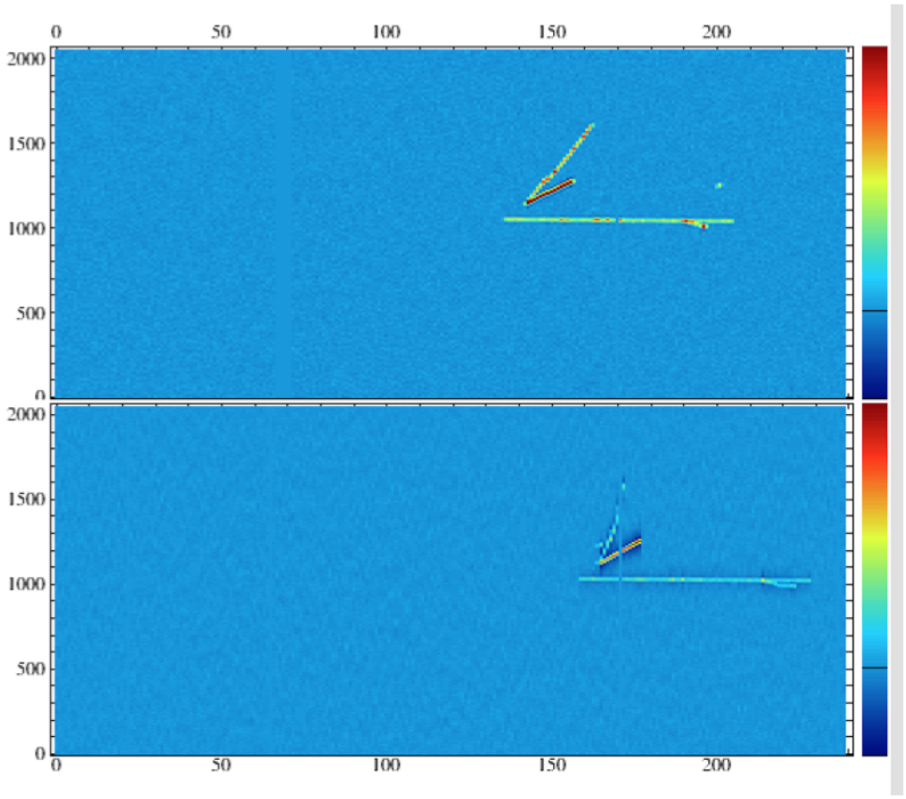


FIGURE 5.19: A CCQE $\Lambda^0$ MC event shown in the ArgoNeuT event display.

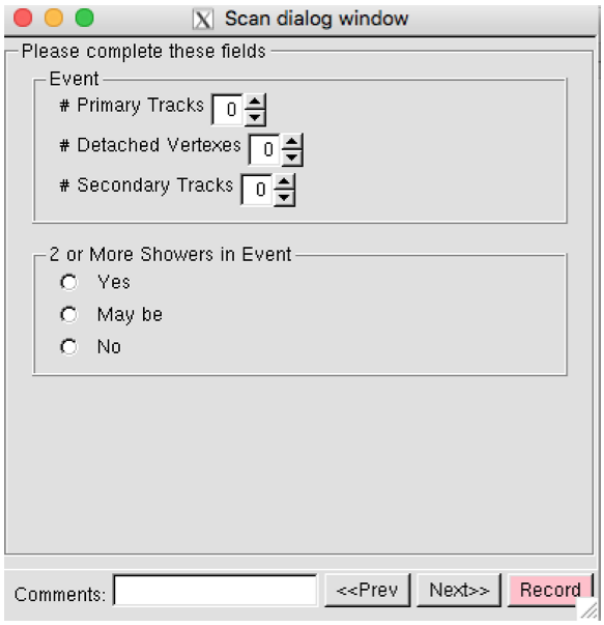


FIGURE 5.20: The scan window populated by the scanner during the visual scanning of neutrino events. Figure from [1].

For each event, the scanner first zooms to identify the primary vertex and records the number of primary tracks in the scan window. They will then scan for any detached vertices (such as the detached vertex in the CCQE $\Lambda^0$ case). If there is one identified, the scanner counts the number of tracks (named secondary tracks) from this detached vertex and records this in the scan window. If there are more than one detached vertices, the vertex that has the most straight secondary tracks is selected. The scan window allows the scanner to reject events that contain through-going muons by identifying the 3D start point of the muon track and determining if the track is entering. The criteria for a 'passed' event through visual scanning is shown below:

1. Only 1 or 2 primary tracks.
2. Exactly 2 secondary tracks.
3. No more than a single electromagnetic shower.

After applying these cuts, 36 data events are selected.

Figure 5.19 shows a very clean CCQE $\Lambda^0$ MC event. One can see the single long track originating from the primary vertex and then the detached vertex with two secondary tracks. The scanner would view this event and state that there is 1 primary track, 1 detached vertex, 2 secondary tracks, with no electromagnetic showers in the event.

Using MC allows us to determine the efficiency of the cuts and the brackground rejection rate. Given in Table 5.1, the efficiency of selecting signal events ($\epsilon_{\text{scan}}$) is 75.7% and the rejection of background events is 98.6%. This drop in the efficiency of selecting signal events comes when the hyperon decays closely to the primary vertex. This is further compounded if the primary and detached tracks are parallel to each other, making it indistinguishable to the scanner where the primary and secondary tracks are. If the signal selection and background rejection rates are scaled to the $1.2 \times 10^{20}$ protons-on-target (POT), the prediction gives 10 signal events and 20 background events for the final selected data sample.

The number distribution of scanning tracks in data and MC following the automatic cuts is shown in Figure 5.21. The distribution of the number of Linemerger clusters in the Induction and Collection wire planes for data and MC after the scanning cuts are given in Figure 5.22 and Figure 5.23, respectively. The distribution of exiting tracks in data and MC after scanning cuts is given in Figure 5.24. In all plots, the data and MC are in agreement and normalized to one. The decay particles in the signal events, a proton and pion created from a decaying neutral hyperon, both exit the TPC 40% of the time, according to MC predictions. MC predictions also show that 19% of the events have only the proton exiting, 10% of the events have only the pion exiting, and 31% of the events have both the proton and pion stopping inside the TPC. Figure 5.25 - Figure 5.26 show a few ArgoNeuT data events that were selected following the scanning cuts.

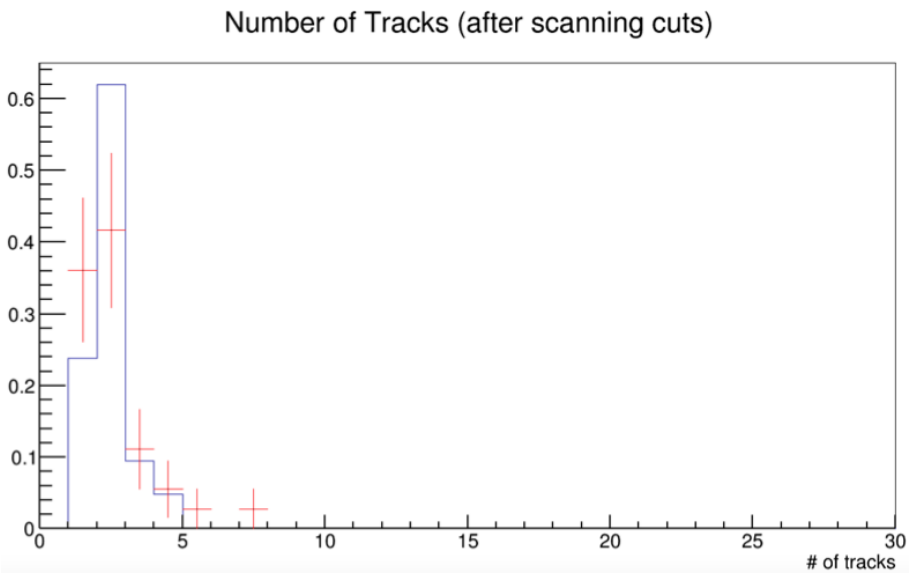


FIGURE 5.21: The number of tracks reconstructed in the data (red) and MC (blue) after the scanning cuts. Both have been normalized to one. Figure from [1].

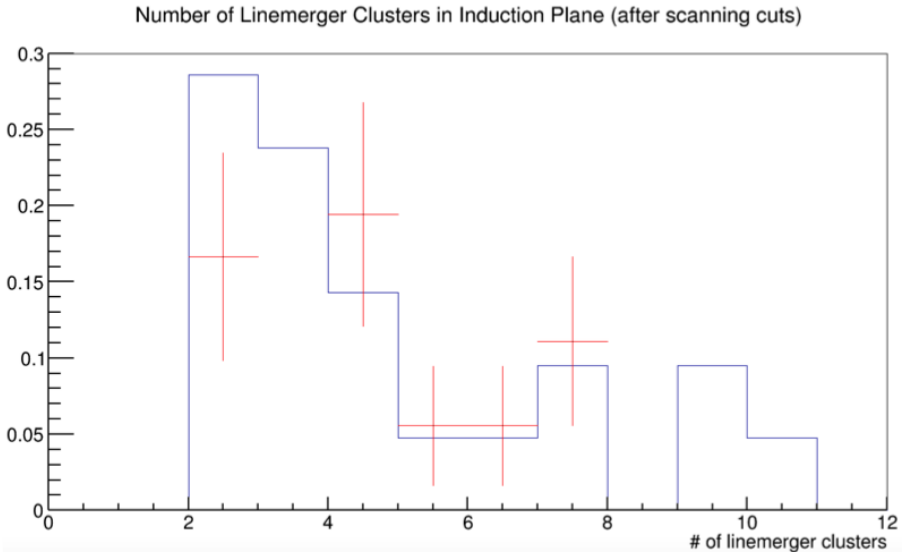


FIGURE 5.22: The number of Linemerger clusters in the Induction wire plane for data (red) and MC (blue) after the scanning cuts. Both have been normalized to one. Figure from [1].

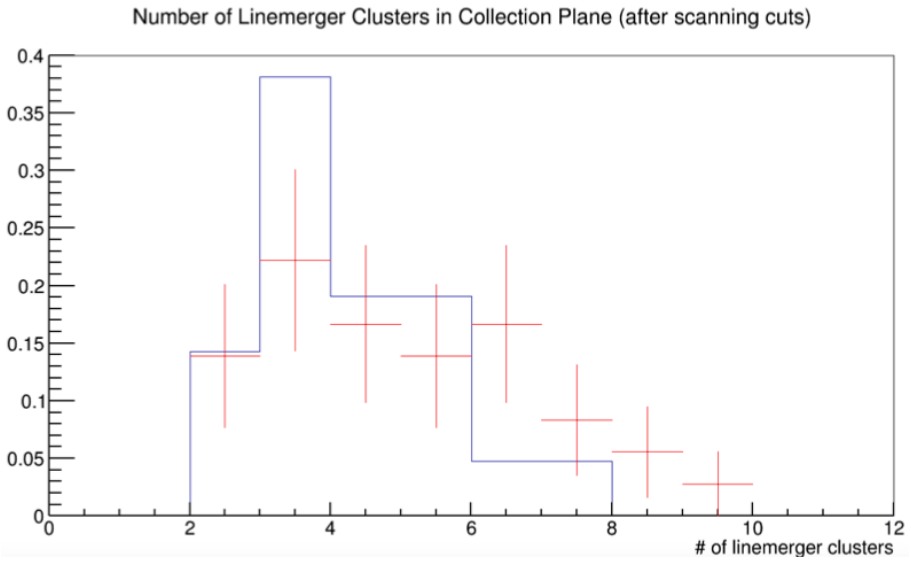


FIGURE 5.23: The number of Linemerger clusters in the Collection wire plane for data (red) and MC (blue) after the scanning cuts. Both have been normalized to one. Figure from [1].

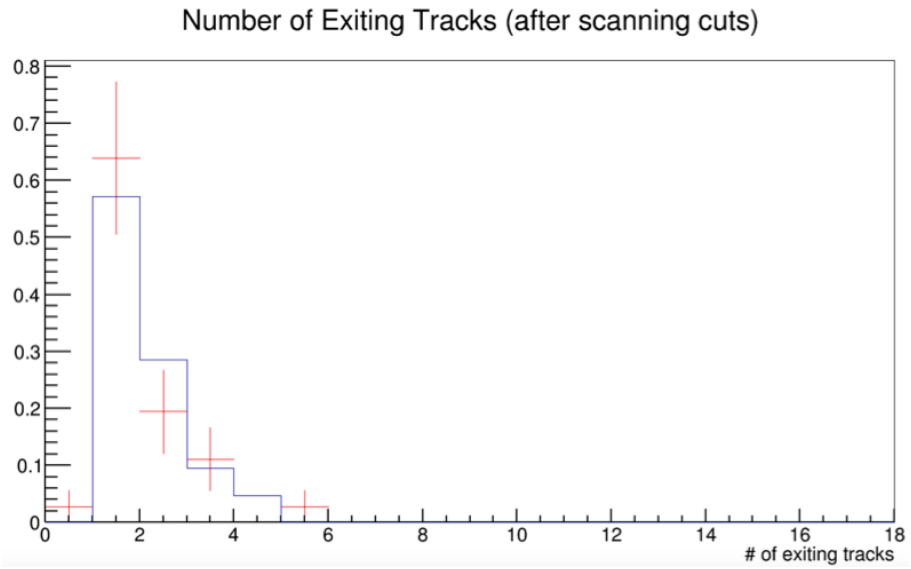


FIGURE 5.24: The number of exiting tracks for data (red) and MC (blue) after the automatic cuts. Both have been normalized to one. Figure from [1].

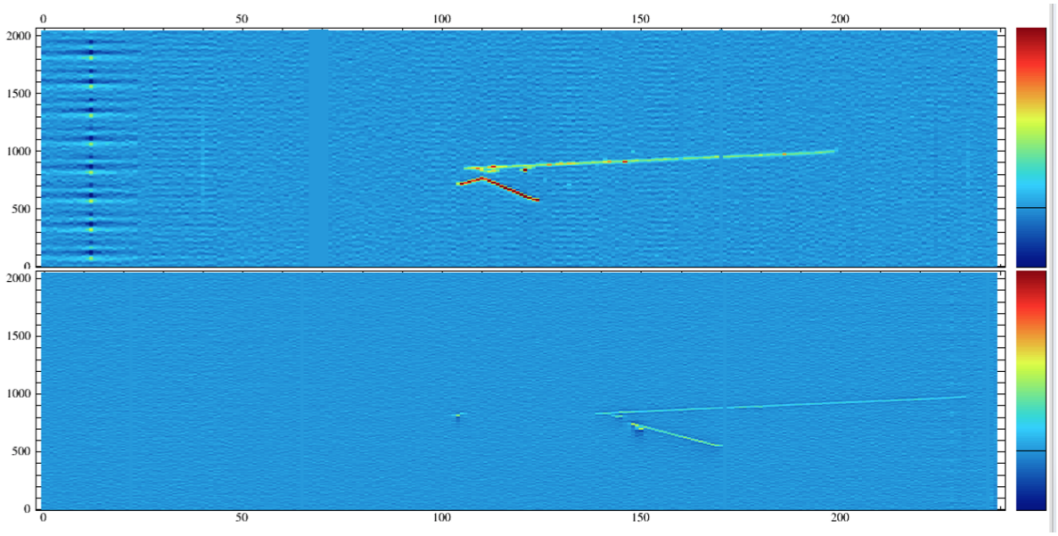


FIGURE 5.25: Data event selected following the scanning cuts. Figure from [1].

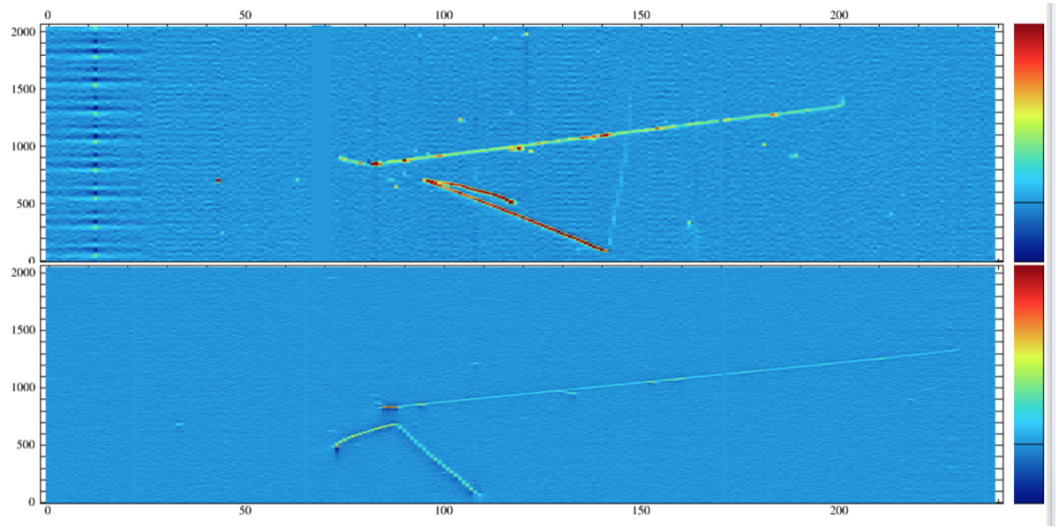


FIGURE 5.26: Data event selected following the scanning cuts. Figure from [1].

Figures 5.21 through 5.24 are similar plots to Figures 5.15 through 5.18 and provide a comparison to how the specified quantities changed following the automatic cuts and scanning cuts, respectively. The visual scanning analysis allows for 3D 'vertex separation', or the separation between the primary and secondary vertices, as well as identifying the opening angle and the lengths of the primary and secondary tracks. The 3D vertex separation in the data and MC is shown in Figure 5.27. The 3D opening

angle between the secondary tracks in data and MC following the scanning cuts is given in Figure 5.28. The 3D lengths of the longer and shorter secondary tracks in data and MC following the scanning cuts are given in Figure 5.29 and Figure 5.30, respectively.

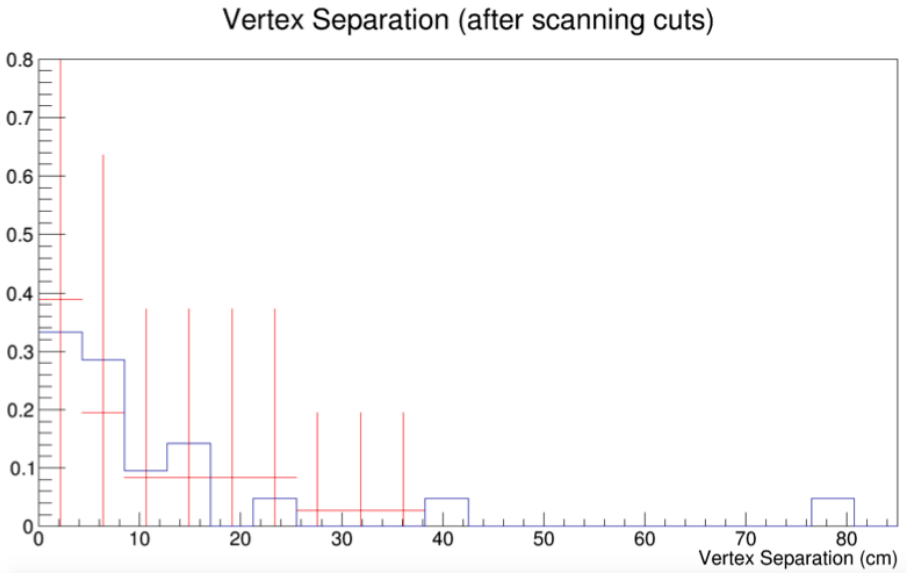


FIGURE 5.27: The vertex separation, or the distance between the primary and secondary detached vertex in data (red) and MC (blue) events following the scanning cuts. Both are normalized to one. Figure from [1].

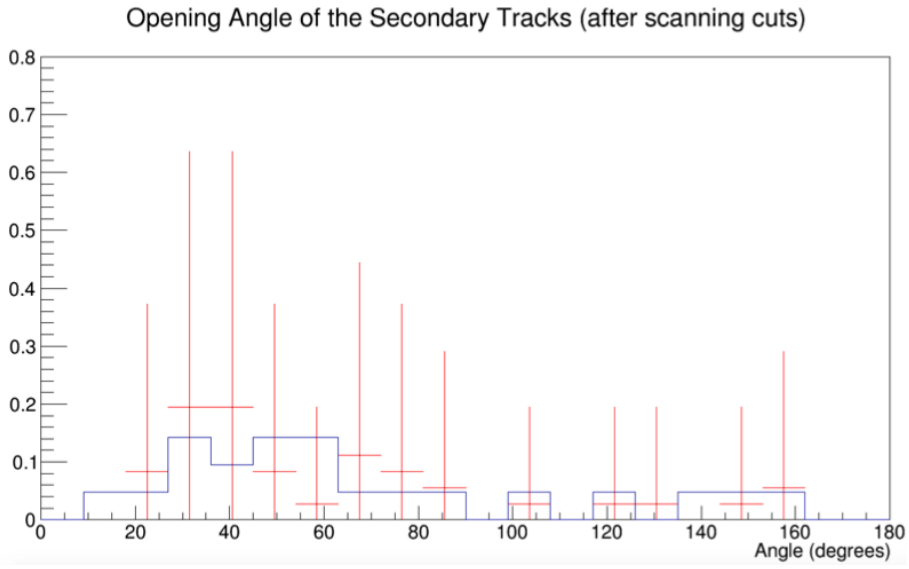


FIGURE 5.28: The 3D opening angle of the secondary tracks in data (red) and MC (blue) following the scanning cuts. Both are normalized to one. Figure from [1].

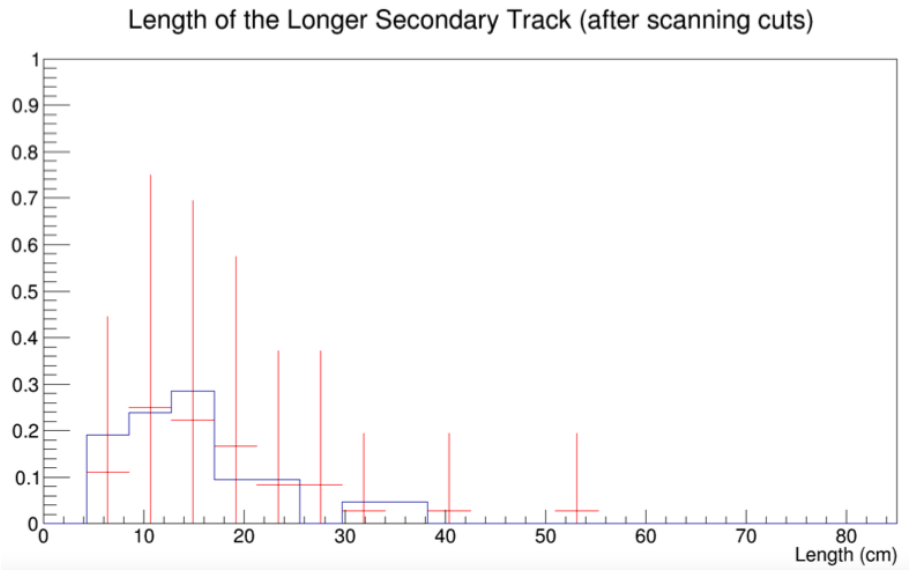


FIGURE 5.29: The length of the longer secondary track in data (red) and MC (blue) following the scanning cuts. Both are normalized to one. Figure from [1].

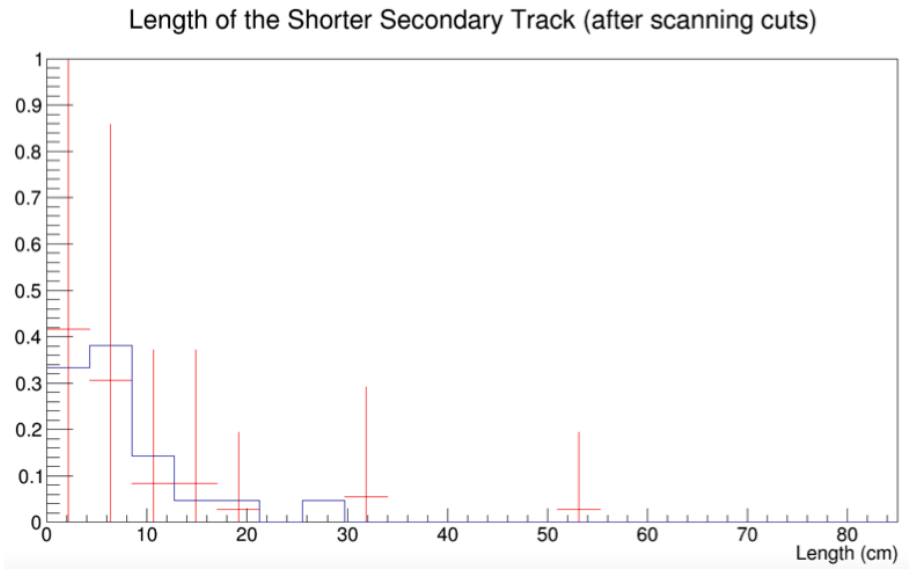


FIGURE 5.30: The length of the shorter secondary track in data (red) and MC (blue) following the scanning cuts. Both are normalized to one. Figure from [1].

### 5.4.3 Post - Visual Scanning Cross Section Measurement

Following the visual scanning, the topological study is complete and the first pass at the cross section measurement can be made. The measurement of the cross section measurement in this analysis sets an upper limit to the cross section at a 90% confidence-level. This measurement uses two independent approaches: a model dependent, using the absolute normalization of the cross section model, and an approximate model independent, using only the shape distributions of the MC signal and background.

The general cross section equation is shown in Equation 5.2, but a more specific equation for this analysis can be written as,

$$\sigma_{(CCQE_{\Lambda^0+\Sigma^0})} = \frac{f \times \left(N_{\text{data}} - N_{\text{bkg}}\right)}{\phi \times N_{\text{targ}} \times \epsilon_{\text{cuts}} \times \epsilon_{\text{scan}}} \tag{5.3}$$

Here $N_{\text{data}}$ is the number of data events that pass all analysis cuts, $N_{\text{bkg}}$ is the predicted number of background events, $\phi$ is the total antineutrino flux, $N_{\text{targ}}$ is the number of targets (protons) in the fiducial volume of the detector, $\epsilon_{\text{cuts}}$ and $\epsilon_{\text{scan}}$ are the efficiencies of the automatic cuts and the scanning cuts respectively, and $f$ is the correction for the branching fraction of hyperon decay to neutral particles.

The model dependent approach gives the cross section as,

$$\sigma_{(CCQE_{\Lambda^0+\Sigma^0})} = \left(3.7 \pm 1.9(\text{stat.}) \pm 1.5(\text{sys.})\right) \times 10^{-40}\text{cm}^2 \tag{5.4}$$

In high energy physics, it is a common standard to consider a measurement statistically significant if it is at least three standard deviations ($3\sigma$) from zero. This study sets a 90% confidence-level (C.L.) upper limit on the cross section measurement,

shown in Equation 5.5.

$$\sigma_{(CCQE_{\Lambda^0+\Sigma^0})} < 7.3 \times 10^{-40} \text{ cm}^2 \text{ at } 90\% \text{ C.L.} \tag{5.5}$$

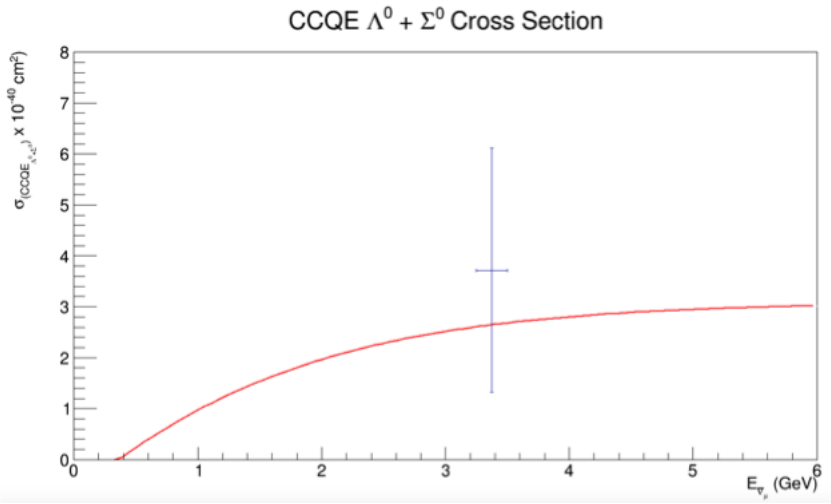


FIGURE 5.31: The total cross section measurement of charge current quasi-elastic $\Lambda^0$ and $\Sigma^0$ production. The NUANCE model is given in red and the topological study result is given in blue. Figure from [1].

#### 5.4.3.1 Background

The background is calculated by normalizing the MC to $1.2 \times 10^{20}$ protons-on-target (POT). Background events are classified as any event that passes all the analysis cuts but is not a CCQE neutral hyperon event shown in Equation 5.1. If the event has a detached vertex with two tracks originated from it, with one or two primary tracks, it can be passed through as a background event. One example of a background event is charge current deep inelastic (CCDIS) interactions, where particles such as $K^0$, $\Lambda^0$, or $\Sigma^0$ are produced in pairs, with one of the pairs exiting the detector without decaying, or decaying into neutral particles. Another possible example is when a charged hyperon is produced with a neutral partner in a CCDIS or neutral current deep inelastic (NCDIS) interaction. More examples could include events where a neutron is produced in the primary interaction and scatters off an argon nucleus to

produce exactly two tracks. These processes account for a total of 64% of the total background.

According to the MC sample, 50% of the background comes from NC/CCDIS interactions, 7% from CCQE interactions, and 43% from CC-resonant interactions. These rates are calculated by convolving the cross section from NUANCE and the flux histograms. Scaling the MC to $1.2 \times 10^{20}$ protons-on-target (POT) predicts 20 background events. Figure 5.32 and Figure 5.33 shows an example of background events selected following the visual scanning. In Figure 5.32, a neutron scatters off an argon nucleus to produce a detached vertex with two secondary tracks. In Figure 5.33, a $K^0$ and $\Lambda^0$ are produced in a pair, with one of them decaying to charged particles inside the TPC.

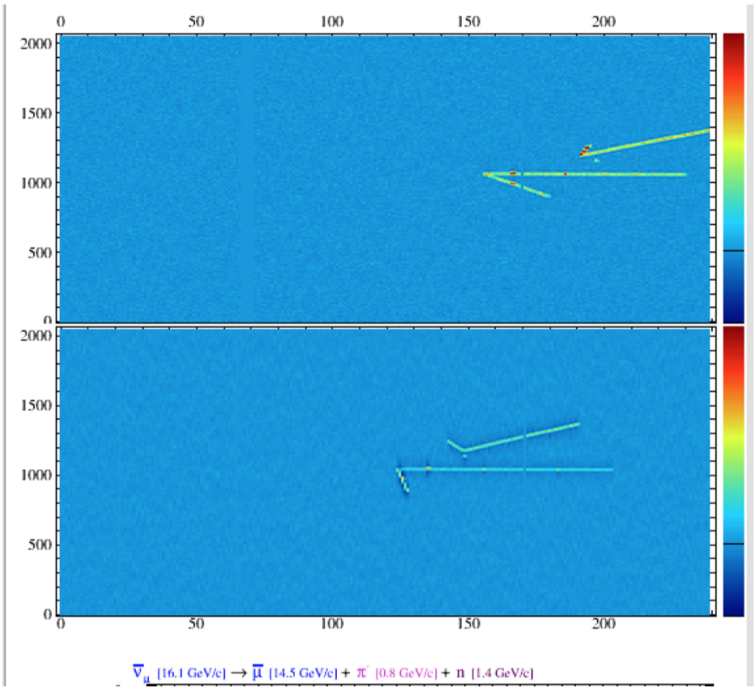


FIGURE 5.32: An example background event following scanning cuts. Figure from [1].

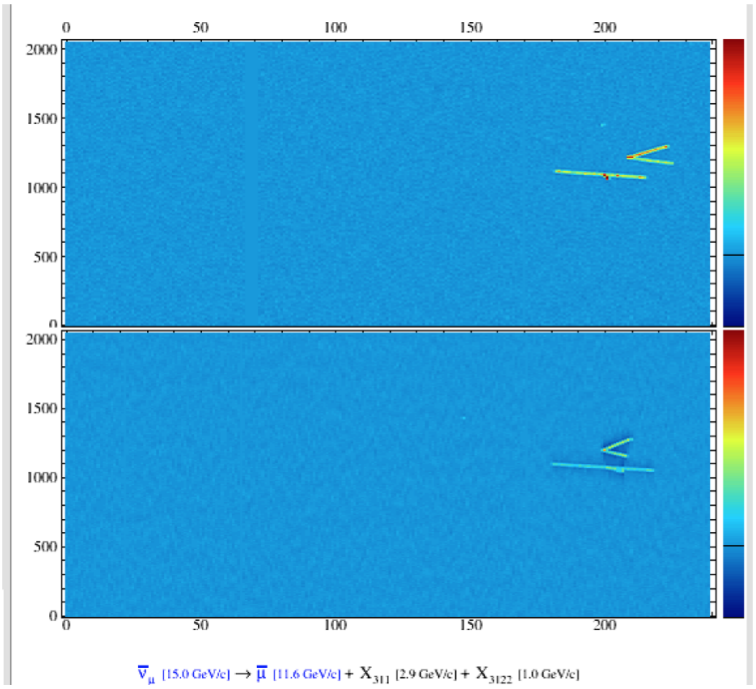


FIGURE 5.33: An example background event following scanning cuts. Figure from [1].

#### 5.4.3.2 Efficiency and Uncertainty

Due to the small number of events available for this study, the statistical uncertainty is significant. The statistical uncertainties can be attributed to the uncertainty in the number of selected data events, the number of predicted background events, and the uncertainty in the efficiency of the automatic reconstruction cuts and the visual scanning cuts.

$$\left(\frac{\delta\sigma_{\text{stat}}}{\sigma}\right)^2 = \left(\frac{\delta N_{\text{data}}}{N_{\text{data}} - N_{\text{bkg}}}\right)^2 + \left(\frac{\delta N_{\text{bkg}}}{N_{\text{data}} - N_{\text{bkg}}}\right)^2 + \left(\frac{\delta\epsilon_{\text{cuts}}}{\epsilon_{\text{cuts}}}\right)^2 + \left(\frac{\delta\epsilon_{\text{scan}}}{\epsilon_{\text{scan}}}\right)^2 \tag{5.6}$$

The first two terms, dictating the uncertainty in the number of selected data events and predicted background events, dominate the total statistical uncertainty. Their contribution to the total uncertainty is 37% and 33%, respectively. The background uncertainty comes from the uncertainty in the selection efficiencies of each of the

cuts on MC and the uncertainty in the NUANCE scaling factor used to scale to $1.2 \times 10^{20}$ POT. For all the efficiencies, binomial uncertainties are used.

Even though this analysis is statistically limited, calculations are made to account for the major sources of systematic uncertainty. Equation 5.4 shows the partitioned contributions to the total systematic uncertainty on the cross section measurement. A flat 11% uncertainty is given to the flux that accounts for the uncertainty in hadron production and beamline modeling. The visual scanning and calorimetric studies also introduces systematic uncertainties that are accounted for.

A set of 4680 data events passed the automatic reconstruction cuts (excluding muon sign requirements) and are then visually scanned by two scanners. The cuts are applied by each scanner and the efficiencies calculated. The difference in efficiencies between the two scanners was calculated to be 3.5%. The beam angle difference from MC and data, discussed previously, also is a source of systematic uncertainty. Following all the cuts, an uncertainty of 6% is given after the MC events are weighted in the muon angle bins. To solve for the systematic uncertainty in the fiducial volume cut, 1 cm is added and subtracted on all sides of the fiducial volume. 1% is determined to be the maximum difference in the event density (number of events per unit volume). The POT count has a systematic uncertainty of 1% [43]. The number of targets has an uncertainty of 2% [12].

There are two estimates of the predicted background, both having the same mean value of 20 estimated events and are consistent. One estimate is the background from MC after applying all the cuts. An uncertainty of 50% is a conservative estimate for the background prediction from the NUANCE model. The second estimate uses the shape fit (described in [1]), also gives an estimate for the background prediction. Combining the two uncertainties allows for the total systematic uncertainty in the

background prediction to be made, which is given at 39% and is the biggest contribution to systematic uncertainty.

$$\left(\frac{\delta\sigma_{\text{stat}}}{\sigma}\right)^2 = \left(0.11_{\text{flux}}\right)^2 + \left(0.035_{\text{scan}}\right)^2 + \left(0.01_{\text{FV}}\right)^2 + \left(0.01_{\text{POT}}\right)^2 + \left(0.02_{N_{\text{targ}}}\right)^2 + \left(0.06_{\text{angle}}\right)^2 + \left(0.39_{\text{bkg}}\right)^2 \tag{5.7}$$

## 5.5 Calorimetric Study

The previous section discussed the procedure conducted in the topological study of the cross section. To provide a complete study of the cross section, the next step is to complete a calorimetric study. This is where this thesis project begins and the remaining sections outline the progress made on the calorimetric study, including the work performed in pursuit of this thesis. The calorimetric study relies on the ideas formulated in Section 2.3.2. With the ability to reconstruct the energy deposited along a track and use that information to identify the particles, it should give additional information. The topological study relies on the spatial features of the particle tracks. By including the calorimetric study, a greater understanding of the cross section measurement is possible. This study is conducted in two major steps, the calorimetric reconstruction and the particle identification. This section will outline the progress made in this analysis and present the future steps required to complete the study.

### 5.5.1 Calorimetric Reconstruction

The accuracy of the calorimetric reconstruction relies heavily on the accuracy of the reconstructed tracks. The dE/dx is dependent on the track direction and the charge deposition of the track, underlying the importance of the proper selection of each hit. At the onset of this study, it was determined that some LArSoft modules were not optimized for the specifics of this study so intervention would be required to

modify them. Due to the unique orientation of the TPC and wire planes, there are events in which two tracks seemingly overlap in the event display, as shown in Figure 5.34. This overlay can introduce cluster and track-finding miscalculations made by the associated LArSoft modules, as no easy distinction between which hits belong to each distinct track can be made.

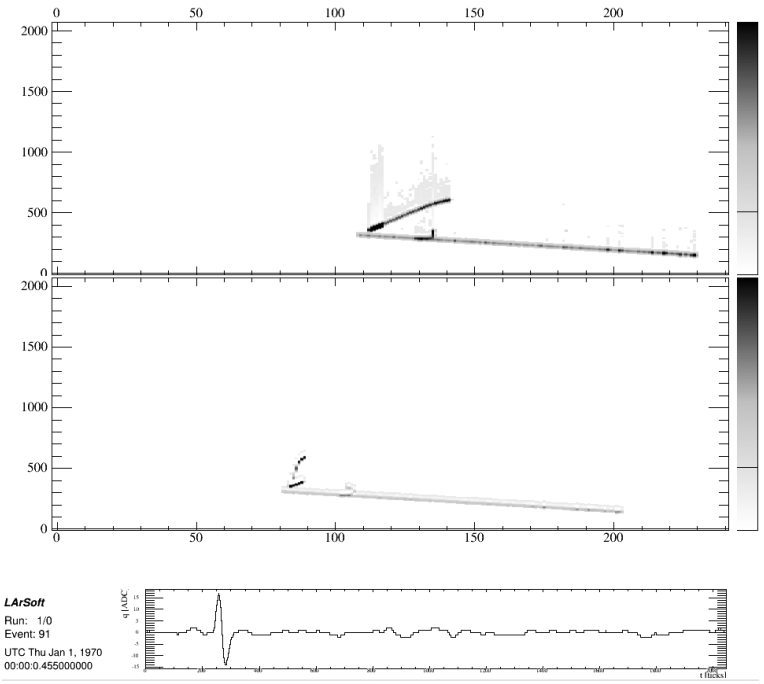


FIGURE 5.34: A event display showing an MC neutrino interaction that passed the topological study. In the top view, two particle tracks are overlaid on one another.

The solution proposed and acted on in this study is to bypass the cluster finding LArSoft module and manually assign hits to individual tracks. Once these hits are associated with the tracks, the tracks can process through the reconstruction chain described in Chapter 4. When the tracks have been reconstructed with the hits, then calorimetric reconstruction can be accomplished using the process outlined in 2.3.2.

The first step in this calorimetric reconstruction is to take all of the events, data and MC, that pass the scanning cuts and manually select the hits associated with each track. This is a rigorous and tedious process, and needs understanding of ArgoNeuT's

event display as well as neutrino interactions. Figure 5.35 through Figure 5.38 show examples of data events with a single manually selected track.

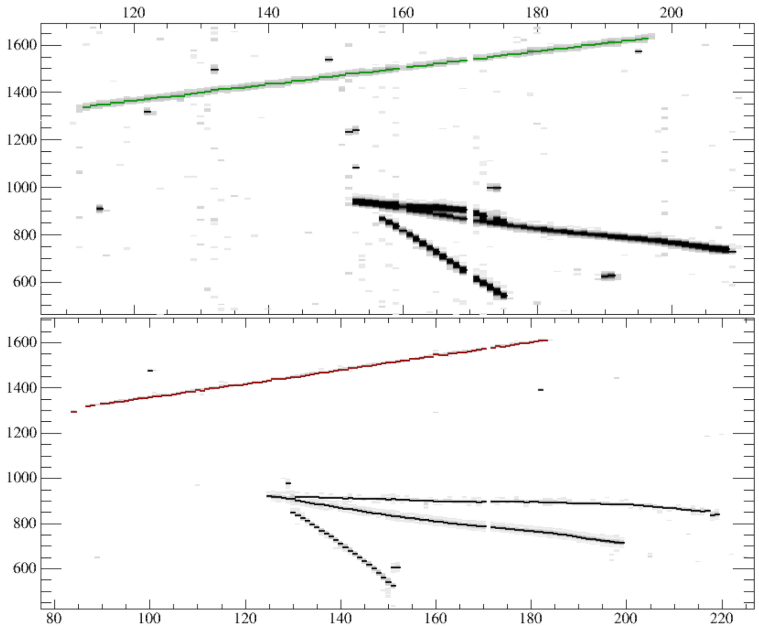


FIGURE 5.35: Data event showing a manually selected track (colored in green or red).

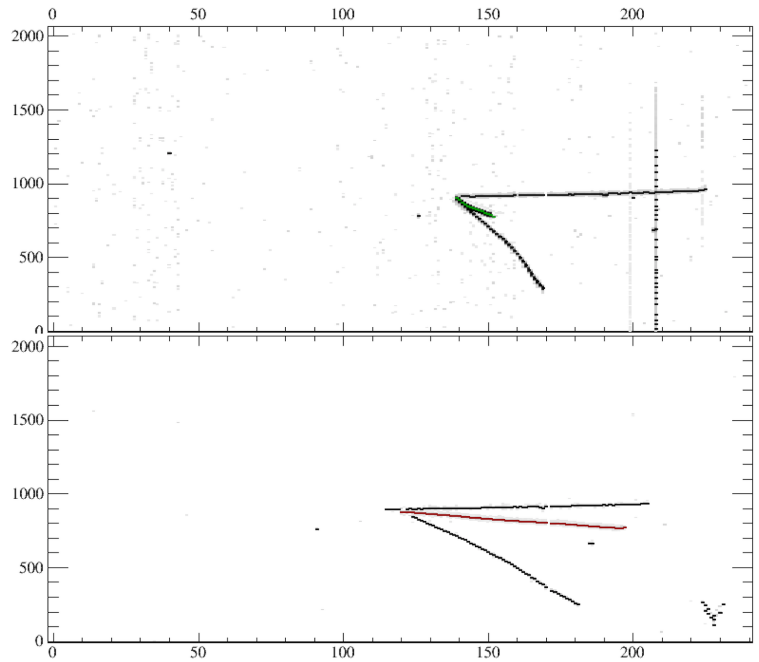


FIGURE 5.36: Data event showing a manually selected track (colored in green or red).

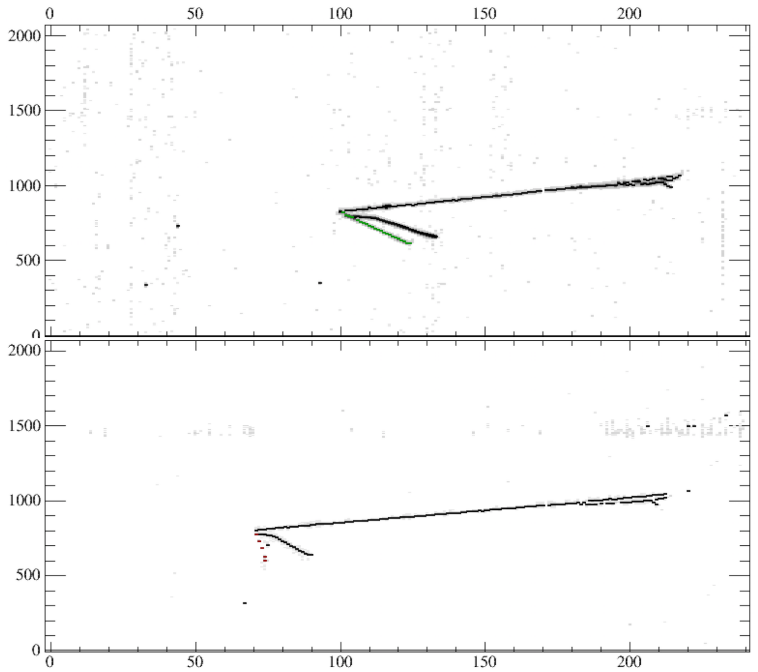


FIGURE 5.37: Data event showing a manually selected track (colored in green or red).

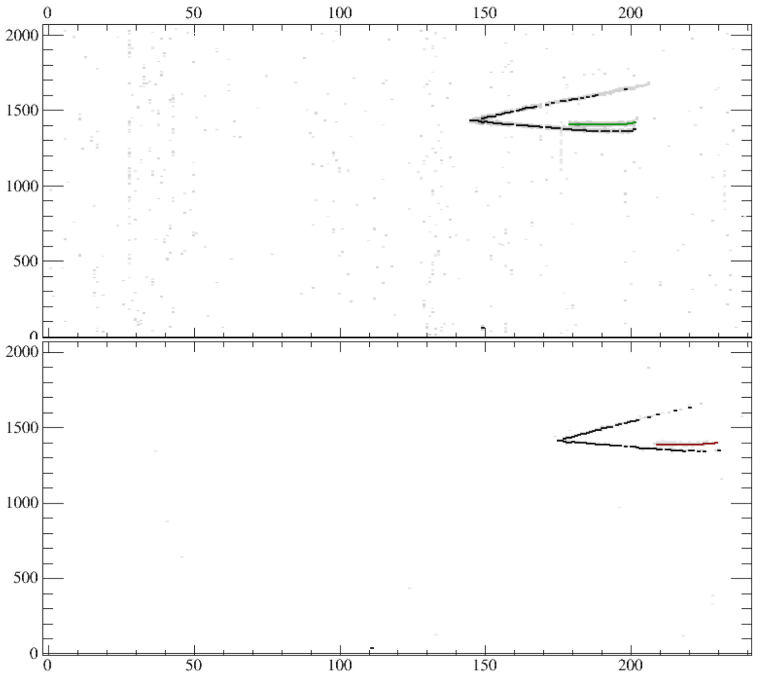


FIGURE 5.38: Data event showing a manually selected track (colored in green or red).

Following the manual selection of all the hits in a single track, the channel number, peak time, and plane (induction vs. collection) are recorded into a text file. By completing this manual selection for each track in an event, with each track separated by the selected hits, a complete description of the event can be made. Following the completion of the manual hit selection, an error was discovered in the process in which the track hits were separated. Following the saving of the first track, all of the same hits would be added to the selected hits for the second track, which would then be both added to the hits of the third track. This lead to the text file holding a distinct group of the first track hits, then a distinct group of the first and second track hits, and then a group of all three track hits in the event, and so on. A module was developed to filter out the subsequently selected hits and create a new filtered text file that only contained the hits associated with the individual track.

As described above, once the track hits are manually selected, they can be used to correlate with the hit finder module. The Track Finder LArSoft module was reconfigured to take in the hit objects from the hit finder module and then filter the hit objects to only pass through hits associated with the same channel number, peak time, and plane as the hits saved into the text file. This allows for the passing of hits into the Track Finder module that correspond with the manually selected hits for each track. There are some potential challenges to this method of selecting hits. In many events, not all tracks will be isolated from one another. In one or both of the planes, tracks can intersect or overlap, giving hits on a single wire that have charge deposited from two tracks. This provides a significant obstacle in manually selecting tracks. If one hit represents two tracks, then that hit must be partitioned to give fractions of the hit's charge to each of the tracks. This is a potential challenge of manually selecting hits that will need to be studied and accounted for. This is the extent to which this study reached at the time of writing of this thesis. The remainder of this section will outline the remaining actions required to complete the calorimetric study.

Once the Track Finder module has the manually selected hits in a track, these hit objects should be converted into cluster objects and then continued to be processed by

the Track Finder module to create 2D line-like tracks and then matched to form 3D tracks, as detailed in Chapter 4. By having the hit and cluster information, it should allow for the 3D tracks to be passed through the remainder of the calorimetric reconstruction chain without significant modification of the modules, since they use both hit and cluster information. Creating cluster objects from the hit objects in the TrackFinder module will allow for potential ease later in the reconstruction chain.

### 5.5.2 Monte Carlo Study

One of the charged particles produced in a CCQE Neutral Hyperon interaction is a $\mu^+$, which is the end state of the incident anti-muon neutrino. Shown in Figure 5.39, the distribution of muon kinetic energies give a mean kinetic energy of roughly 3 GeV. With this kinetic energy, the $\mu^+$ particles will frequently exit the detector before stopping.

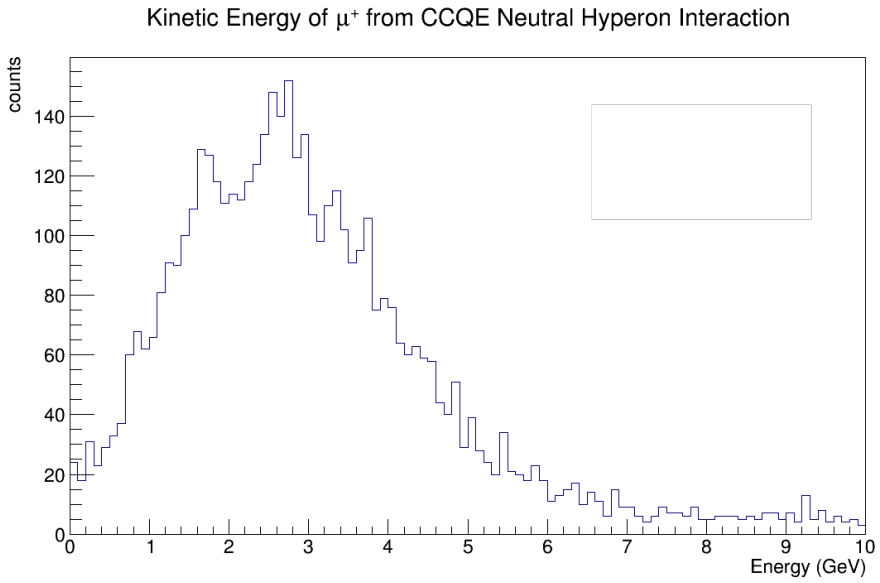


FIGURE 5.39: Distribution of the kinetic energy of MC $\mu^+$ from CCQE Neutral Hyperon interactions.

The other particle produced in tandem with the $\mu^+$ is one of the neutral hyperons, either a $\Lambda^0$ or $\Sigma^0$. As discussed previously, if a $\Lambda^0$ is produced, it will decay directly

into a $p\pi^-$ charged pair or an $n\pi^0$ uncharged pair. If a $\Sigma^0$ is produced, it will quickly decay to a $\gamma\Lambda^0$ pair, which will then decay as given above. Figures 5.40 and 5.41 give the kinetic energy distribution of the $\Lambda^0$ and $\Sigma^0$, with mean kinetic energies of 242 MeV and 262 MeV, respectively.

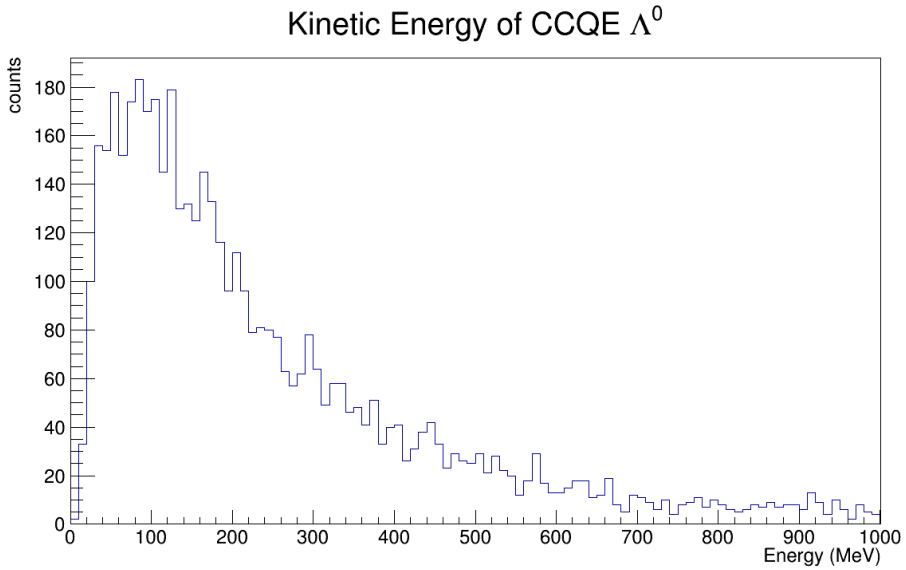


FIGURE 5.40: Distribution of the kinetic energy of MC $\Lambda^0$ from CCQE Neutral Hyperon interactions.

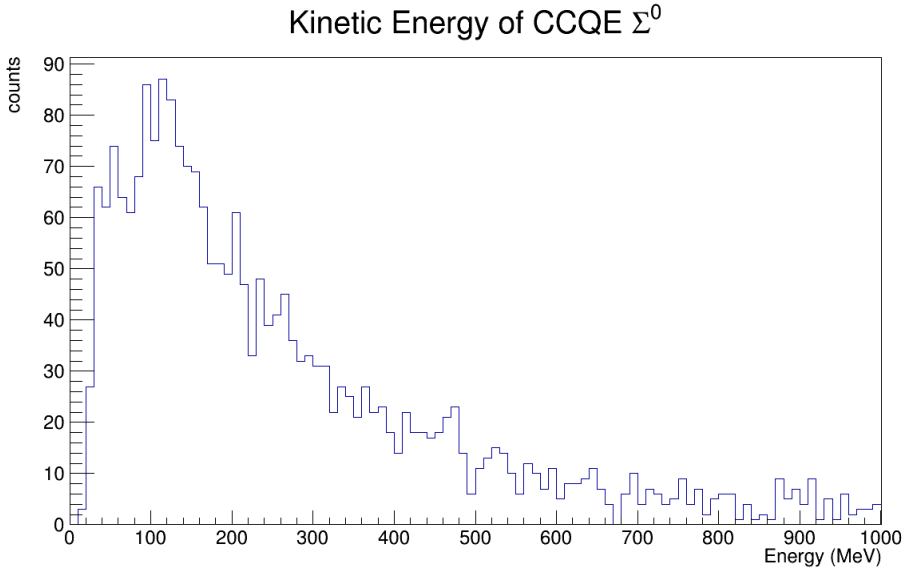


FIGURE 5.41: Distribution of the kinetic energy of MC $\Sigma^0$ from CCQE Neutral Hyperon interactions.

The distribution of kinetic energies from protons and $\pi^-$ particles are given in Figures 5.42 and 5.43 with mean kinetic energies of 206 MeV and 70 MeV, respectively. These distributions include protons and $\pi^-$ produced in $\Lambda^0$ decay, regardless if the $\Lambda^0$ was produced from a $\Sigma^0$. The protons and $\pi^-$ particles have energies sufficient enough to leave the detector depending on the location of the secondary vertex.

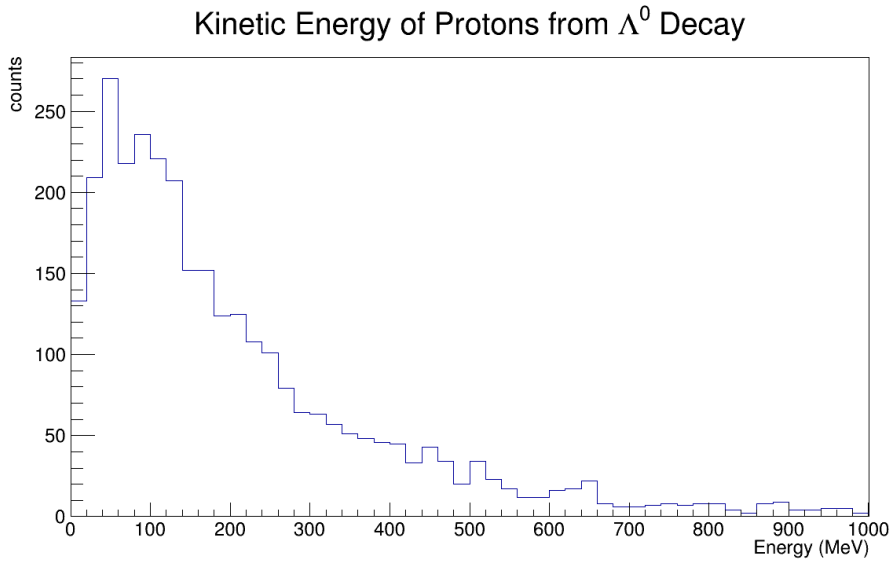


FIGURE 5.42: Distribution of the kinetic energy of MC protons from CCQE $\Lambda^0$ interactions.

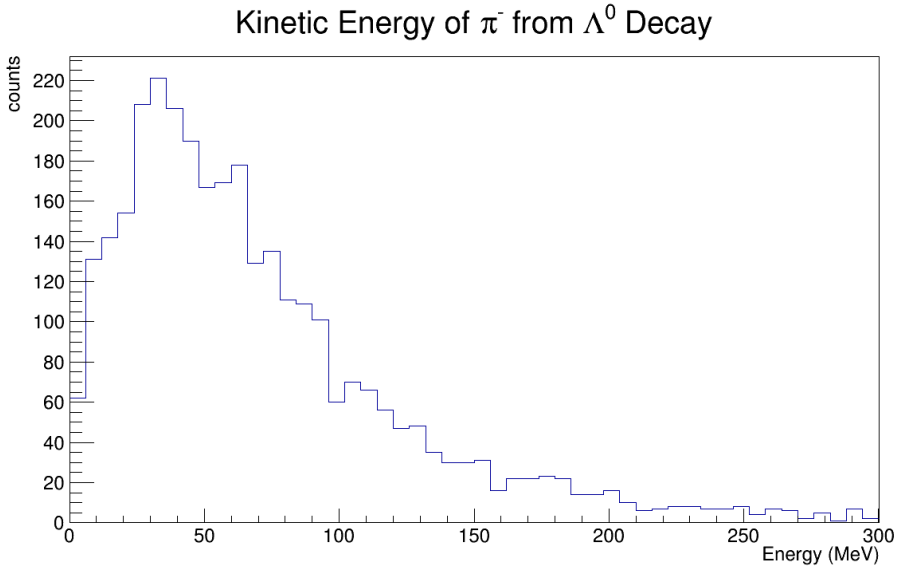


FIGURE 5.43: Distribution of the kinetic energy of MC $\pi^-$ from CCQE $\Lambda^0$ interactions.

If a $\Sigma^0$ is produced, it will decay into a $\Lambda^0$ 100% of the time and a photon. The distribution of the photon energies are given in Figure 5.44. With a mean energy of 92 MeV, photons are visible by the detector as they form an electromagnetic shower.

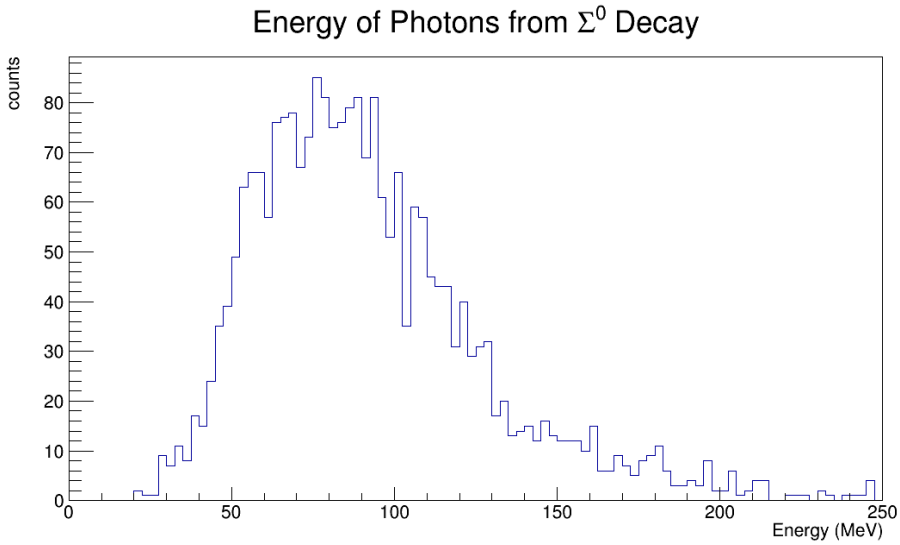


FIGURE 5.44: Distribution of energy of MC photons from CCQE Neutral Hyperon interactions.

An additional piece of information gleaned from Monte Carlo that is useful is the mean decay length of the $\Lambda^0$. Figure 5.45 shows a mean decay length of 4.3cm.

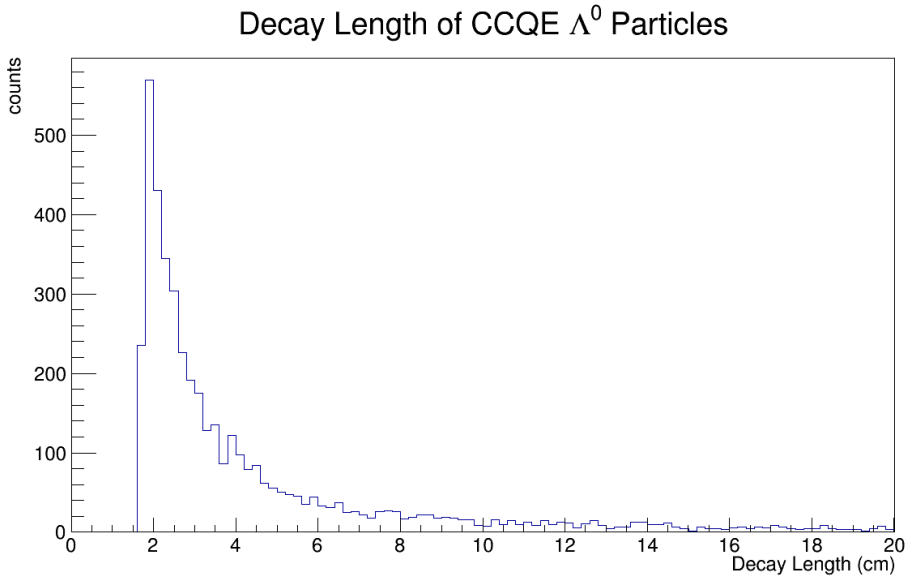


FIGURE 5.45: Distribution of decay lengths of MC $\Lambda^0$'s in CCQE Neutral Hyperon interactions.

### 5.5.3 Particle Identification

Following the three dimensional track reconstruction, the tracks can then be processed through the Calorimetric Reconstruction module, outlined in Section 4.3.9. This module will allow for the $dE/dx$ and the kinetic energy to be reconstructed for each track. If a particle stops within the detector, particle identification can be made by matching the particle's $dE/dx$ with the residual range and the kinetic energy with the total range. This is highlighted in Section 4.3.9 and Figure 4.13. Particle identification allows for a calorimetric cut to be made. Using the known particles produced, events can be selected through matching the particle identification.

There are significant limitations to this study. This analysis is statistically limited in both studies, but even more so in the Calorimetric Study. In order to accurately measure the kinetic energy of a particle, the full track must be inside the detector volume. The number of particle events that have full tracks contained to the detector volume is extremely statistically limited. However, utilizing calorimetric reconstruction from LArTPCs on events will give additional analyses to the cross section measurement and bolster the findings from the topological study.

### 5.5.4 Future Direction

The completion of this study will be the combination of the cross-section measurements from the topological and calorimetric studies. The topological study has been completed and a full description of the results can be found [1]. The calorimetric study, to which this thesis details, is currently in-progress. The goal of the calorimetric reconstruction is to utilize the energy information to verify that the events are true CCQE Neutral Hyperon events. This section will give an outline for the future actions required to complete the calorimetric study.

The first actions needed to be taken are the completion of the TrackFinder module, to produce three dimensional tracks that have been manually selected. As of the writing

of this thesis, the TrackFinder module has been redesigned such that it can input the HitFinder hit objects and the txt files of manually selected hits. The HitFinder is then able to filter the hit objects for each track so that only manually selected hits are passed for each track. Further code development must be implemented to convert the passed track hits into cluster objects and through the reconstruction chain to produce three dimensional tracks.

The first step is to take the three dimensional track and account for the track pitch, which gives the deposited charge per unit track length. The next step is to correct for absorption, or electron lifetime, which accounts for when charge is lost due to electronegative impurities. Finally, applying Birk's Law, which includes a correction for recombination, will yield the energy deposited per unit length, $dE/dx$. Once $dE/dx$ is calculated for each track, the energy can be summed along the tracks to determine the total deposited energy.

The next step in the calorimetric study is to determine the invariant mass of the candidate neutral hyperon, based on the calorimetric information from the candidate proton and $\pi^-$ tracks. Every event that passes the visual scanning cut should have a secondary vertex with two tracks.

Before the next step is presented, it is important to first provide a brief theoretical formalism for invariant mass. The invariant mass, or rest mass, of a particle is the partition of the total mass of the particle that is independent of movement [44], meaning it is unchanged no matter the reference frame. In more precise terms, it is the pseudo-Euclidean length of the four-vector $(E, p_x, p_y, p_z)$, or $(E, \mathbf{p})$, known as the 4-momentum vector. Due to its independence of movement, invariant mass is the same in all reference frames. One can build an equation for the invariant mass using the energy-momentum relation, given in Eq 5.8

$$m_0^2 c^2 = \left(\frac{E}{c}\right)^2 - |\mathbf{p}|^2 \tag{5.8}$$

Here, $m_0$ is the invariant mass, $c$ is the speed of light, $E$ is total energy, and $\mathbf{p}$ is the particle's momentum. This can then be rearranged to solve for invariant mass $m_0$ [44],

$$m_0 = \frac{1}{c^2}\sqrt{E^2 - p^2c^2} \tag{5.9}$$

If a particle increases its velocity, both its energy and momentum will increase in a way that $E^2 - p^2c^2$ remains unchanged.

It is common to use natural units (i.e. $c = 1$) and keeping the equation as the square of the invariant mass, [45],

$$m_0^2 = E^2 - \left|\mathbf{p}\right|^2 \tag{5.10}$$

In the case where a $\Lambda^0$ decays into a proton and a $\pi^-$, the invariant mass of the system (proton and $\pi^-$) can be calculated by the addition of the four-momentum of the two particles,

$$m_{\Lambda^0}^2 = (E_p + E_{\pi^-})^2 - \left|\mathbf{p}_p + \mathbf{p}_{\pi^-}\right|^2 \tag{5.11}$$

Equation 5.11 gives the invariant mass of the $\Lambda^0$, since the secondary vertex is the point of decay of the $\Lambda^0$. This can serve as a check point for the signal events. Using the invariant mass of the two tracks originating from the secondary vertex and the solving for the invariant mass of the neutral particle producing the two particles, allows for the verification that it truly is a $\Lambda^0$ decaying into a proton and a $\pi^-$.

Equation 5.11 can be calculated using the particle's masses and kinetic energies, using the relation $E = \mathrm{KE} + m$, where KE is the particles kinetic energy calculated from dE/dx, and $m$ is the known mass of the particle, and the relation $|\mathbf{p}|^2 = E^2 - m^2$ which is derived from Equation 5.9. First, the squares can be expanded,

$$m_{\Lambda^0}^2 = \left(E_p^2 + 2E_pE_{\pi^-} + E_{\pi^-}^2\right) - \left(p_p^2 + p_{\pi^-}^2 + 2p_pp_{\pi^-}\cos\theta_{\hat{p}_p\hat{p}_{\pi^-}}\right) \tag{5.12}$$

Here $\theta_{\hat{p}_p \hat{p}_{\pi^-}}$ is the angle between the two tracks originating from the secondary vertex. Using the rearrangements of the energy-momentum relation, $m^2 = E^2 - p^2$,

$$m^2_{\Lambda^0} = m^2_p + m^2_{\pi^-} + 2E_p E_{\pi^-} - 2\big(p_p\big)\big(p_{\pi^-}\big)\cos\theta_{\hat{p}_p \hat{p}_{\pi^-}} \tag{5.13}$$

LArTPC's provide precise measurements of a particles dE/dx and kinetic energy, given that the particle stops within the detector. Using the kinetic energies given by the detector and the known masses of protons and $\pi^-$s, the experimental calculation of the $\Lambda^0$ invariant mass can be done using Equation 5.13. Once the momentum vectors of the proton and $\pi^-$ are calculated, using the energy-momentum relation given in 5.10 and the reconstructed track's orientations, they can be summed together to find the momentum vector of the $\Lambda^0$, using to the Law of Conservation of Momentum.

Furthermore, the momentum vector of the $\Lambda^0$ can be traced back to ensure that it does originate from the primary vertex. Taking the negative of the momentum vector components will give the direction that that $\Lambda^0$ travelled from, which can be tracked back to see if it crosses the primary vertex. A certain amount of uncertainty would have to be determined to define when a $\Lambda^0$ track originates from the primary vertex.

By using the calorimetric information to verify that a $\Lambda^0$ particle is produced and originates from the primary vertex, which then decays into a proton and a $\pi^-$, a more accurate verification of signal events is possible. By applying this analysis to all the events passing the scanning cut, a calorimetric cut can be made to remove events that do not pass the calorimetric verification given above. This would allow for a cross-section measurement of CCQE neutral hyperons to be calculated through the calorimetric study, completing this analysis.

## 5.6 Conclusion

This thesis outlines the first measurement of CCQE neutral hyperon production cross section in a liquid argon time projection chamber (LArTPC) through a topological

study [1] and presents the ongoing progress of the addition of a calorimetric study. The analysis uses $1.20 \times 10^{20}$ protons-on-target, in the NuMI beam operating in the low energy antineutrino mode. The results of the topological study provide a total cross section measurement at the mean production energy of 3.42 GeV for CCQE neutral hyperons. The result of the topological study is consistent with the NUANCE cross section model and sets a 90% confidence level on the upper limit of the cross section. The calorimetric study is ongoing and shows promise to provide additional results to compare to the topological study findings. The further actions described in Section 5.5.4 outline the necessary steps needed to complete the calorimetric study. This total analysis is statistically limited, due to several factors. CCQE neutral hyperon production is naturally suppressed by a factor of $sin^2\theta_c$, where $\theta_c$ is the Cabibbo angle. The ArgoNeuT detector is a small detector and it only had a five month runtime. The studies outlined in this thesis could be used at larger LArTPC detectors that have a higher proportion of contained events, that are introduced to more intense neutrino beams, and that have longer runtimes.

# BIBLIOGRAPHY


[1] S. Farooq. Kansas State University, 2016.

[2] R. H. Robertson K. Snover A. Balantekin K. Heeger M. Ramsey-Musolf D. Bemmerer A. Junghans C. Bertulani E. Adelberger, A. GarcÂťÄśa et al. Reviews of modern physics. 83(195), 2011.

[3] J. N. Bahcall. Cambridge University Press, 1989.

[4] R. Smith and E.J. Moniz. Nuclear physics b. 43(605), 1972.

[5] D. Casper. Nuclear physics b-proceedings supplements. 112(161), 2002.

[6] A. Pais. Annals of physics. 63(361), 1971.

[7] S. Chauhan M. R. Alam, M. S. Athar and S. Singh. Journal of physics g: Nuclear and particle physics. 42(055107), 2015.

[8] G. Scanavini. Yale University, 2017.

[9] http://arxiv.org/pdf/1507.06690v2.pdf.

[10] K. A. Partyka. Yale University, 2013.

[11] A. Collaboration J. Spitz et al. volume 312. IOP Publishing, 2011.

[12] J. Spitz. Yale University, 2011.

[13] A. Martinez. Universidad de Granada, 2007.

[14] J. B. Birks. Proceedings of the physical society. section a. 64(874), 1951.

[15] B. Baller T. Bolton C. Bromberg F. Cavanna E. Church D. Edmunds A. Ereditato S. Farooq C. Anderson, M. Antonello et al. Journal of instrumentation. 7 (P10019), 2012.

[16] K. Arms R. Armstrong D. Auty S. Avvakumov D. Ayres B. Baller B. Barish P. Barnes Jr P. Adamson, C. Andreopoulos et al. Physical review d. 77(072002), 2008.

[17] T. Alexopoulos W. Allison G. Alner K. Anderson C. Andreopoulos M. Andrews R. Andrews C. Arroyo D. Michael, P. Adamson et al. Nuclear instruments and methods in physics research section a: Accelerators, spectrometers, detectors and associated equipment. 596(190), 2008.

[18] J.Sander M. Ester, H.-P. Kriegel and X. Xu. Kdd. 96(226-231), 1996.

[19] W. Pauli. "dear radioactive ladies and gentlemen". 1930.

[20] E. Fermi. Z. physik. 88(161), 1934.

[21] F. Harrison H. Kruse C. Cowan, F. Reines and A. McGuire. Science. 124(103), 1956.

[22] K. Goulianos L. Lederman N. Mistry M. Schwartz G. Danby, J. Gaillard and J. Steinberger. Physical review letters. 9(36), 1962.

[23] C. Andreopoulos N. Saoulidou G. Tzanakos P. Yager B. Baller D. Boehnlein W. Freeman B. Lundberg K. Kodama, N. Ushida et al. Physics letters b. 504(218), 2001.

[24] R. Hayward D. Hoppes C.-S. Wu, E. Ambler and R. P. Hudson. Physical review. 105(1413), 1957.

[25] L. Grodzins M. Goldhaber and A. Sunyar. Physical review. 109(1015), 1958.

[26] R. Davis. Progress in particle and nuclear physics. 32(13), 1994.

[27] C. L. Smith. Physics reports. 3(261), 1972.

[28] R. Smith and E. J. Moniz. Nuclear physics b. 43(605), 1972.

[29] N. Cabbibo. Physical review letters. 10(531), 1963.

[30] N. Cabbibo and F. Chilton. Physical review. 137(B1628), 1965.

[31] S. K. Singh and M. V. Vacas. Physical review d. 74(053009), 2006.

[32] S. Mintz and L. Wen. The european physical journal a. 33(299), 2007.

[33] K. Kuzmin and V. Naumov. Physics of atomic nuclei. 72(1501), 2009.

[34] I. Sick and J. McCarthy. Nuclear physics a. 150(631), 1970.

[35] T. Cranshaw O. Bunemann and J. Harvey. Canadian journal of research. 27(191), 1949.

[36] U. Sowanda G. Bakale and W. F. Schmidt. The journal of physical chemistry. 80 (2556), 1976.

[37] D. Bhattacharya F. Cavanna J. Dobson S. Dytman H. Gallagher P. Guzowski R. Hatcher P. Kehayias C. Andreopoulos, A. Bell et al. Nuclear instruments and methods in physics research section a: Accelerators, spectrometers, detectors and associated equipment. 614(87), 2010.

[38] C. Juszczak T. Golan and J. T. Sobczyk. Physical review c. 86(015505), 2012.

[39] J. Revol C. Rubbia W. Tian P. Picchi F. Cavanna G. P. Mortari M. Verdecchia D. Cline P. Cennini, S. Cittolin et al. Nuclear instruments and methods in physics research section a: Accelerators, spectrometers, detectors and associated equipment. 345(230), 1994.

[40] L. Berg. Zamm-journal of applied mathematics and mechanics. 62(282), 1982.

[41] L. R. Rabiner and B. Gold. Englewood cliffs, nj, prentice-hall, inc. 777(p. 1), 1975.

[42] P. V. Hough. International conference on high energy accelerators and instrumentation. 73, 1959.

[43] M. Collaboration D. Harris et al. hep-ex/0410005, 2004.

[44] https://www.jlab.org/Hall-B/notes/clas_notes04/2004-008.pdf.

[45] J.R. Forshaw and A.G. Smith. Wiley, 2009.

# AUTHOR'S BIOGRAPHY

Samuel M. Borer was born in Sacramento, California on April 25th, 1993. His father was an Air Force Physician and he spent his childhood traveling the world. Samuel is pursuing a Bachelor of Science degree in physics and mathematics. He is a member of the Sigma Pi Sigma Physics Honors Society and Pi Mu Epsilon Mathematics Honors Society. He received a NASA-MSGC fellowship for the work outlined in this thesis.

Upon graduation, Samuel plans to spend a year working as an AIP public policy fellow with Senator Tammy Duckworth and then enter medical school, pursuing a career in pediatric neurosurgery.